THEORETICAL INVESTIGATIONS ON STRATEGIES FOR SAMPLING METEOROLOGICAL AND CHEMICAL FIELD QUANTITIES IN SMOKE PLUMES USING UAVS

By

Mary K. Butwin

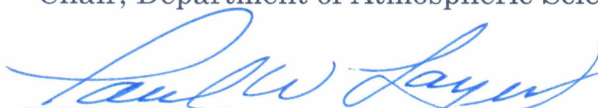RECOMMENDED:

Dr. Uma S. Bhatt

Dr. Richard L. Collins

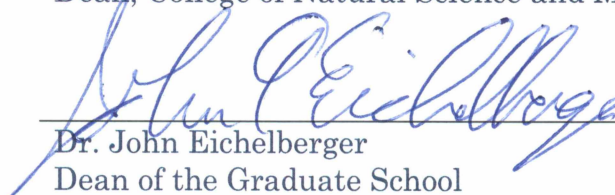Dr. Dr. Nicole Mölders
Advisory Committee Chair

Dr. Uma S. Bhatt
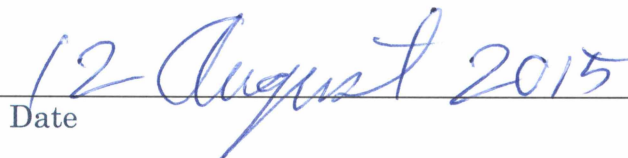Chair, Department of Atmospheric Sciences

APPROVED:

Dr. Paul W. Layer
Dean, College of Natural Science and Mathematics

Dr. John Eichelberger
Dean of the Graduate School

12 August 2015
Date

THEORETICAL INVESTIGATIONS ON STRATEGIES FOR SAMPLING

METEOROLOGICAL AND CHEMICAL FIELD QUANTITIES IN SMOKE

PLUMES USING UAVS

A

THESIS

Presented to the Faculty

of the University of Alaska Fairbanks

in Partial Fulfillment of the Requirements

for the Degree of

MASTER OF SCIENCE

By

Mary K. Butwin, B.S.

Fairbanks, AK

August 2015

Abstract

Wildfires emit large quantities of pollutants that decrease the air quality in the atmospheric boundary layer. Understanding the chemical makeup of a fire plume is beneficial for air quality studies and for air quality forecasting in communities. To be able to understand the chemical composition, Unmanned Aerial Vehicles (UAVs) should be flown into plumes with an air quality instrumental payload.

Before such flights can be completed it is crucial that the flight paths will allow for a complete understanding of the chemical concentration distributions within the plume.

To develop such a flight path, with respect to flight altitude, direction and speed the UAV should travel at for examining a wildfire plume in Interior Alaska, output from the Weather Research and Forecasting model coupled with Chemistry (WRF/Chem) was used and was considered to be the true atmospheric conditions over the UAV measurement domain.

For this thesis simulations were for 3-10 August 2009 of the Alaska fire season, centered in Interior Alaska. Focus for the UAV study was on the smoke plumes from the Crazy Mountain Complex fires near Circle, AK.

Based on the results from the comparison of different flight altitudes, sampling patterns, and speeds of the simulated UAV flights, recommendations can be made for the use of UAVs in a field campaign into a wildfire plume in Interior Alaska.

Table of Contents

List of Figures

List of Tables

Acknowledgements

Chapter 1
Introduction

Wildfires burn on average one million acres of land each year in Alaska alone; these fires are a natural part of ecosystem evolution, but when they approach populated areas problems arise (NPS, 2014; Alaska Public Lands Information Centers, 2014). As biomass burns, there is a release of pollutants that affect air quality, atmospheric chemistry, health and climate (e.g. Mott et al., 2002; Bowman and Johnston, 2005; Kinney et al., 2008; Langmann et al., 2009; Grell et al., 2011; Environmental Protection Agency (EPA), 2013a).

Fires are a major source of trace gases and aerosols in the atmosphere, and gas/aerosol concentrations are also highly variable arising from different fuel types (van der Werf et al., 2010). Burning biomass releases various chemicals and particulate matter such as (but not limited to): carbon monoxide (CO), carbon dioxide (CO_2), methane (CH_4), mono-nitrous oxides (NO_x), volatile organic carbon (VOC), particulate matter of diameter 10 μm or less (PM_{10}) and particulate matter of diameter of 2.5 μm or less ($PM_{2.5}$) which is part of PM_{10} (Nance et al. 1993; Vicente et al., 2013). These chemicals and particulate matter undergo numerous chemical reactions and transformations resulting from processes such as photolysis and reactions with other chemical substances (Hodzic et al., 2007; Heilman et al., 2014). Fire state also affects what is released into the atmosphere; for example, higher concentrations of particulate matter and CO are released in smoldering fires than in well-ventilated fires due to reduced combustion (Ferguson et al., 2003).

Emissions from wildfires have the potential to escape the atmospheric boundary layer (ABL) through lifting mechanisms (Val Martín et al., 2006) like convection, vertical mixing, and/or forced lifting. Regardless of the lifting mechanism, once above the ABL, pollutants can then be transported thousands of kilometers, by being caught in circulation patterns at plume height (Hodzic et al., 2007; Heilman et al., 2014). For example, particulates

1

from fires in remote regions of Canada and Russia have been found over Europe by examining the optical properties of the aerosols (Damoah et al., 2004; Müller et al., 2005; Hodzic et al., 2007) (Figure 1.1). At these large scales, biomass smoke from fires can alter the atmospheric carbon balance, which then changes the optical properties and radiation fluxes within the atmosphere (Houghton et al., 1990, 1995; Levine, 1991, 1996; Ferguson et al., 2003).
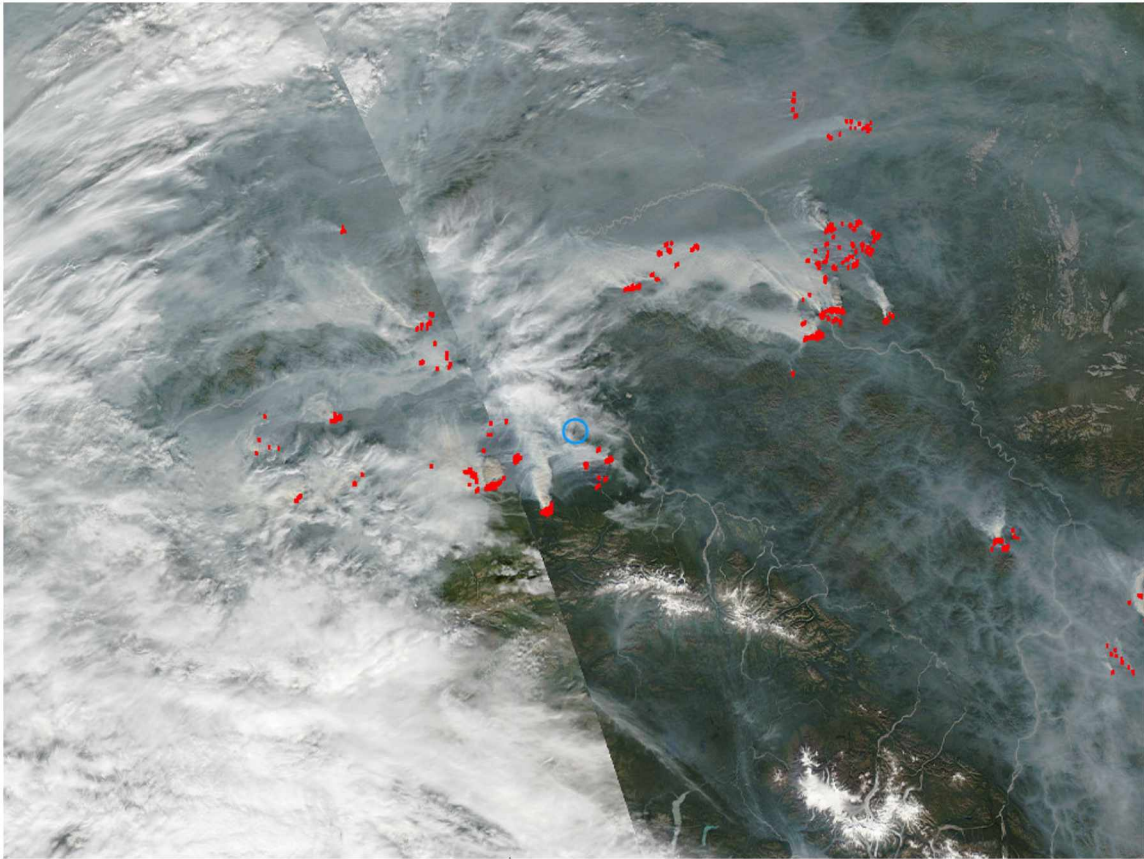
Figure 1.1 Aqua satellite image of wildfire smoke propagating across Alaska, taken on 4 August 2009. The blue circle is the location of the AERONT (AErosol RObotic NETwork) at Bonanza Creek (64.7°N, -148.3°W). Red points are locations of fires. From: NASA EOSDIS (2015)

As a result of degraded air quality from the smoke, health and public safety are at risk (EPA, 2013b). Studies have shown that with an increase in exposure to particulate matter (both $PM_{2.5}$ and PM_{10}) there is an increase in hospital visits due to asthma attacks, and an increase in both clinic and hospital visits due to respiratory symptoms. Bronchitis and chest pains are the most common causes especially to those individuals with preexisting conditions such as chronic obstructive pulmonary disease (COPD) and lung diseases (Mott et al., 2002; Bowman and Johnston, 2005; Kinney, 2008). Due to the high emissions of carbon monoxide released from biomass burning, CO poisoning could occur in persons inhaling smoke; persons could further experience headaches, dizziness, neuropsychological impairment and death (Ward and Hardy, 1991; Weaver, 2009). Manned aircraft can also experience problems when flying through smoke plumes due to a decrease in visibility as well as the effects from thermals (McCreary, 2014)

The majority of Alaska wildfires occur in the area between the Alaska and Brooks Ranges, where boreal forest is present. Approximately 20% of the Alaskan population resides in this area (Olsen et al., 2011; U.S. Census Bureau, 2014).

Within the past four years the population in the State of Alaska has risen by approximately 25,000 people (U.S. Census Bureau, 2014). As the population in the Arctic and subarctic regions rise, more and more people are directly affected by the inhalation of smoke from boreal wildfires, which could have significant consequences on their health.

In addition to health concerns, visibility is greatly reduced by wildfire smoke due to the particulate matter (EPA, 2013a). Visibility can decrease down to 0.2 km or less in extreme cases. Reduction of visibility blocks incoming solar radiation; and which can then lead to changes temperature, relative humidity, and small-scale weather patterns (e.g. Mölders and Kramm, 2007; Shulski and Wendler, 2007).

3

Even after wildfires are finished burning, there can be other lasting environmental effects. A major concern in Arctic regions is the thawing of permafrost. Burn scars have a lower albedo than vegetation covered areas. The lower albedo of fire scars allows for more absorbed heat than over vegetation; as a result permafrost can begin to thaw (Amiro et al., 1999; Mölders and Kramm, 2007). Thawing of permafrost can have lasting consequences. The increase in soil moisture can change vegetation, which can greatly affect precipitation patterns (Chang and Wetzel, 1991; Zhuang et al., 2002; Mölders and Kramm, 2007).

According to McClelland et al. (2004), the thawing of permafrost also leads to an increase of river levels. This increase is not only due to the added groundwater, but also due to the lack of vegetation that would normally prevent strong runoff from precipitation events. In addition to changes in drainage and runoff patterns, there is also the threat of increased sedimentation in the rivers and streams.

If ground vegetation is removed (either by the fire itself or during clean-up efforts) then thawing of permafrost can start and silty sediments can begin to drain into rivers and streams; the sediment transport can occur even if the slope is gradual and erosion is not typical of the area (Lotspeich and Mueller, 1971; Backer et al., 2004). This increase in sedimentation has the potential to affect the aquatic ecosystems by changing water chemistry (Lotspeich and Mueller, 1971; Backer et al., 2004).

Fire scars not only effect the ecosystem, but can also effect meteorological quantities such as net radiation, albedo and heat fluxes that may last about a decade; changes in CO_2 absorption and oxygen released by plants can be seen for approximately 15 years after the fire (Amiro et al., 1999). If these scars are large enough then they can create a non-classical mesoscale circulation from the scar to its adjacent areas. Due to the non-uniform heating and moisture fluxes, convection can occur with graupel formation, graupel formation can create a charge differential in the cloud. As

4

a result, there is the potential to start subsequent wildfires through lightning strikes (Mölders and Kramm, 2007).

The detection of fires has become much easier since satellites have become available in the 1960s, especially in remote regions such as the interior of Alaska. Through the use of the sensors on board of MODIS (Moderate Resolution Imaging Spectroradiometer) and the Terra and Aqua satellites, 82% of fires that were larger than 18 ha were detected for the fire seasons of 2003-2005. However, when conditions are cloudy, or the fires are small, rapidly burning, and/or low in intensity, the possibility of satellite detection decreases (Hawbaker et al., 2008).

By knowing the locations of fires, the probability of them encroaching on populated areas is less likely because they can be watched and potentially extinguished if needed. In addition, knowing the fire location allows better estimates of where the smoke can be advected to can be gained. Furthermore, the location allows conclusion on the chemicals the smoke may contain dependent on the fuel types existing at the location.

Emissions from fires can have immediate and lasting effects on communities and the environment especially in terms of soil and water quality (DeBano et al., 1998). So having a better understanding of the extent of fires and their emissions can allow for an increase in accuracy of both meteorological and smoke forecasts which would aid in fire suppression (Hodzic et al., 2007).

Emissions from wildfires vary depending on the fuel type. Van der Werf et al. (2010) concluded that the greatest variation from emissions result from differences in climate regimes. They examined locations such as boreal Asia, South America, and Indonesia. Carbon emissions give the most variation depending on fuel source ranging from 44% of the emissions in savanna fires to 3% of the total emissions in agricultural waste and tropical peat fires (van der Werf et al., 2010).

Methane is also a key trace gas that can be emitted by wildfires. Its emission varies greatly depending on fuel source. For example, peat fires have the potential to emit ten times more methane than savanna fires (Yokelson et al., 1997; Andreae and Merlet, 2001; Christian et al., 2003; van der Werf et al., 2010).

The interior of Alaska is covered mainly with boreal forests, which is composed primarily of white and black spruce, and paper birch (USGS, 2014). It is in this area that the majority of wildfires occur (Olsen et al., 2011).

1.1 Climate of Interior Alaska

The state of Alaska covers a total of 1,477,262 km². There are extreme climate differences from one portion of the state to the next (Bieniek et al., 2014). The topography of Interior Alaska (Figure 1.2) is composed of two river basins as well as highland areas. Climate in this region is not influenced by the oceans as the mountain ranges block the flow of moisture, making it a region of continental air masses (Shulski and Wendler, 2007).

Continental areas or those leeward of mountains (like Interior Alaska) experience the driest conditions, making these areas extremely prone to wildfires (Johnson and Miyanishi, 2001). Weather in the Interior has low humidity, light irregular precipitation, and large temperature ranges between seasons. For instance, in Fairbanks, the average maximum temperature in July is 23°C and the average minimum temperature in January is -28°C. Wind speeds are typically weak even in summer when they average less than 4 ms⁻¹. In summer, precipitation occurs mostly in the form of scattered rain showers and thunderstorms. With these dry conditions and the high probability of thunderstorms there is high risk for wildfires to ignite by lightning within the Interior (Shulski and Wendler, 2007).
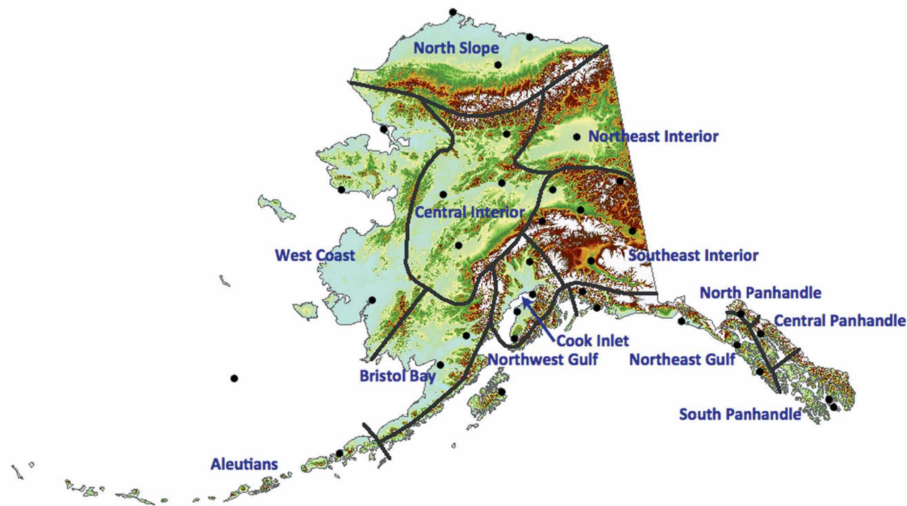
Figure 1.2 Climate divisions of Alaska, dots represent the stations that were used by Bieniek et al. for climatic analysis. (Courtesy of Bieniek et al., 2011)

1.2 Climatology of Alaska Wildfires

Since the 1920s, there has been at least one large fire year per decade in Alaska, averaging to approximately 2.3 large fire years per decade occurring in Alaska. A "large fire year" is defined as a year wherein wildfires burn more than 470,000 ha (Kasischke et al., 2010). There have been times in which there has been an increase in fire activity such as the 2000s when on average 767,000 ha per year were burned (Kasischke et al., 2010). In contrast the inverse between 1860 and 1919 where there were three decades without any large fires in the state (Kasischke et al., 2010). Yet, on average nearly 400,000 ha per year are burned within the state (Kasischke et al., 2010).

The official fire season in Alaska lasts from April 1st to August 31st (Alaska Department of Natural Resources, 2009). Ignition mainly occurs due to human activity (approximately 66%). The percentage of human started fires is typically higher in the spring (April-May) when lightning strikes are uncommon (Mölders and Kramm, 2007; Kasischke et al., 2010). Human

caused fires only account for about 10% of burned area per year (McGuiney et al., 2005; Shulski and Wendler, 2007).

The reason for this difference in area burned is that the human caused fires are typically located close to developed areas. Up to twice as many human caused fires as compared to lightning ignited fires occurred within 20 km of a road or settlement (Kasischke et al., 2010). These fires are typically quickly detected and put out. Whereas, fires started by lightning strikes can occur in remote locations and go undetected until they grow large so they are either detected by satellites and/or their plumes are advected to settlements (McGuiney et al., 2005; Shulski and Wendler, 2007; Hawbaker et al., 2008).

According to Bieniek (2007) there may be a relationship between teleconnections and years of high fire activity. Times when there are strong geopotential height anomalies over Alaska prior to and during the fire season are also times when there is high fire activity; a positive temperature anomaly is also present over Interior Alaska during these high fire events (Bieniek, 2007). However, negative anomalies in geopotential height and/or temperature do not necessarily mean a season of low fire activity will occur (Bieniek, 2007). Despite these trends of large areas burned in the Interior, it is better to examine conditions over synoptic and mesoscale time frames than climatological time frames (Bieniek, 2007).

The majority of lightning activity in Alaska occurs during weak synoptic scale forcing that allows thunderstorms to form over a region for multiple days. Due to the added moisture in these systems, lightning strikes do not typically ignite fires. The majority of the lightning ignited fires start from mesoscale thunderstorms where convection is initiated from topography, differing albedos, changing surface roughness, and changes in heat fluxes (Vidale et al., 1997; Kasischke et al., 2010). The differences in albedo, surface roughness and heat fluxes can be explained with the differences in landuse, especially in areas of patchy forests. Dissing and Verbyla (2003) discussed that the relationship between the boreal forest and the occurrence of

lightning strikes is not by coincidence; the boreal forest coincides with an area already prone to convection, but it also often acts as a trigger mechanism through the variations in surface energy. Despite black spruce is indicative of a cool moist climate, expansion of the boreal forest can create a positive feedback loop with fire occurrence due to the increase in convection (Lynch et al., 2003; Dissing and Verbyla, 2003; Hu et al., 2007).

With climatic changes, summers in northern Interior Alaska have been warmer for the last three decades than in preceding decades (Wendler et al., 2010). The climatic changes have resulted in twice as many large fires in the last 27 years than there was in the first 28 since records were kept in 1955. According to these authors the change in weather patterns is the main reason for such an increase, with more ridges staying over the Interior and clear skies bringing higher temperatures and decreases in relative humidity, and below normal precipitation than before.

1.3 Unmanned Aerial Vehicles

Unmanned Aerial Vehicles (UAVs) were originally developed in the early 1900's for use in combat and surveillance during wars. As time went on and technology improved so did the abilities of UAVs (NOVA/PBS, 2002). Although attempts at using UAVs in science were made by NASA (National Aeronautics and Space Administration) in the 1970s, the use of UAVs did not catch on in the scientific community due to the high costs. But scientific use increased in the early 2000s due to decreased costs and technological advances (Marris, 2013).

UAVs have recently been compared to "low flying satellites" as they can collect high resolution up-to-date images and data from just above the surface (Marris, 2013). Thus, UAVs can be used to detect fires and/or observe smoke spreading when clouds block the view for satellites.

Research using UAVs has been interdisciplinary ranging from subjects such as atmospheric science, geology and biology. UAVs have the ability to fly

anywhere from just above the surface up to 20 km depending on model type (Marris, 2013). In the realm of Earth and environmental sciences, UAVs served to map vegetation, survey waterways for algae plumes, and to fly into and study severe storms such as supercells (Patterson et al., 2005; Dugdale, 2007; Runge et al., 2007; Elston et al., 2011; Knuth and Cassano, 2011; Ezequiel et al., 2014).

In the early 2000s, UAVs were being used by geologists to closely examine volcanic activity as well as thermal conditions within the craters of active volcanoes; allowing for measurements to be taken in real time while not posing a threat to scientists (Patterson et al., 2005). Later, UAVs studied gas plumes from volcanic eruptions.

High Altitude Long Endurance (HALE) UAVs have been developed since 1999 with the idea of using them in the Arctic and Antarctic for sea-ice monitoring (Runge et al., 2007). Solar powered UAVs would be extremely useful as they could hypothetically run forever during polar summer and can be used in areas where fueling is difficult. They are able to remain stationary over an area which would allow for continuous measurement of quantities such as ice depth. HALE UAVs also would have the capability to track ice migration (Runge et al., 2007). In practice, UAVs have been used to monitor the atmospheric conditions off of the Antarctic plateau and how they affect the state of polynyas (Knuth and Cassano, 2011).

When mounted with a camera, UAVs can easily capture images of the Earth's surface, which are extremely useful after events such as storms and earthquakes. UAVs were deployed shortly after Typhoon Haiyan and Bohol Earthquake (Ezquiel et al., 2014). Initially after Typhoon Haiyan, UAVs allowed damage surveys to be taken and to document any changes in landuse/land cover; later they were used to support rehabilitation and relocation.

In terms of seismic activity, UAVs assist in fault-line detection allowing for easier and faster analysis of post earthquake fault movement than is possible from the ground (Ezquiel et al., 2014).

Algae plumes on mudflats on the East Coast of England have been monitored with the use of a standard camera in addition to a near-infrared camera (Dugdale, 2007).

In severe weather when conditions are not suitable for manned aircraft, UAVs have been increasingly used. In 2010, during the Verification of the Origins of Rotation in Tornadoes Experiment 2 (VORTEX2; Elston et al., 2011) in-situ measurements were taken in the rear flank down-draft, as well as the rear flank gust front in order to examine some of the thermodynamic properties of the life cycle of supercells (Elston et al., 2011).

UAVs have the ability to carry a variety of instruments. The number of instruments depends on the exact model of the UAV their weight capacity and flying power (Elston et al., 2015). Typically, UAVs that are equipped with meteorological equipment have the capability to fly up to 1.5 km above ground level (AGL). Equipped with meteorological sensors, they create a high-resolution profile and/or spatial mapping of the environment while collecting temperature, humidity, and turbulence data (Martin et al., 2011).

UAVs can also be equipped with air quality sensors that can collect data from within a fire plume (Kosmatka et al., 2010). UAVs equipped with these instruments have the capability to detect and track a fire plume as well as the plume evolution (Phan and Liu, 2008; Kosmatka et al., 2010). UAVs are able to assist in fire suppression by directly extinguishing a fire or by containing it by dropping fire retardant or water over an area (Phan and Liu, 2008).

Due to the intensity of fires and the inability for humans to go into burning areas and release radiosondes, or for manned aircraft to get close to take measurements, little is known about the vertical distribution of smoke during an active fire (e.g. Ferguson et al., 2003). Due to the bulk of other

sampling methods such as lidar that needs fixed locations (Collins and Cahill, 2000), UAVs would be a viable and cost effective way to study fire emissions especially in remote locations (Ferguson et al., 2003). During the Frostfire study conducted in July 1999 in Interior Alaska, it was determined that sharpest gradients of smoke concentrations occur within the lowest 2 km of the atmosphere. Smoke concentrations were heavily controlled by inversions and local topography (Ferguson et al., 2003). With these local variations in concentrations the use of a UAV would allow for a detailed examination of emissions and variations with time (Ferguson et al., 2003).

In 2009 and 2012 the University of Alaska Fairbanks ACUASI (Alaska Center for Unmanned Aircraft Systems Integration) deployed the UAV ScanEagle into fire plumes from the Crazy Mt. Complex fires in Interior Alaska (2009) and wildfires occurring in Florida's panhandle (2012). These UAVs were equipped with infrared cameras to monitor the fire's location and expansion, and later with instrumentation for aerosol mass concentration sensors for the monitoring of the plume in Florida (ACUASI, 2015a). The use of the UAV in these conditions shows that monitoring and collecting data from wildfire plumes with UAVs is effective.

1.4 Thesis Goal

The goal of this thesis is to examine theoretically how a UAV could provide information about the spatial distributions of mean conditions in a smoke plume. The results of an air quality model will serve as the "known" atmospheric conditions, while a virtual UAV will sample the simulated data at various configurations, heights and speeds. The area chosen for simulated sampling was based off of the mean smoke distribution from the fires. The sampled data are then compared to the mean distributions of the respective mean distributions calculated from model data.

This thesis is also aimed towards determining whether air quality modeling and sampling a forecast for fire plume concentrations can assist in the planning of UAV flight missions.

The virtual UAV is assumed to be a ScanEagle. This UAV has a wingspan of 3.11 m, a length of 1.55 m, and a maximum payload of 3.4 kg (Figure 1.3; INSITU, 2014). The ScanEagle has the capability to fly for over 24 hours when it is at its lightest weight (no payload) and under ideal conditions. Given an instrument load and head wind conditions in this study the ScanEagle is estimated to have an endurance of 20 hours and a cruising speed of 31 m/s.

The ScanEagle has the ability to follow a programed flight path based on latitude/longitude coordinates. This feature allows for simple comparison between UAV recorded data and model output (Jun and D'Andrea, 2003).

Figure 1.3 ScanEagle being launched into the plume of the Crazy Mt. Complex fires by Circle, AK in August 2009. (Courtesy UAF, 2009)

1.5 Thesis Hypothesis

This thesis discusses how the spatial distribution of mean chemical species and meteorological quantities obtained by UAV sampling depend on the sampling pattern, sampling height as well as sampling speed. The hypothesis is *that sampling pattern, sampling height and speed affect the virtually sampled mean spatial distribution of the plume.*

To test this hypothesis, simulated data were obtained by version 3.3 of the Weather Research and Forecasting model coupled with Chemistry (WRF/Chem) (Grell et al., 2005; Skamarock et al., 2008; Peckham et al., 2011) in its Alaska adapted version (Mölders et al., 2010) will be used as "ground truth" in a similar way as in PaiMazumder and Mölders (2009). This means the model results are assumed to represent the actual atmospheric conditions from which the UAV obtains samples and to which the mean spatial distributions obtained by the sampling are compared. The area that the UAV sampled was determined by the mean smoke distribution from the Crazy Mountain complex of fires.

1.6 Brief Layout of the Thesis

WRF/Chem simulated the meteorology and wildfire gases and aerosol propagation; the exact set up and details on initialization, physics and chemistry packages are discussed later in Chapter 2. The WRF/Chem simulation data used in this thesis stem from Tran and Mölders (2012, personal communication).

The Crazy Mountain Complex of fires was used as the testbed. These fires were the main fires in that simulation. This fire complex was ignited on July 31, 2009 in Interior Alaska (65.79°N, 144.5°W), approximately 5 miles (8 km) southwest of Circle, Alaska (Figure 1.4, NWCG, 2009). This fire complex consisted of five main fires the Bluff Creek, Little Black 1, Jagged Ridge, 14 Mile Fire, and Puzzle Gulch fire. This fire complex burned a total of 180,987.8 ha, where the majority of the fuel sources was black spruce and

other hardwoods (AICC, 2009; NWCG, 2009). This fire complex was a threat to 239 structures. The fire and synoptic situation are given in Chapter 2 as well.

The amount of smoke produced in the proximity of the Steese Highway restricted travel along the highway (AICC, 2009). Efforts to contain and extinguish the fires by means of ground and manned aircrafts was extremely limited due to the nature of the smoke being thick.

Prior to using the WRF/Chem data for the UAV study it is needed to demonstrate that the data represents a realistic dataset that describes a fire and smoke situation. This evaluation and its results are in Chapter 3.

In Chapter 3 of this thesis, I assessed the model performance by comparing WRF/Chem cross sections of aerosols and cloud particles with CALIPSO (Cloud-Aerosol Lidar and Infrared Pathfinder Satellite Observation) Level 1B products. This comparison served to evaluate that the model is simulating the spatial distribution of aerosol and cloud presence correctly. Other forms of evaluation included analysis of National Weather Service discussions, METAR (METeorlogical Aerodrome Report) reports, MODIS imagery, as well as surface meteorological observations from the Western Regional Climate Center (WRCC) and Remote Automatic Weather Stations (RAWS). The meteorological quantities of interest for model evaluation were: temperature (T), dewpoint temperature (T_d), and wind direction/speed (**U**).

Air quality is evaluated using data taken at stations monitoring aerosol and particulate matter concentrations; which is also discussed in Chapter 3.

Chapter 4 describes and discusses the results of testing of simulated UAV flights through smoke plumes from the Crazy Mountain Complex of fires.

Chapter 5 encompasses the conclusion, major findings, and recommendations for UAV field campaigns into wildfire plumes.

15
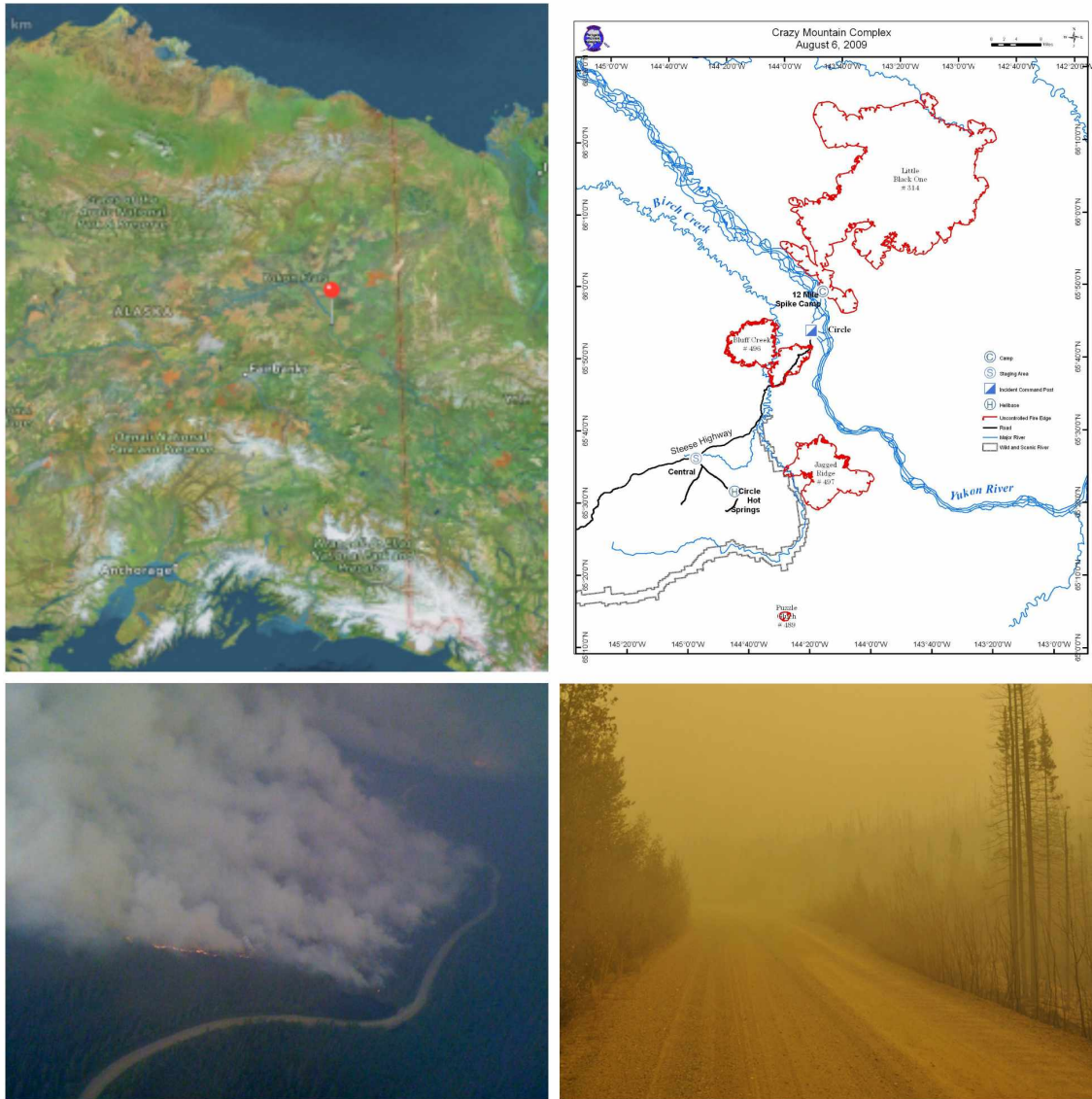
Figure 1.4 Crazy Mountain Fire Complex map and images. Starting in the upper left and working clockwise: Map of Alaska with a point at Circle, AK, Map of Crazy Mountain Complex fires near Circle, AK on 6 August 2009, smoke on road due to Crazy Mountain Complex Fires, and smoke plumes from Crazy Mountain Complex along Steese Highway. (AICC, 2009)

Chapter 2
Experimental Design and Methodology

2.1 WRF

The Weather Research and Forecasting (WRF) model is a high-resolution, limited area, non-hydrostatic, terrain following (with eta coordinates) mesoscale model that is used both operationally and for research (Skamarock et al. 2008). The WRF takes into account the physics and the dynamics of the atmosphere from the surface to the lower stratosphere. The exact vertical levels and the top of the model can be defined by the user. In this case, the top of the model was defined as 100 hPa with 28 vertical layers that increase in thickness with height.

The WRF inline coupled with chemistry packages (WRF/Chem) take into account not only the meteorology, but also the air chemistry, the transport, transformations and removal of chemical species as well as the radiative properties of water substances, aerosols and gases within the atmosphere (Grell et al., 2005; Peckham et al., 2011). WRF/Chem in its Alaska adapted version (Mölders et al., 2011) was used to produce the data used in this thesis.

2.1.1 WRF ARW

The Advanced Research WRF (ARW) is the WRF using the ARW dynamics solver (Skamarock et al., 2008). When used with the meteorological properties of the WRF a complete simulation is formed. The ARW includes the compressible, non-hydrostatic equations, uses prognostic variables such as wind velocity in three dimensions, potential temperature, pressure perturbations, and water in its various phases as well as turbulent kinetic energy and other scalar properties.

The vertical coordinate system is terrain following; whereas the horizontal grid follows an Arakawa C-grid configuration (Figure 2.1). In an Arakawa C-grid configuration, the u and v components lie orthogonal to each

other and the dynamics, mass transfer and chemistry are calculated for the center of the grid cells.

To integrate forward in time, the model uses a third order Runge-Kutta scheme which contains a small time step for the acoustic and gravity wave modes (Skamarock et al., 2008).

In the WRF/Chem, the meteorological values interact with the atmospheric chemistry. This concept allows for the model to consider meteorological and chemical interactions. For example, it can account for the cloud condensation nuclei (CCN) concentrations that affect cloud formation processes as well as droplet sizes that would later affect the chance of precipitation when the modules are chosen accordingly (Barnard et al., 2010). The coupling also accounts for how the cloud species, atmospheric gases and aerosols affect radiative and photochemical properties and reactions that can affect the meteorological conditions (Grell et al., 2005; Peckham et al., 2011).

2.1.1.1 Physics Packages

The WRF has many physics schemes that can be combined in various ways depending on the application. For this simulation, the physics options were chosen to allow for the interaction of the clouds, radiation, and chemistry as used by Grell et al. (2011). Cloud microphysical processes are resolved in the Purdue scheme (Lin et al. 1983). This scheme includes water vapor, ice, snow, and graupel processes, and permits for the co-existence of supercooled cloud water and ice. The processes consider the melting and freezing of raindrops, riming, as well as evaporation, sublimation, deposition, condensation, accretion and aggregation and sedimentation of hydrometeors, among other things (Lin et al., 1983).

Lin et al. (1983) discussed that ice presence and formation play important roles in cloud formation. Due to its complexity the Purdue scheme should be mostly used when the WRF is in research mode, as it allows for

cloud-radiation-chemistry interaction (Barnard et al., 2010). The Purdue scheme deals with the cloud microphysical processes at the resolvable scale.

As convective clouds may be of sub-grid scale at the resolution of the simulations (which was 4 km at a grid increment of 2 km) the Grell-Dévényi scheme (GD) was used. GD is the best choice for high-resolution domains (Skamarock et al., 2008). Inside each grid cell, multiple mass-flux schemes are run. Their output is averaged over each grid cell to provide the impacts of multiple clouds within the grid-column onto the vertical profiles of meteorological quantities within that grid-column. The schemes that are run inside each grid cell differ with their updraft and downdraft parameters as well as precipitation efficiencies. These differences affect the formation of Convective Available Potential Energy (CAPE), moisture convergence, and vertical velocities. With these vertical motion components, the convective inhibition (CIN) is also considered in the formation of convection (Grell and Dévényi, 2002).
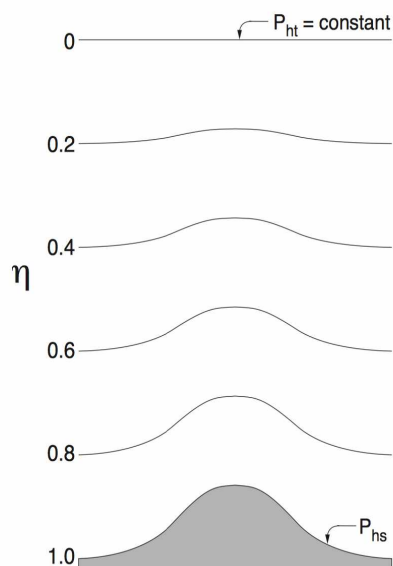
Figure 2.1 Illustration of the terrain-following coordinate system (Skamarock et al., 2008). Here η represents the vertical non-hydrostatic pressure, P_{ht} and P_{hs} are the hydrostatic components of pressure at the top of the atmosphere and at the surface, respectively (Skamarock et al., 2008)

$$\eta = \frac{(p_h - p_{ht})}{\mu} \qquad\qquad \textbf{2.1}$$

$$\mu = p_{hs} - p_{ht} \qquad\qquad \textbf{2.2}$$

Long-wave radiation was parameterized by the Rapid Radiative Transfer Model (RRTM; Mlawer et al., 1997) scheme. The RRTM scheme accounts for multiple bands of absorption with atmospheric trace gases, as well as for cloud optical depth. Values for the RRTM have been based on the line-by-line radiative transfer model (LBLRTM) that provided the absorption coefficients for the cloud species and trace gases (Mlawer et al., 1997).

For the shortwave radiation spectra, the Goddard shortwave scheme was used, where both diffuse and direct solar radiation are considered (Chou and Suarez, 1994). For this study, the scheme that has been used with the modification by Peckham et al. (2011) considered ozone and cloud properties as calculated by WRF/Chem.

The Eta model surface-layer scheme must be run along side the Eta (Mellor-Yamada-Janjić) Atmospheric Boundary Layer (ABL) scheme (Mellor and Yamada 1982; Janjić 1994; Skamarock et al., 2008). As a result, it is commonly referred to as the MYJ scheme (Skamarock et al., 2008). This scheme is based on the work of Monin and Obukhov (1954). Monin and Obukhov simulated the turbulence in the atmosphere due to various surface-layer fluxes from differing frictional properties of vegetation. Within this scheme, a viscous sub-layer is proposed, and it is parameterized for roughness heights for both temperature and humidity (Skamarock et al., 2008).

Due to the use of the Eta model surface-layer scheme the MYJ scheme is also used for the processes within the ABL. The flux profiles are determined for the well-mixed and stable layers, allowing for temperature, moisture (including clouds), and horizontal momentum to be examined in the atmospheric column (Skamarock et al., 2008). The MYJ scheme takes into

account the turbulent kinetic energy (TKE) as well as buoyancy and shear for turbulence formation in the ABL and free atmosphere (Skamarock et al., 2008).

The Rapid Update Cycle (RUC) land-surface model (LSM) (Smirnova et al., 1997; 2000) uses data from the surface-layer scheme, radiation scheme, cloud microphysical scheme, and the cloud convective scheme. This concept allows the exchange of momentum, species, moisture, and heat fluxes at the land-surface-atmosphere interface.

The RUC-LSM includes a one-layer vegetation model, and multilayer snow and soil models. However, like all LSMs available in WRF, the RUC-LSM does not allow for horizontal interaction of surface properties (Skamarock et al., 2008). The RUC-LSM calculates soil temperature, and soil water/ice conditions at six depths under inclusion of frozen ground physics. The RUC-LSM also accounts for canopy effects, as well as snow cover, depth, density and surface albedo as well as snow temperature within the snowpack (Smirnova et al., 1997; Skamarock et al., 2008). The frozen ground and snow processes are important for this study, as Interior Alaska contains large coniferous forests underlain with continuous and discontinuous permafrost, and snow can be present all year especially in high elevations (Shulski and Wendler, 2007).

2.1.1.2 Chemistry Packages

The chemistry packages used in WRF/Chem consider the processes of dry deposition, biogenic emissions, wet deposition, chemical reactions, photolysis, as well as the aerosol physics, dynamics and chemistry. The following chemistry packages were chosen by Tran and Mölders (personal communication 2014) to produce the WRF/Chem simulation data used in this study.

Wesely (1989) developed the surface resistance parameterizations that consider soil and plant characteristics in this WRF/Chem simulation. Dry

21

deposition rates were calculated by multiplying the concentrations in the lowest portion of the atmosphere by the deposition velocities; deposition velocities are calculated as functions of aerodynamic, sub-layer, and surface resistances, among other things. The dry deposition module included the modifications for Alaska that consider dry deposition onto snow and vegetation parameters suitable for Alaska (Mölders et al., 2010).

To handle the gas-phase chemistry occurring in the atmosphere, the Regional Acid Deposition Model, version 2 (RADM2; Chang et al., 1989) chemistry mechanism (Stockwell et al., 1990) is used. Herein, both organic and inorganic chemistry are considered. In total, the RADM2 chemical mechanism considers 14 stable species, four reactive intermediates and three abundant stable species for inorganic atmospheric composition as well as 26 stable species and 16 peroxy radicals for the organic atmospheric composition (Middleton et al., 1990). The chemical mechanism implements chemical reaction rates, emissions, transport and deposition to determine the distribution of gas-phase species and includes treatment of high order alkanes and alkenes, treatment of dicarbonyl and ketones separate from aldehydes (Stockwell et al., 1990).

Furthermore, volatile organic compounds (VOCs) are separated into 32 different classes because of their different reaction rates and properties. Methane, propane, ethane and formaldehyde, propene, acetylene, and acetone are all assigned their own class because of their large concentrations in the atmosphere due to their high emission rates from both natural and anthropogenic sources. Organic acids have their own class due to their ability to acidify the environment. There are two lumped classes for alkane and alkene mixing ratios. The exact reactivity in these classes depends on the exact compounds. There is also an unreactive category where the compounds do not react or react extremely slowly. Finally, there is the unidentified VOC category and an unassigned category for the compounds that are not

commonly found from emissions inside the United States (Middleton et al., 1990).

Primary organic aerosols are any organic aerosols that are released either anthropogenically or naturally into the atmosphere. Whereas secondary organic aerosols (SOA) are particles that experienced gas-phase oxidation of an organic gas and the result was an organic particle (Kanakidou et al., 2005). The organic aerosols are assumed to have a quasi-ideal solution, where a reversible reaction occurs, but the volume and total energy remain constant throughout the reaction (Schell et al., 2001).

The modal aerosol dynamics for Europe (MADE; Ackermann et al., 1995; 1998), which was developed from the regional particulate model (RPM) (Binkowski and Shankar, 1995), serves to calculate aerosol physics. It assigns a particle-size distribution from submicron to course aerosols represented by two log-normal modes. Coagulation, condensation, deposition, and transport are all considered when calculating the concentration of aerosols in the environment (Ackermann et al., 1998).

The secondary organic aerosol model (SORGAM) can simulate SOA formation as well as their low volatility and gas-to-particle conversion by oxidation (Schell et al., 2001). There are currently eight SOA classes parameterized in SORGAM. These classes include anthropogenic and biogenic precursors, alkane and alkene reaction products, products from α-pinene, and the products from limonene degradation (Schell et al., 2001).

The MADE/SORGAM package is particularly useful when dealing with the chemical emissions from fires as this scheme considers a wide spectrum of the organic compounds released during burning of organic fuels.

Due to the simulation used in this thesis having been run in the high latitudes for the warm season where it is daylight for all or most of the day, photolytic reactions are very important to consider. Certain chemical compounds will disassociate into their constituents at certain wavelengths because of their absorption of the light's energy. For the gas-phase chemistry

23

21 photochemical reactions are considered within each grid cell, and the frequency of photolysis is a function of wavelength, temperature, species, and absorption cross section among other things (Madronich, 1987).

Biogenic emissions depend on landuse. The Guenther et al. (1994) and Simpson et al. (1995) biomass-emission scheme was used to account for biogenic emissions. This scheme utilizes the average biomass emissions from various forms of vegetation depending on vegetation density. The biomass emissions are mostly of the VOC variety. Emission rates are dependent on leaf type, light intensity, canopy effects, and leaf and soil temperature. Furthermore, this scheme considers the emissions of NO from soil bacteria as a function of soil conditions.

Biomass burning is considered in accord with Freijtas et al. (1996) and Grell et al. (2011). According to the National Research Council (NRC), 71.44% of emissions from biomass burning in wildfires are released in the form of carbon dioxide (CO_2), and 20.97% is water. VOCs make up 0.24% of the fire emissions, and $PM_{2.5}$ makes up 0.47% of fire emissions (NRC, 2004; Liu et al., 2014).

The wildfire emissions were updated in the WRF/Chem model each day as the fire progressed. The locations of the fires and their temporal progress stem from the MODIS wildfire database (NASA EOSDIS, 2015).

Along with the wildfire emissions, VOCs will also be released from anthropogenic sources. Most of these sources are from oil and natural gas production, which is a huge industry in the State of Alaska, but occurs only at very localized areas. These emissions are typically in the form of paraffins, olefins, aromatics, aldehydes, and marginally reactive compounds (Piccot et al., 1992). Furthermore, VOC is released from traffic, power generation, and other industrial processes. The anthropogenic emissions stem from the EDGAR (Emission Database for Global Atmospheric Research) emission inventory which provides annual emissions of greenhouse and precursor gases on a $1° \times 1°$ (EC-JRC/PBL, 2014). Due to Alaska's sparse population,

anthropogenic emissions have more the characteristics of local spots like point sources than area sources like in the contiguous US (Leelasakultum et al., 2012).

2.1.2 Model Domain and Initialization

The WRF/Chem model domain was centered over Interior Alaska (65.57 °N, 145.9 °W); with 120 × 110 grid points in west-east and north-south direction. At each boundary, five grid cells served for relaxation of the downscaled boundary values and therefore were omitted from the analysis. Thus, the domain of interest encompassed 110 × 100 grid points. This domain extended into the western portion of the Yukon Territory. Notable features within the domain are the cities (with respective 2010 population; U.S. Census Bureau, 2014) of Fairbanks (31,535), North Pole (2,117), and Circle (104), and portions of the Arctic National Wildlife Refuge (Figure 2.2). The model was run at 4 km increments, a time step of 24 seconds, and on a vertically stretched grid from the surface to 100 hPa with 28 vertical layers.

The initial and boundary conditions for the meteorological quantities were retrieved from the National Centers for Environmental Prediction (NCEP) 1°×1° 6 hour resolution global final analyses (NCEP, 2000).

WRF/Chem simulations existed for 3 August 2009 to 10 August 2009 for a total of eight days (Mölders, 2014; personal correspondence). The meteorological fields were reinitialized every five days. The chemistry was initialized by idealized vertical profiles that correspond to Alaska background concentrations of the various chemical species (Mölders et al., 2010). These same profiles were also used as the lateral boundary conditions for the chemical fields.

Data from 6 to 10 August are considered for the evaluation of the chemical species and aerosol distributions. The first two days of the simulation were discarded for spin up of the chemical fields.

The chemical fields and meteorological conditions must be correct during the time of the chemical spin up. In case of the meteorology, the evaluation was performed for the entire timeframe (3-10 August 2009) and the 110×100 domain.
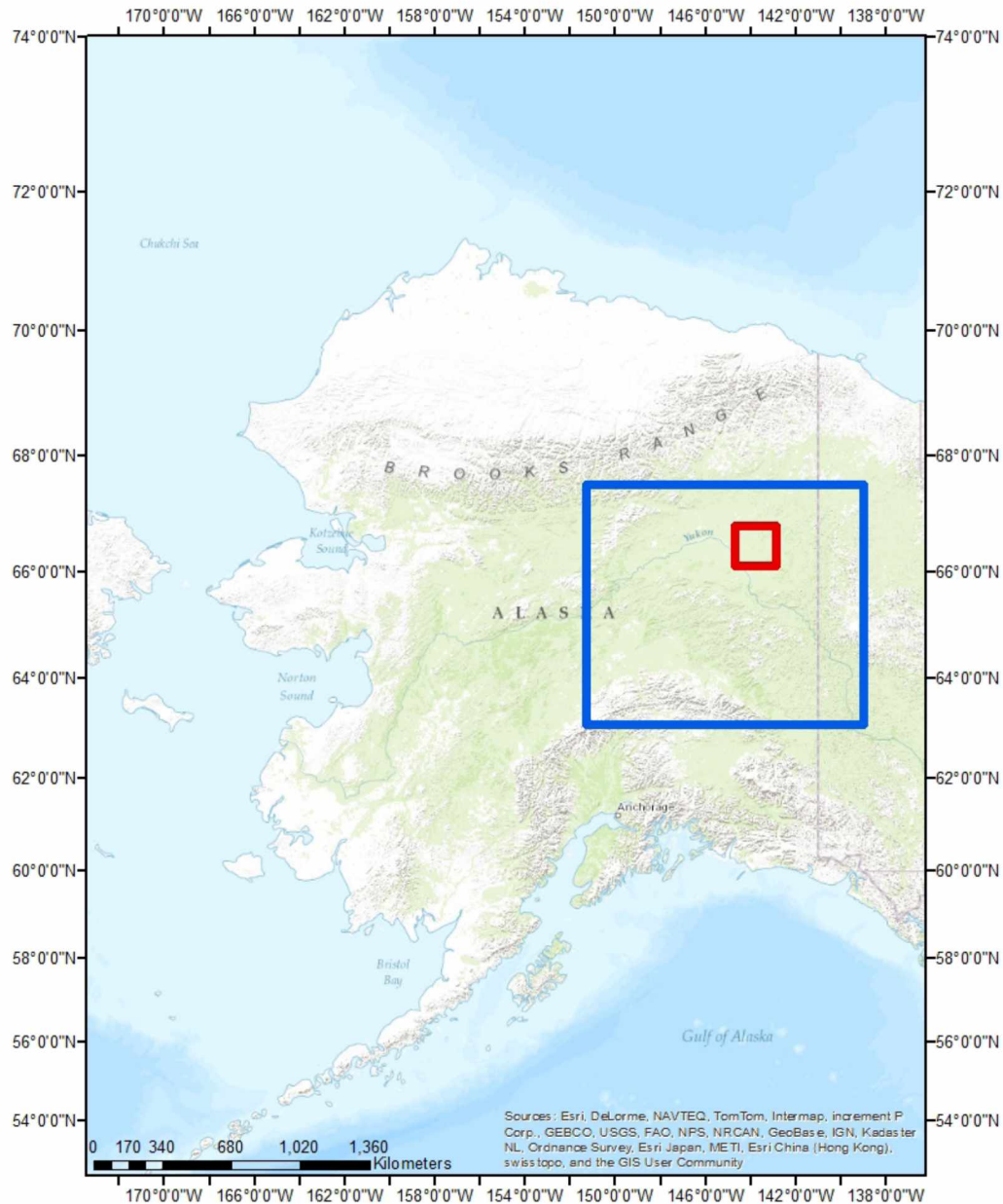
Figure 2.2 WRF/Chem domain and UAV domain. Blue box represents the WRF/Chem domain. The red box is the UAV sampling domain for the Crazy Mountain Complex fires. See text for further information.
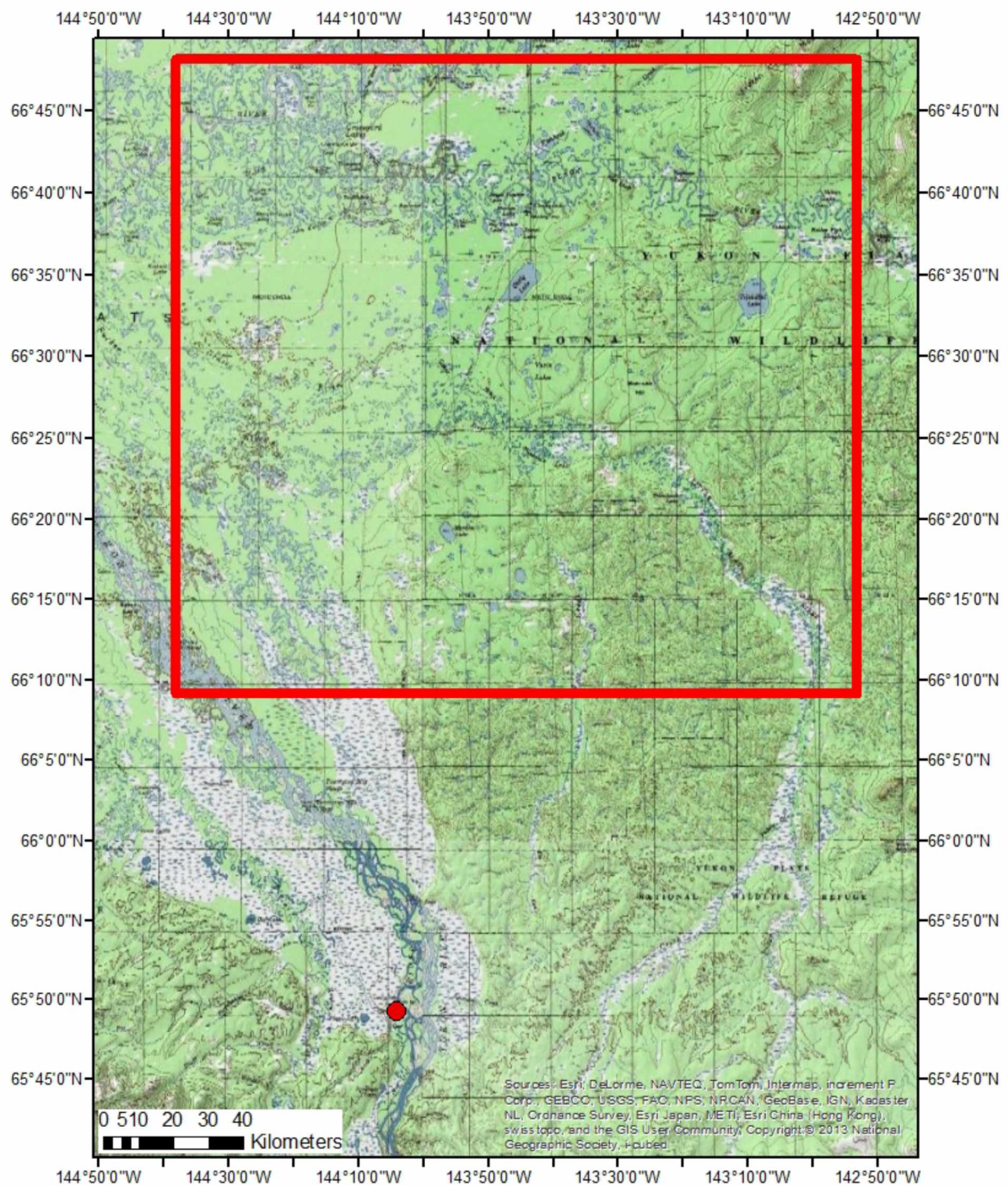
Figure 2.3 Topographic map of the UAV domain within the red box. The red dot is Circle, AK. (Base map courtesy of ESRI)

2.2 Synoptic Conditions

Knowing and understanding the large-scale synoptic conditions is key to assess wildfire development and spreading as well as plume propagation. A week prior to the study timeframe, a weak low-pressure system was consistently present in Interior Alaska with haze and scattered light rain showers. Concurrently, a comparatively stronger low formed over the Aleutian Islands. By the first of August, a ridge of high pressure began to move into the Interior, with clearing skies and cool air and low dewpoint temperatures.

Conditions in the Interior on August 3rd were mostly cloudy, but hot and dry at the surface with temperatures between 17 and 20°C with dewpoint temperatures between -1 and 9°C. High pressure was situated at the coastline in the Gulf of Alaska with a northwestward tilting ridge into the Interior. Weak low-pressure systems were approaching from the west and propagating inland.

Just a day later, the lows to the north and west had deteriorated and the high strengthened, with the ridge now extending from the Gulf of Alaska to the Brooks Range. In the Interior, winds were from variable directions and weak. Skies were mostly clear with increased cloudiness along the western coast of Alaska and along the Brooks Range. Dewpoint temperatures were still between 0 to 9°C over the Interior and air temperatures were in the low to mid 20s (°C). The low over the Aleutians deepened to 997 hPa and moved eastward. At this time, the system was fully matured and started to occlude by the end of August 4th.

By August 6th the center of the 1006 hPa low was located over Interior Alaska with scattered light rain showers. Temperatures had fallen to 15°C with increased dewpoint temperatures. At this time, winds had decreased to values between 0 and 2.5 m/s.

August 7th to 9th was a transition period for synoptic conditions. The low continued to weaken and moved eastward. Temperatures remained low but with gradually clearing skies.

On August 8th, the low–pressure system propagated northeastward toward the Interior, while rain showers were present along the coast of the Gulf of Alaska, but skies were mostly clear and with temperatures close to 20°C, and dewpoint temperatures were gradually increasing as the low propagated northeasterly. Winds were variable in direction in the Interior, but wind speeds increased to 5 m/s.

August 10th brought a drop in dewpoint temperatures (down to -5°C) and an increase in wind speeds of up to 10m/s, which resulted from the new high-pressure system over the Interior.

In summary, the synoptic pattern during the time examined in this thesis was an oscillation between high and low pressure in the Interior. Lows continually formed around the Aleutian Islands, and propagated eastward into Interior Alaska. When the high pressure centered over the coast of the Gulf of Alaska strengthened, the ridge extended over the Alaska Range into the Interior up to the Brooks Range. During the time of transition between high and low-pressure systems, winds increased, while dewpoint temperatures remained low and air temperatures remained near 20°C. These are prime conditions for wildfire formation and expansion (UCAR, 2012).

2.3 Model Evaluation Techniques

It is important to determine the accuracy of the meteorology by comparing the meteorological output to observed values before even considering the WRF/Chem-simulated chemical species and aerosol data (Chapman et al., 2009). The near-surface meteorological variables of temperature including daily minimum and maximum, dewpoint temperature, wind speed and direction observed at 33 sites were used for model evaluation. Other meteorological quantities such as surface pressure and precipitation

were not considered in the model evaluation due to too few observations within the domain and/or in time for reasonable skill-score statistics.

Due to Interior Alaska's low population density and the general remoteness of the area, observations are few and biased to locations with human settlements (Figure 2.4). In order to fill in gaps and be able to have a meaningful evaluation, meteorological quantities were taken from multiple sources: Data from 33 remote automatic weather stations (RAWS) were downloaded from the Western Region Climate Center (WRCC). Data from six automated surface observing systems (ASOS) were provided by the National Climatic Data Center (NCDC), and data from nine snow telemetry (SNOTEL) sites were provided by the United States Department of Agriculture's Natural Resources Conservation Service. All stations considered in my evaluation have a sufficient number of observations for a statistically meaningful performance evaluation.

Evaluation of the model was conducted using the statistical skill scores (e.g. von Storch and Zwiers, 2001) of bias (simulated vs. observed), root mean square error (RMSE), standard deviation of error (SDE), and correlation-skill score. Biases show the model's systematic errors from approximations, assumptions, and parameterization (Mölders, 2008). RMSE takes into account bias and variance, weighting the outlying data more heavily. Thus, RMSE is a good tool for determining model accuracy (Jiang et al., 2008; Mölders, 2008). The SDE takes into account random errors from the model that occur due to uncertainties in observations, boundary and initial conditions (Mölders, 2008). Correlation-skill scores show how well the model simulates data as compared to the observed values.

Near surface simulated $PM_{2.5}$ was compared to $PM_{2.5}$ concentrations that were recorded in Fairbanks, AK. Statistical skill scores of fractional bias (FB) as well as normalized mean error (NME) were used for the model evaluation of chemistry.

30
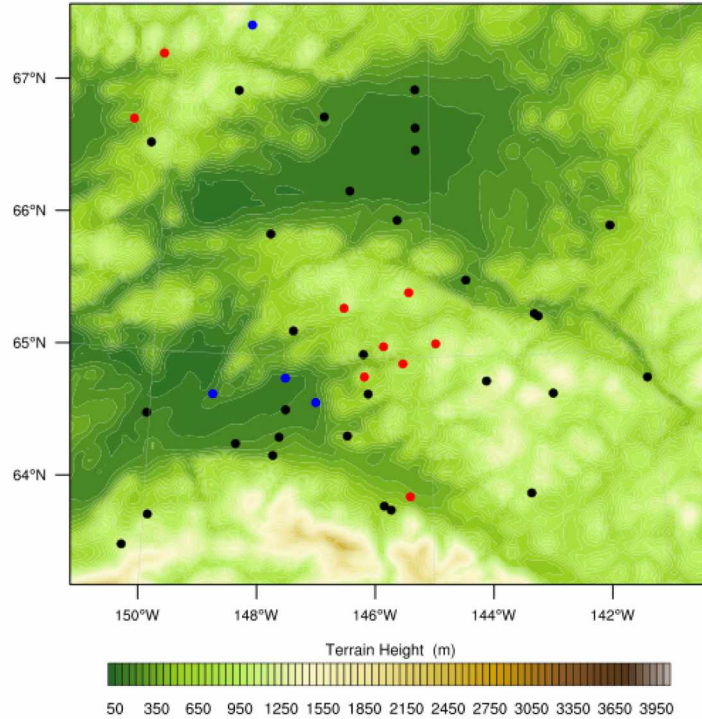
Figure 2.4 Model domain showing terrain height in meters, as well as the locations of surface observation sites. Black – RAWS, Blue – ASOS, Red – SNOTEL. See text for further information.

2.4 CALIPSO

Presently, the only direct detection of aerosols on a continual basis in the atmosphere is through surface stations. As these observations are limited in space and can only collect data at the surface, Cloud-Aerosol Lidar and Infrared Pathfinder Satellite Observation (CALIPSO) level 1B backscatter and depolarization data is analyzed for qualitative evaluation of the WRF/Chem performance in the vertical along the lidar curtains.

The CALIPSO was designed to provide vertical profiles of clouds and aerosol layers. CALIPSO has a Cloud-Aerosol Lidar with Orthogonal Polarization (CALIOP), Imaging Infrared Radiometer (IIR), and a Wide Field Camera (WFC) on board (McCormick, 2005).

CALIPSO is part of the "A-train constellation". The A-train refers to the group of polar orbiting satellites (Aqua, CloudSat, CALIPSO, PARASOL,

and Aura) that pass over the equator at roughly 1:30 pm local time (Figure 2.5). This group of satellites travels closely together, recording information on the atmospheric profile (Figure 2.5). This constellation assesses various atmospheric characteristics at the same time.
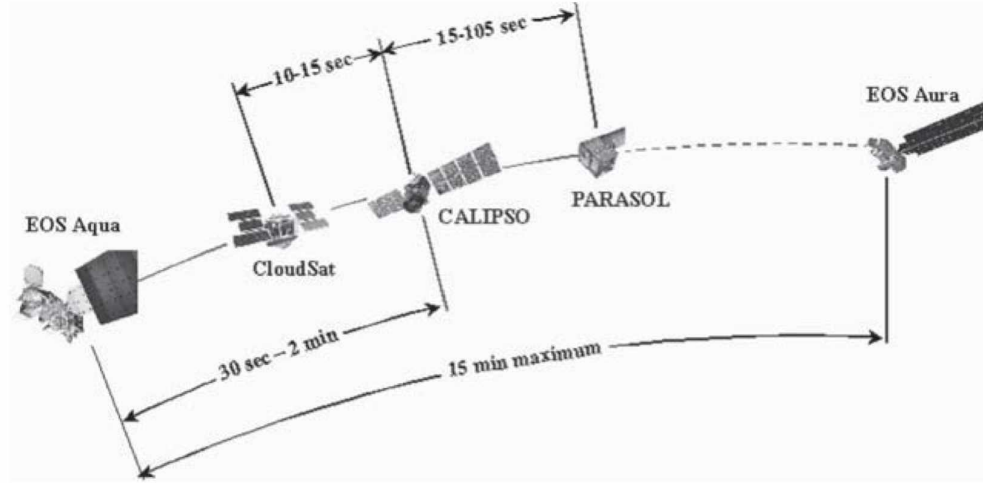
Figure 2.5 The five satellites of the "A-train constellation" in their correct configuration. Also shown is the time difference between when a particular satellite goes over an area. Notice that the time for the entire A-train to pass over an area is 15 minutes. From: McCormick (2005)

CALIOP collects the backscatter and depolarization data that were compared with WRF/Chem vertical profiles of particulate matter of 10 μm or less in diameter in this thesis. CALIOP emits pulses of polarized light at 1064 and 532 nm. The 532 nm return signal is received in two orthogonal components (parallel and perpendicular to the original pulse) (McCormick, 2005). The backscattering coefficient (Equation 2.1) of the lidar signal (β) is the primary data of CALIOP. The backscattering coefficient is a function of the concentration of scattering particles (N) of a certain type (j), in the volume the laser passes through, and the differential backscattering cross section at a particular wavelength ($d\sigma/d\Omega$) (Wandinger, 2005).

$$\beta(R,\lambda) = \sum_j N_j(R) \frac{d\sigma_{j,sca}}{d\Omega}(\pi,\lambda) \qquad \textbf{2.3}$$

32

The backscattering power that is sent back to the lidar, is a function of the power sent out (P_o), the lidar-system constant (K), the backscatter coefficient, the volume extinction coefficient (σ), range (R) which is a function of the perpendicular ($\perp$) and parallel ($\parallel$) polarization planes with respect to the initial orientation of the transmitted signal given by (Sassen and Khvorostyanov, 2008).

$$P(R)_{\perp,\parallel} e^{(-2\int \sigma(R)dR)/R^2} \qquad\qquad \textbf{2.4}$$

If particles are spherical in nature, no backscattering would occur in the perpendicular or parallel planes. Thus, irregular shaped particles, such as those found in smoke, would have some orthogonal backscattered values (Hu et al., 2007). The linear depolarization ratio (δ) is simply the ratio of the perpendicular backscatter power return over the parallel backscatter power return (Equation 2.3). The contributions from all the molecular, aerosol, and cloud species are included in both power returns. Despite backscattering from clouds dominates the power returns, the combination from aerosols and molecules can produce δ values between that of the pristine atmosphere and that of a particular aerosol type (Sassen and Khvorostyanov, 2008). Particle size can also impact the depolarization values. Particles that are approximately the same size (or larger) as the wavelength from the lidar, produce the highest δ values (Mishchenko and Sassen, 1998; Sassen and Khvorostyanov, 2008)

$$\delta = \frac{P(R)_\perp}{P(R)_\parallel} = \frac{[\beta_m(R)_\perp + \beta_a(R)_\perp + \beta_c(R)_\perp]}{[\beta_m(R)_\parallel + \beta_a(R)_\parallel + \beta_c(R)_\parallel]} \qquad\qquad \textbf{2.5}$$

In terms of smoke studies, δ values are close to zero for fresh smoke. Aged smoke particles have higher δ values than what would be expected for spherical particles in the atmosphere; showing that crystallization of aqueous drops onto the smoke particles occurred during transport (Wandinger et al.,

33

2002; Murayama et al., 2004; Sassen and Khvorostyanov, 2008). Sassen (2002) concluded that smoke layers are dominated by spherical aqueous drops, and as a result, δ values are typically very low; although ash fallout and crystallization can lead to elevated values (~0.1).

2.4.1 CALIOP and Model Evaluation

CALIPSO data (both backscatter and depolarization) can be compared with the WRF/Chem cross sections of PM_{10} (e.g. Madden, 2014). This comparison not only allows for an examination of the simulated smoke plumes in the vertical and in one horizontal direction, but also allows for the WRF/Chem simulations to be assessed with satellite data. These comparisons can only be made along the same latitude/longitude path that the CALIPSO satellite followed. The times in which the satellite passed over the fire and/or plume directly were chosen for display in the analysis, but all overpasses were compared and discussed.

2.5 UAV Sampling Assessment Study

The UAV sampling domain is set up as a 60 km × 60 km grid. This size was chosen based on the ScanEagle's cruising speed (111 km/hr) and flying time with payload (20 hours). The domain is located over the Crazy Mountain Complex of fires (Figure 2.2).

The WRF/Chem simulated values were assumed to be the 'grand truth' of the meteorological and chemical conditions during the wildfires. Values of meteorological quantities, selected wildfire emitted trace gases, secondary pollutants, and particulate matter were extracted from the WRF/Chem simulations.

2.5.1 Sampling Strategies

Due to the weight of instrumentation, the only meteorological fields assumed to be sampled from the 'grand truth' were temperature and dewpoint temperature. The chemical constituents considered in the UAV sampling studies consist of

1. CO as a representative for inert tracers emitted by wildfires
2. SO_2, and NO as representatives for aerosol precursor gases
3. O_3 as a representative for secondary pollutants
4. PM_{10} and $PM_{2.5}$ that are emitted, but also produced in the atmosphere by gas-to-particle conversion from various precursor gases (Seinfeld and Pandis, 2006)

To test the hypothesis that *the distributions of the various quantities depend on the sampling pattern, height, and speed*, a sampling pattern as shown in Figure 2.6 was assumed. The WRF/Chem values that are to represent "measurements" were taken along the pattern at different temporal resolution, i.e. speed. Furthermore, the data were taken along the pattern starting at different points and reversing the direction in which the data were sampled by the assumed UAV from the WRF/Chem data. Sampling was also performed at various heights.

There are two halves of each flight, the first Half of Flight Path (HOFP) was the flight from the starting point to the opposite corner (the red path in Figure 2.6). The second HOFP begins where the UAV starts its return to the starting position (blue path in Figure 2.6). The initial UAV path follows a mainly longitudinal path along the sampling domain. Once located in the northeast corner, it flies a mainly latitudinal path (Figure 2.6a).

The UAV sampling flights were examined at 200 m, 500 m, and 1000 m altitude. Herein, 200 m is the lowest height a UAV could fly in Interior Alaska due to turbulence caused by high vegetation, and 1000 m is the highest height a UAV could ascend without consuming large amounts of fuel (INSITU, 2014). The latter is around the top of the ABL.
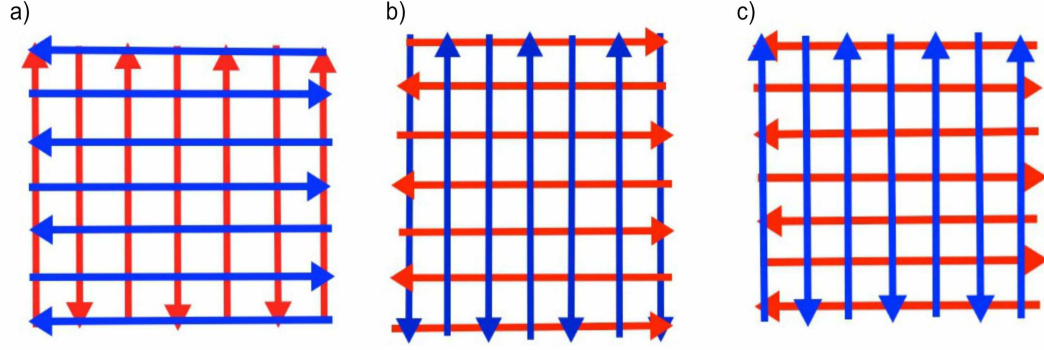
Figure 2.6 UAV sampling patterns' initial direction is given in red, and the second direction in blue. a) Initial flight path starting in the SW corner with initial longitudinal sampling. b) Second sampling pattern starting in the SW corner but sampling latitudinally until reaching the NE corner, and then sampling longitudinally. c) Third sampling pattern starting in the NE corner sampling latitudinally to the SW and then longitudinally back to the NE.

Winds up to the 5 km height were examined in order to determine if they would be strong enough to force the ScanEagle off course; i.e. out of a 4 km × 4 km grid cell. Due to the UAVs weight and its ability to follow a pre-programed course, head, tail, or side winds at all heights below 5 km were not a factor to bringing the UAV off course. However, these winds, of course, were considered in calculating the UAVs actual speed over ground, i.e. with strong head winds, for instance, the UAV samples longer in a grid cell than with no head winds, tail winds and/or side winds.

Since the WRF/Chem data were recorded at one-hour intervals, the sampled quantities were interpolated between available WRF/Chem data as a time-weighted average

$$C_{sampled} = \left(1 - \frac{\Delta t}{3600}\right) \cdot C_t = T \cdot c_t \frac{\Delta t}{3600} \qquad \textbf{2.6}$$

where Δt is the time since the last full hour t-1, and t is the time at which the next hourly WRF/Chem data are available. Furthermore, C stands for the sampled meteorological quantity or chemical constituent.

The path of the UAV was changed to see if the sampling pattern influences the 20 hour mean spatial distributions constructed from the sampled values. The pattern was inverted rather than starting in the southwest corner and traveling in the longitudinal direction; meaning a dominantly latitudinal initial path is followed by a dominantly longitudinal one (Figure 2.6b). Also a complete reversal of flight path was conducted by starting in the northeast corner of the UAV sampling domain and traveling latitudinally first and then longitudinally to the southwest corner (Figure 2.6c).

The final variation in the UAV sampling mode concerns flight velocity. Instead of the cruising speed of 111 km/hr, sampling is once assumed at the stall speed of 72 km/hr and then at the maximum speed of 148 km/hr. With the change in speed of the UAV the time it takes to cover the entire sampling domain also changes. With the cruising speed the UAV covers the sampling domain in 20 hours, with the fastest speed 14 hours, and with the stall speed 28 hours. Despite the time it takes for the UAV to cover the entire sampling domain all sampling results are compared to the 20 hour average or 'grand truth' value.

To keep a uniform comparison to the 'grand truth' value the data that was recorded after the 20th hour was not considered for statistical analysis as these hours were not considered for the 'grand truth'. The same principle was applied when the UAV was travelling at its minimum speed except statistical analysis was compared to a 14 hour average. While changing the velocity of the UAV, it is important to remember that the sensitivity of instruments on board must allow for the new speed. Flying at a higher speed requires higher sampling rates to achieve similar accuracy than with slower speed. However, instrumentation that has high sensitivity often has more weight and the maximum payload of the UAV must be considered (Elston et al., 2015).

In all cases, differences and similarities between the temporal mean spatial distributions of "sampled" meteorological quantities, gases and particulate matter and the temporal mean spatial distribution calculated from the 'grand truth' WRF/Chem data are examined to test the research hypothesis. Note that here 'temporal mean' refers to the mean over the entire UAV flight duration.

2.5.2 Assesment of Spatial Distributions

In order to assess the spatial distributions of the temporal mean derived from the UAV sampled data by means of the 'grand truth' the 20 hour average of each quantity was calculated from the WRF/Chem data. Note that the mean is taken over 20 hours, and not 24 hours is a result of the limited flight time for the UAV to travel the sampling domain at its cruising speed. The WRF/Chem mean 20 hour distribution is then used as the "true" picture of the environment that is used for the calculations of the skill scores between the mean distribution derived from the sampled quantities obtained for different flight paths heights, patterns, and speeds. This assment method follows PaiMazumder and Mölders (2009).

Differences in the temporal mean spatial distribution derived from the sampled values and those of the 20 hour mean determined from the WRF/Chem data were expressed in terms of normalized mean biases (NMB) and fractional mean biases (FB) following Chang and Hanna (2004). For atmospheric models it is considered to be good if the relative mean bias is less than 30% at the 95% confidence level, for the fractional bias values that are within a factor of two of the observations is condidered to be accurate (Chang and Hanna, 2004).

$$NMB = \frac{1}{N}\sum_{i=1}^{N}\frac{(S_i - g_i)}{g_i} \qquad\qquad \textbf{2.7}$$

$$FB = \frac{1}{N}\sum_{i=1}^{N}\frac{(S_i - g_i)}{(\frac{S_i + g_i}{2})} \qquad\qquad \textbf{2.8}$$

38

Where S is for sampled and g is the 'grand truth', N is the number of samples and i is the time interval.

The NMB is useful for model analysis as it creates an equal distribution, and does not inflate the observed ranges of concentrations. This is especially true with low concentrations. The FB is used because it has equal weighting of positive and negative biases (EPA, 2009).

Chapter 3

Evaluation

Before any use of model data for investigations regarding the sampling from UAVs, it is imperative to determine if the model data represents a realistic picture of the environment. In order to determine model accuracy: 2 m air temperature, 2 m dewpoint temperature, 10 m wind speed and direction were evaluated by using the root mean square error (RMSE), standard deviation error (SDE), bias (simulated vs. observed) and correlation-skill score.

Unfortunately, radiosonde data from 4-6 August possibly had calibration errors (Plumb, 2015; personal communications). There were no launches after 6 August until the end of the episode under study because the radiosonde system was switched over from the automated theodolite system to GPS (Global Positioning System) monitoring. Therefore, no evaluation of WRF/Chem's performance with respect to the vertical profiles of temperature, dewpoint temperature, wind speed and wind direction could be performed.

To assess the chemistry model data was compared to surface air quality observations of $PM_{2.5}$ as well as PM_{10}. WRF/Chem cross sections for PM_{10} which includes $PM_{2.5}$, were also compared to CALIPSO level 1B products.

3.1 Meteorological Quantities

Meteorological quantities were extracted from the WRF/Chem data at the locations of surface sites throughout the model domain. In total, there were 33 sites that provided meteorological data for the 2 m air temperatures of 3 to 10 August 2009. Only 2 m air temperature, 2 m dewpoint temperature, 10 m wind speed and direction were examined. Surface pressure and downward shortwave radiation were omitted due to a lack of sufficient sites and data.

3.1.1 Temperature

During the study period, the model consistently overestimated the hourly spatial average 2 m temperature in the model domain, leading to an overall bias of 2.7 K, RMSE of 4.9 K, SDE of 4.1 K and a correlation-skill score of 0.74 (Table 3.1). Despite this relatively good correlation there are high random errors in simulated 2 m air temperature as is indicated by the large values for RMSE and SDE.

The model data show a diurnal cycle as well as the passage of the cold front on 6 August, but these signals are dampened when compared to those from the surface observations, by a maximum of 2 K. Over the episode the diurnal course is overestimated by 3 K on average, with an overestimation of both the maximum and minimum 2 m air temperature. This means the ABL is too warm overall, with little variation between the maximum and minimum temperatures (Figure 3.1).

Similar errors and dampening of the diurnal cycle were found in past WRF studies (Mölders 2008; Hines and Bromwich 2008; PaiMazumder and Mölders 2009; Mölders et al., 2011; Madden, 2014)

These errors could come from a variety of sources. The model could possibly be overestimating the incoming solar shortwave radiation. There were no stations inside the WRF/Chem domain that recorded downward shortwave radiation, only nine stations recorded net radiation. With the lack of downward radiation it cannot be determined if temperature errors are a result of errors in the incoming shortwave radiation.

WRF/Chem does not represent the terrain exactly due to the average terrain height within a grid cell being used as terrain height of the grid cell. Furthermore, the strategy of dominant landuse in a grid cell is used. The smoothed terrain and more homogeneous surface in the model than in nature will affect the temperatures when compared to the surface stations yielding a difference in station and model data (e.g. Avissar and Pielke, 1989; Mölders et al., 1996; Skamarock et al. 2008; Mölders, 2011).
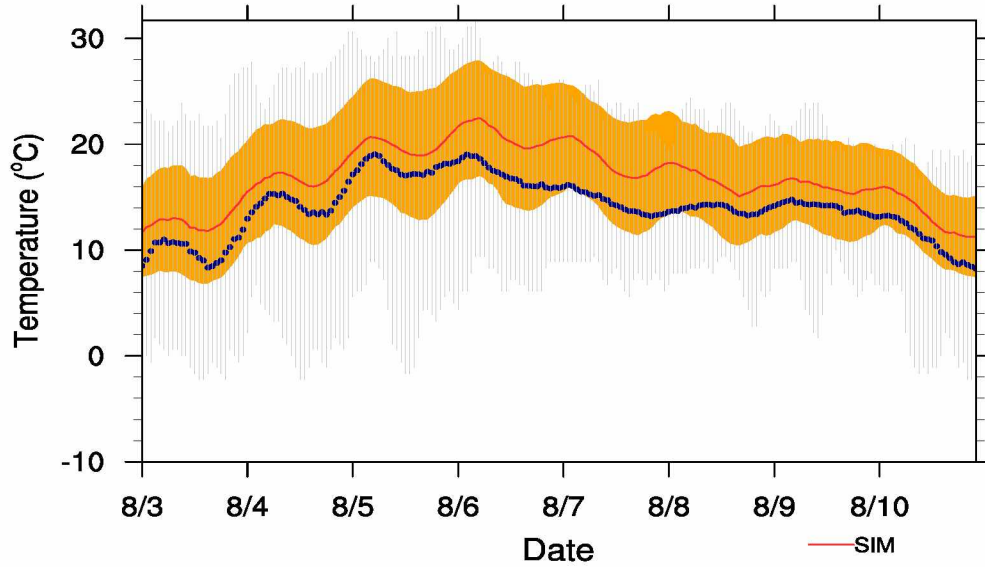
Figure 3.1 Spatial hourly averages of temperature for the 33 sites in the domain during 3-10 August 2009. Blue dots represent the spatial average WRF/Chem 2 m air temperatures, the red line is the spatial hourly average of simulated temperatures, the grey lines are the mean standard deviation from the mean observed values over all the sites. The orange shading is the mean standard deviation of simulated values over all sites.

The documented warm bias affects other meteorological quantities. Relative humidity will be too low when the atmosphere is too warm. Unfortunately, relative humidity is a key quantity when dealing with wildfires. As a result of too high air temperatures, cloud and precipitation formation may be underestimated if the overestimation also remains with height. However, this question cannot be answered as precipitation was as showers, not all sites recorded precipitation and if, the recording timeframes differed among the sites of the different networks.

Table 3.1 Means, standard deviation of simulated and observed quantities as well as skill scores over 33 sites within the model domain. The simulated and observed columns give the hourly spatial average of each variable and its ± standard deviation, followed by the RMSE, SDE, bias, and correlation for the variables discussed in section 3.1.

Averaged Hourly Statistic						
Variable	**Simulated**	**Observed**	**RMSE**	**SDE**	**Bias**	**Correlation**
T (°C)	16.9±5.6	14.1±5.7	4.9	4.1	2.7	0.7
T$_d$ (°C)	7.1±4.2	7.1±4.6	3.6	3.6	~0	0.7
U (m/s)	3.4±1.6	3.3±6.2	6.2	6.2	0.1	0.1
Dir. (°)	190±106	166±104	115	111	15	0.4

3.1.2 Dewpoint Temperature

WRF/Chem simulates dewpoint temperatures acceptably, with the lowest RMSE, SDE, and bias being 3.6°C, 3.6°C, and ~0°C respectively. The correlation was one of the highest of the meteorological variables with a correlation of 0.7. Similar results were seen in Mölders (2008) Hines et al., (2011) Mölders et al., (2011) Mölders et al. (2012) and Madden (2014).

On 4 August, there was an increase of mean standard deviations of dewpoint temperatures. This increase is likely due to the low-pressure system that was centered over the Central Aleutian Islands bringing moisture into the Brooks Range area leaving the central Interior with dry air and clear skies (Figure 3.2). Other than this day, spatial mean standard deviations in dewpoint temperatures are fairly consistent over time (Figure 3.3).

Other errors are likely produced by inaccurate soil and moisture fluxes possibly due to inconsistencies between WRF/Chem assumed and actual landuse/cover. In the model domain, the landuse/cover is broadly categorized, for example landuse is automatically categorized as a coniferous forest rather than spruce forest. These differences may seem minute, but can make large

44

differences of moisture, heat, matter, and momentum fluxes (Mölders, 2011). Intuitively, the broad category of coniferous forest includes all pine types. Pines can be considerably larger than spruce trees, and hence create different amounts of evapotranspiration, sensible heat flux densities and friction.
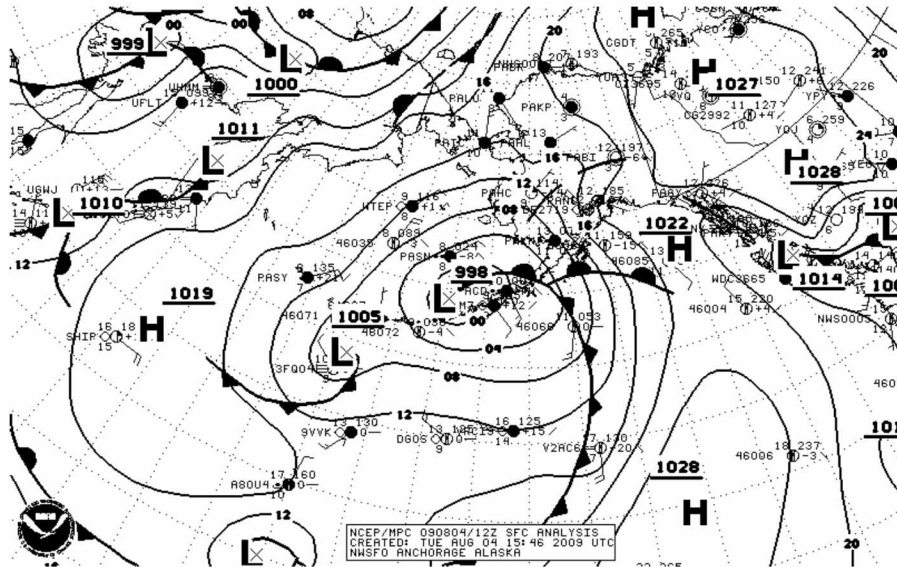
Figure 3.2 Synoptic surface map over Alaska for 4 August 12 UTC. Note that the low-pressure system over the Central Aleutian Islands brought moisture up to the Brooks Range area, while the Interior remained warm with low dewpoint temperatures. From: NWS, 2014
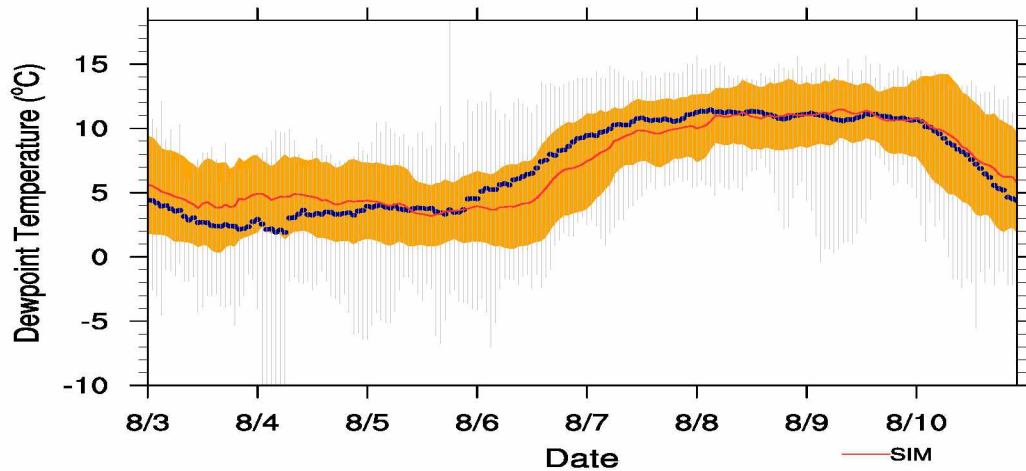
Figure 3.3 Spatial average hourly dewpoint temperature for the 33 sites during the study period. Blue dots represent the spatial average of the observed 2 m dewpoint temperatures. The red line is the spatial average of 2 m dewpoint temperatures as obtained from the WRF/Chem data. The grey lines are the mean standard deviation from the observed mean value over all sites. The orange shading is the mean spatial standard deviation of the simulated dewpoint temperatures over all sites.

3.1.3 Wind Speed

The model acceptably predicted the temporal evolution of 10 m wind speeds, with a positive bias of 0.1 m/s, a RMSE of 6.2 m/s, a SDE of 6.2 m/s and a correlation of 0.1. This low correlation is due to the fact that thunderstorms and fires strongly affect the local wind fields. Furthermore, channeling effects are of subgrid-scale with respect to the model, but are inherent in the observations. It is well known that all mesoscale models have difficulties to capture the wind speeds under stagnant conditions (Zhang et al., 2009) which characterized at least half of the episode. Slight offsets in the timing of frontal passages also lead to low performance skill scores with respect to wind speed (Mölders, 2008).

The overestimation of wind speed found in this study is consistent with other polar WRF studies (Hines and Bromwich, 2008; Grell et al., 2011; Hines et al., 2011). This overestimation also occurs in non-Polar Regions that

46

frequently have low wind speeds (Sauter and Henmi, 2004; Cheng and Steenburgh 2005).

These errors could be created due to the complex terrain within the domain, which includes three mountain ranges that are latitudinally oriented (Alaska Range, White Mountains, and Brooks Range). With these great changes in topography (Figure 2.3), it is difficult for any air quality and weather prediction model to account for mountain/valley circulations as well as wind channeling especially when the grid size is larger than the length scale these effects. Also, as pointed out above, WRF/Chem uses grid-area averaged terrain heights within each grid cell and as a result smooths the surface. With this smoothed surface, air is able to move at higher velocities than in nature.

It is also important to note that the model output is a volume average for an entire 4 km × 4 km × height of grid cell, whereas the surface observation is for a point location. This point location may have higher or lower wind speeds than the volume average of the grid cell.
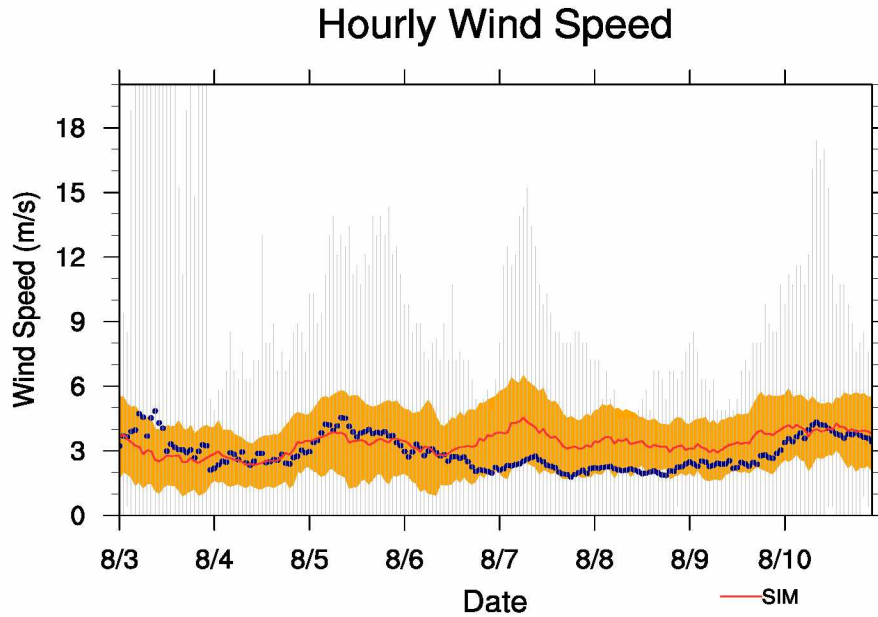
Figure 3.4 Spatial average of hourly 10 m wind speed for 3 to 10 August 2009. Blue dots are the spatial average of the observed wind speed; the red line is the spatial average of simulated wind speed for the 33 sites. The grey lines represent the mean standard deviation from the observed mean value over all sites. The orange shading is the mean spatial standard deviation of simulated wind speed over all sites.

3.1.4 Wind Direction

Winds in Interior Alaska are relatively light (Shulski and Wendler, 2007). With these light winds, the direction can be extremely variable, as can be seen in Figure 3.4. Although the correlation is 0.4, the model captures the changes in spatial average hourly 10 m wind direction broadly (Table 3.1), especially with a domain of this size where wind direction can be completely different when the sites are far away from each other and network density is sparse (Eidsvik et al., 2004) (Figure 3.5). The RMSE and SDE were 115° and 111° respectively, with a mean direction being 166° and a bias of 15°.

Like the 10 m wind speeds, 10 m wind directions are measured at a single point, while the model predicts a volume average value for an entire grid cell. As a result, errors occur. Small scale circulations and channeling

48

effects are of subgrid-scale with the grid increment of 4 km, but are inherent in the point measurements.
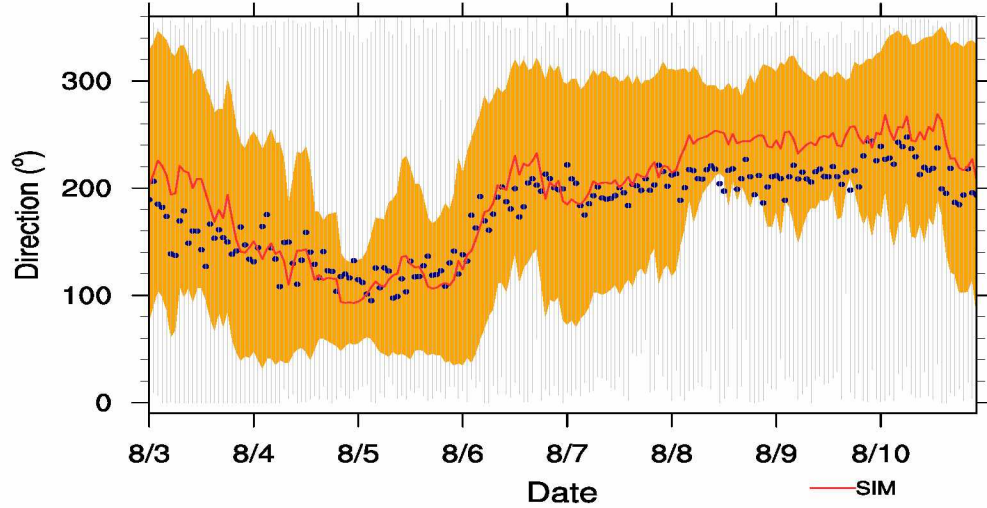
Figure 3.5 Spatial average of hourly 10 m wind direction for 3 to 10 August 2009. Blue dots are the spatial average of the observed wind direction; the red line is the spatial average of simulated wind direction for the 33 sites. The grey lines represent the mean standard deviation from the observed mean value over all sites. The orange shading is the mean spatial standard deviation of simulated wind direction over all sites.

3.2 Particulate Matter Evaluation at Fairbanks

Data of observed PM$_{2.5}$ concentrations are available at the State Office Building in downtown Fairbanks. This data is used to evaluate particulate matter of 2.5 μm or less in diameter predicted by the WRF/Chem. Simulated PM$_{2.5}$ was extracted from the output at the same latitude/longitude, time and height as the station in downtown Fairbanks for all days during the episode.

Over time, the model showed a fractional bias of -10% and a NME of 20%. It is important to remember that the observed data is for a specific point whereas the model data is valid for an entire grid cell. Similar results between modeled and observed particulate matter were also noted in Solazzo et al. (2012), Mölders et al. (2012), and Madden (2014).

49

Particulate matter concentrations can be extremely localized as they depend on transport from wind, chemical and physical processes, as well as having distinct sedimentation velocities (Seinfeld and Pandis, 2006). Figure 3.6 shows that for most days the simulated and observed concentrations show a similar temporal trend, but differ notably in magnitude.
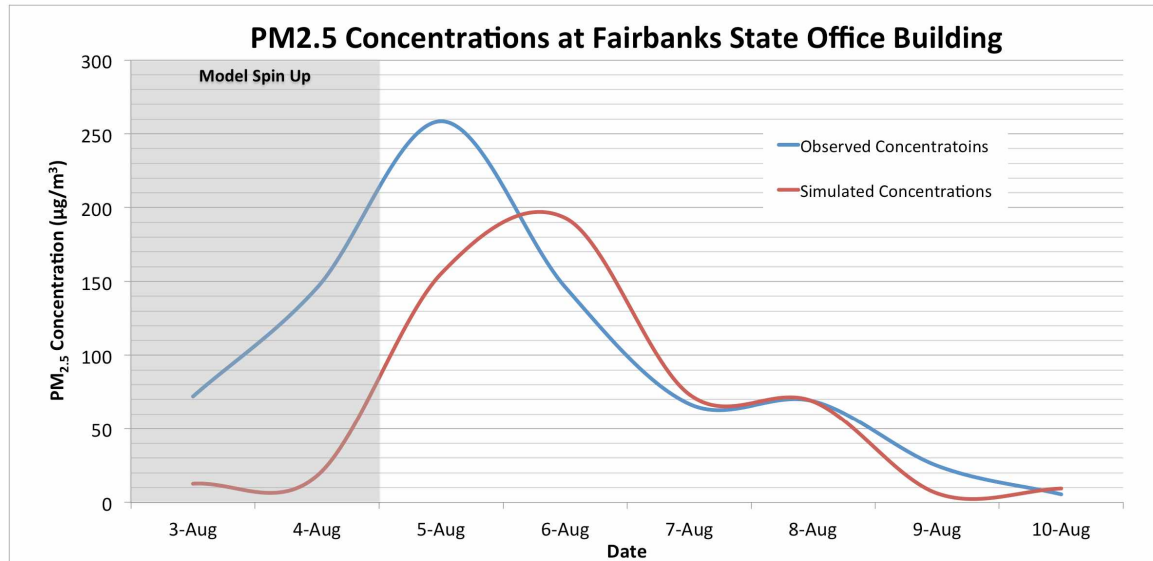
Figure 3.6 PM$_{2.5}$ observed at the State Office Building and WRF/Chem output PM$_{2.5}$ concentrations as simulated data (red) and observed data (blue) at the State Office Building in downtown Fairbanks. The grey shaded region is 5 August which is still during the model's spin up.

3.3 CALIPSO 1B Products and WRF/Chem Evaluation

While all CALIPSO passages were analyzed, for the sake of space only two data sets of CALIPSO 1B and WRF/Chem cross sections will be presented: 4 August at 22:33 UTC, and 5 August at 05:11 UTC. These dates were chosen as all other days had too many clouds for CALIPSO to reach the lower atmosphere, therefore, this comparison would only demonstrate WRF/Chem's performance in predicting clouds and the aerosols above the clouds. Furthermore, on the chosen days, the path of CALIPSO went over the plumes from the Crazy Mt. Complex fires. CALIPSO does not pass at the beginning of every hour so the closet hour of WRF/Chem data is used for comparison. Doing so, creates little temporal time differences.

50

Due to the synoptic conditions, during much of the episode, Interior Alaska was cloud covered or at least had mostly cloudy skies. Thus, it is difficult to find imagery where the smoke plume is visible from space. Therefore, METAR reports as well as discussions from the National Weather Service were used for further evaluation of the presence of smoke.

Analysis of CALIPSO data with WRF/Chem output for all days during the study shows an accurate prediction of particulate matter near the surface, and its ability to advect particulate matter upward within the ABL.

3.3.1 4 August Case

MODIS imagery from 4 August at 00:10 UTC can be seen in Figure 3.7a. Just south of the Brooks Range there is clear evidence of wildfire smoke that was transported northwestward. CALIPSO traveled over this area, going over the central part of the model domain towards the southwest (Figure 3.7) bringing the sensor over this plume that was seen in this MODIS imagery taken by the Aqua satellite.

In the attenuated depolarization ratio, CALIPSO picks up some high-level cirrus clouds around 10 km between 64.26°N and 65.39°N. However, CALIPSO was still able to pick up particulate matter close to the surface beneath this cloud layer with depolarization ratios of approximately 0.05 km^{-1}sr^{-1} (Figure 3.8). WRF/Chem also modeled the particulate matter in this area (Figure 3.9) These particulates only went up to about 1000 m in altitude, which is consistent with wildfire emissions because most particulates are contained within the ABL (Gupta et al., 2006). At the northern edge of the path, there were low cloud layers that prevented the lidar signal from reaching the ground, thus making it impossible to investigate particulate matter near the surface.
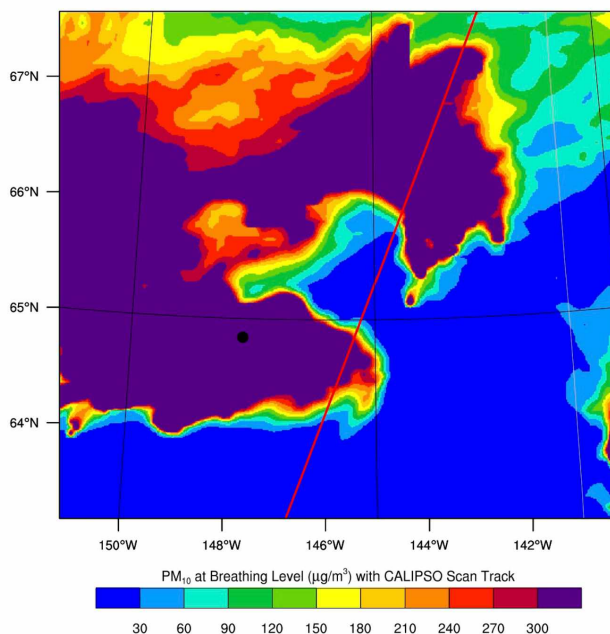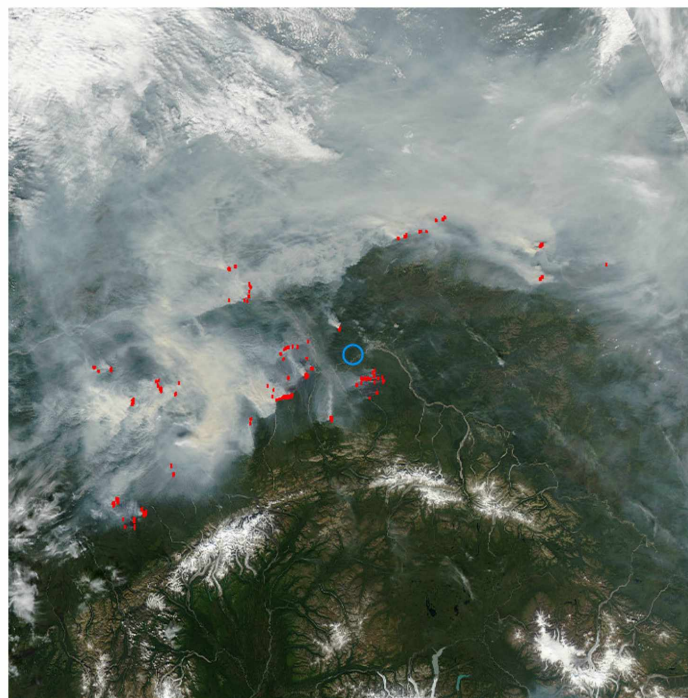
Figure 3.7 4 August MODIS imagery with WRF/Chem PM$_{10}$ at breathing level Top) MODIS imagery over Alaska taken by Aqua, 4 August 00:10 UTC. Wildfire smoke can be seen throughout the WRF/Chem model domain. The blue circle is the AERONET site at Bonanza Creek (30 km southwest of Fairbanks, AK), the red points are fire locations. Bottom) PM$_{10}$ in μg/m^3, the CALIPSO track is marked in a red line. CALIPSO passed over at **22:33** UTC. The black dot represents Fairbanks.

52

532 nm Total Attenuated Backscatter

UTC: 2009-08-03 22:32:49 to 2009-08-03 22:33:59   km^{-1} sr^{-1}

Attenuated Depolarization Ratio

UTC: 2009-08-03 22:32:49 to 2009-08-03 22:33:59   km^{-1} sr^{-1}
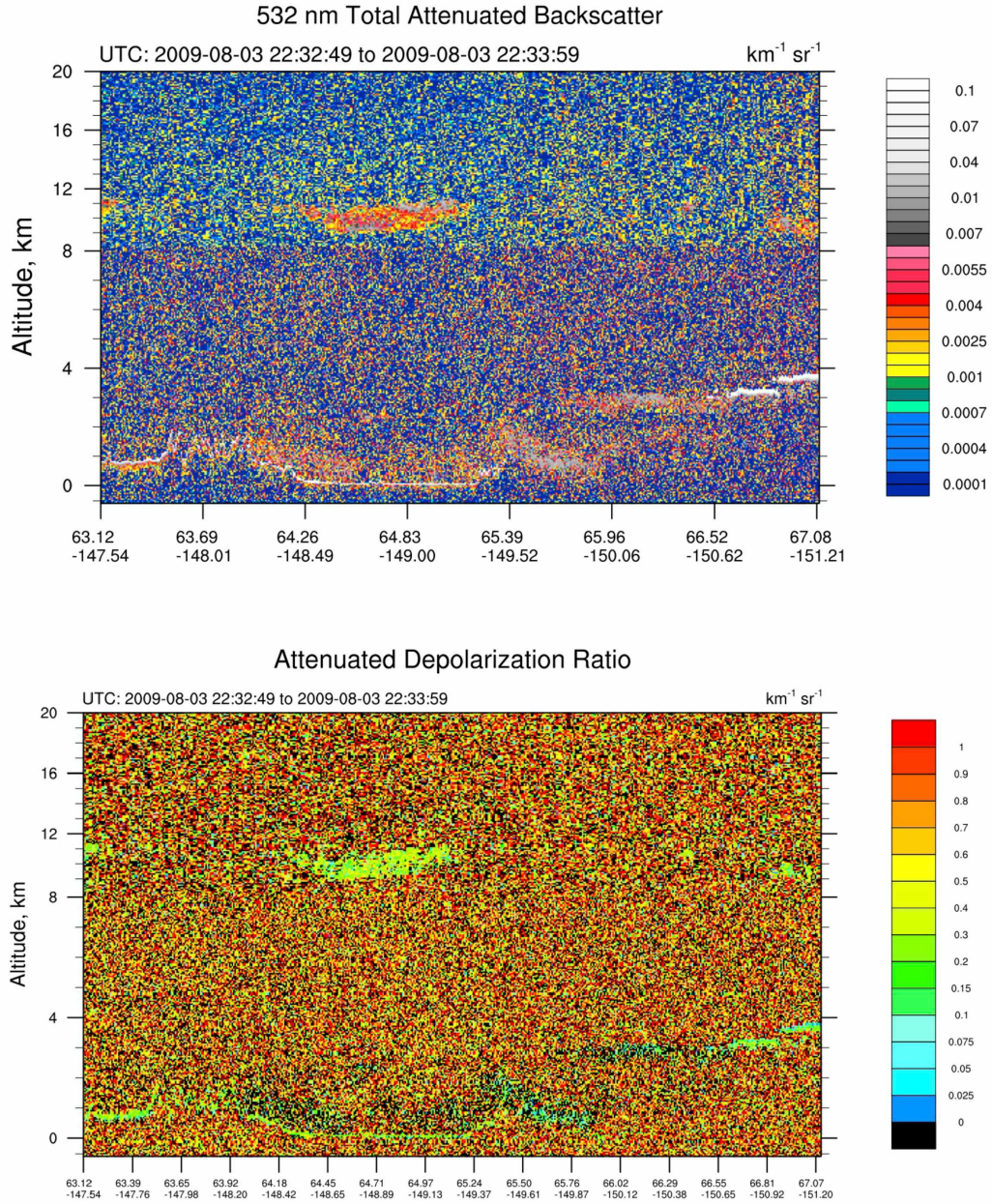
Figure 3.8 4 August attenuated backscatter and depolarization. Top) Total attenuated backscatter for the CALIPSO path on 3 August 2009 at 22:33 UTC. Note the increase in backscatter from the surface up to 2 km. Bottom) Attenuated depolarization ratio along the CALIPSO path on 3 August 2009 at 22:33 UTC. Increase in depolarization at the surface up to 2 km is seen.
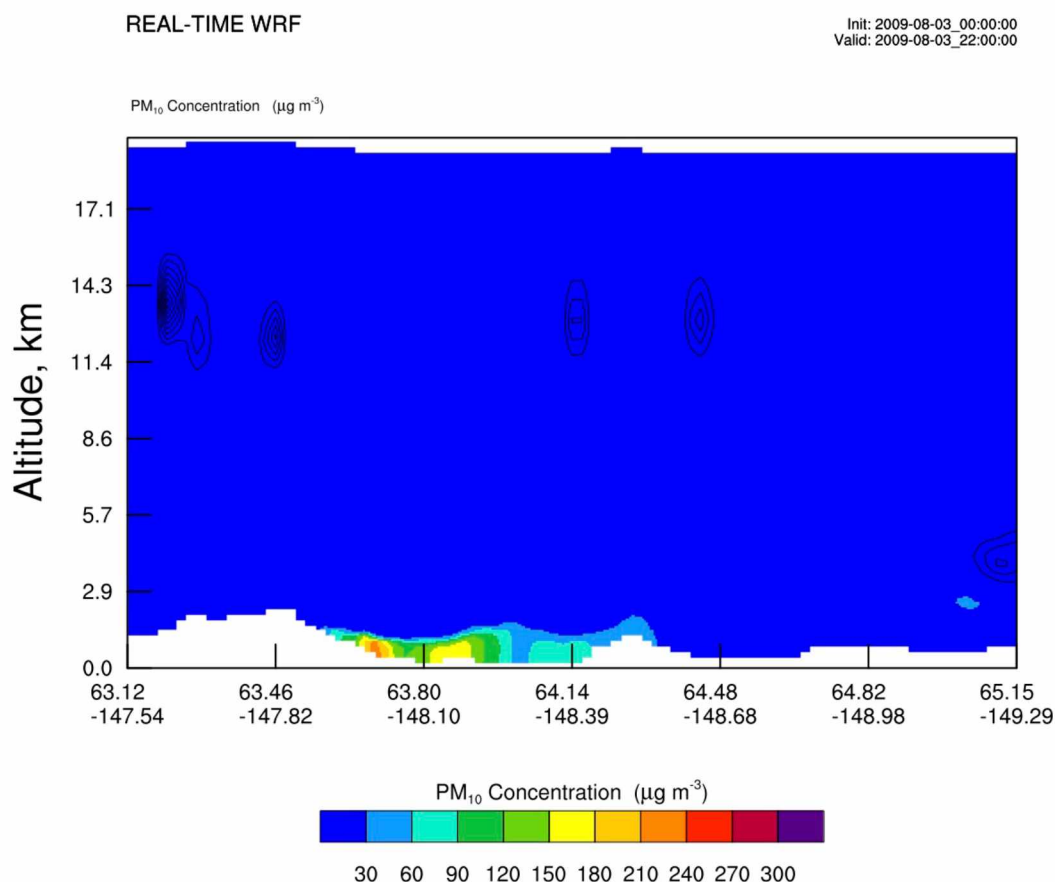
Figure 3.9 WRF/Chem cross section along the CALIPSO path on 3 August 2009 at 22:33 UTC. Mixing ratio is also plotted to show that the increase in backscatter and depolarization that was seen in Figure 3.8 are not clouds.

3.3.2 5 August Case

On 5 August the MODIS imagery showed a similar situation as on 4 August. A distinct smoke plume existed just south of the Brooks Range with clouds from a low-pressure system approaching from the southwest (Figure 3.10). On this day, the CALIPSO path was the closest to the Crazy Mt. Complex Fires compared to all other days during the episode. Depolarization ratios of 0 to 0.075 km^{-1}sr^{-1} located near the surface and extending upward to 3 km height are signs of thick plumes made of particulate matter (Figure

3.11) between 68°N and 66°N. These signatures likely stemmed from particulates being emitted high into the atmosphere through strong updrafts.

Upward transport can be seen in the WRF/Chem cross section that follows the panel of the CALIPSO path (Figure 3.12). The total mixing ratio is also plotted on this cross section to show that CALIPSO detected was particulate matter rather than low-level clouds. The upward transport is less in WRF/Chem as the model does not consider the release of heat from the fire.
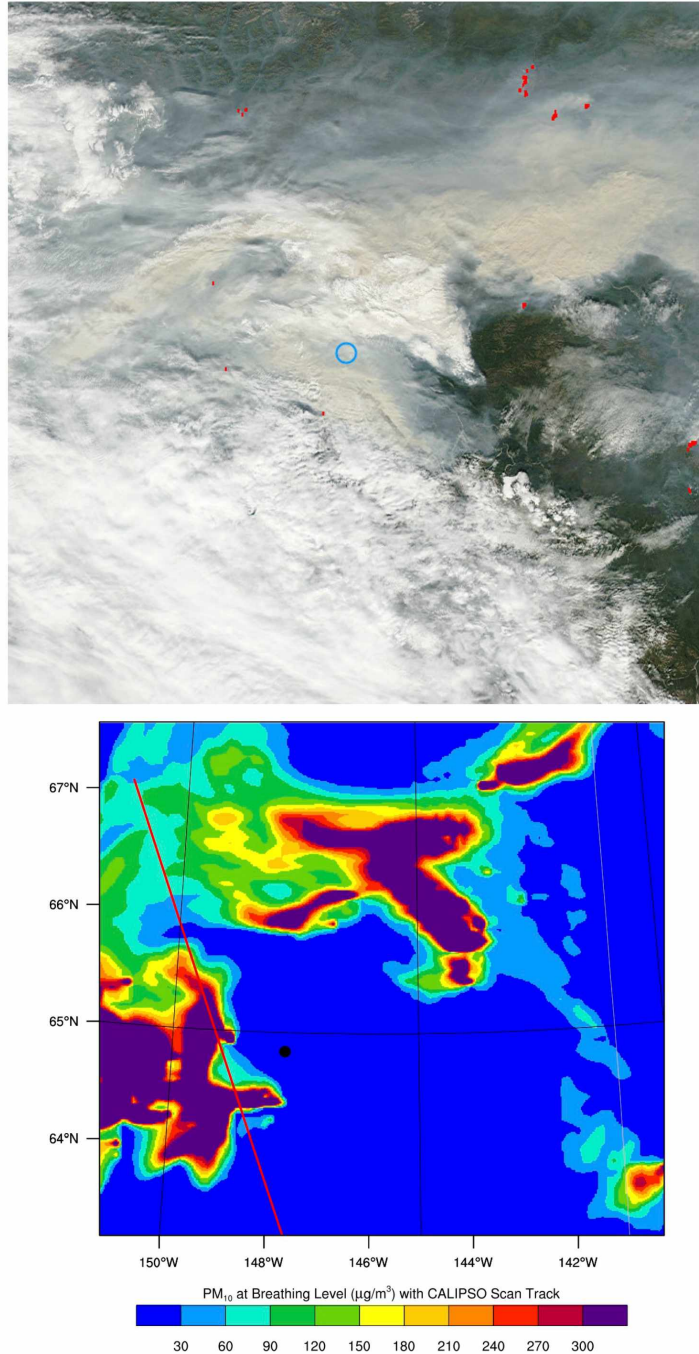
Figure 3.10 5 August MODIS imagery with WRF/Chem PM$_{10}$ at breathing level Top) MODIS imagery over Alaska taken by Aqua, 5 August. Wildfire smoke can be seen throughout the WRF/Chem model domain. The blue circle is the AERONET site at Bonanza Creek (30 km southwest of Fairbanks, AK), The red points are fire locations. Bottom) PM$_{10}$ in μg/m^3, the CALIPSO track is marked in a red line. CALIPSO passed over at 12:01 UTC. The black dot represents Fairbanks.
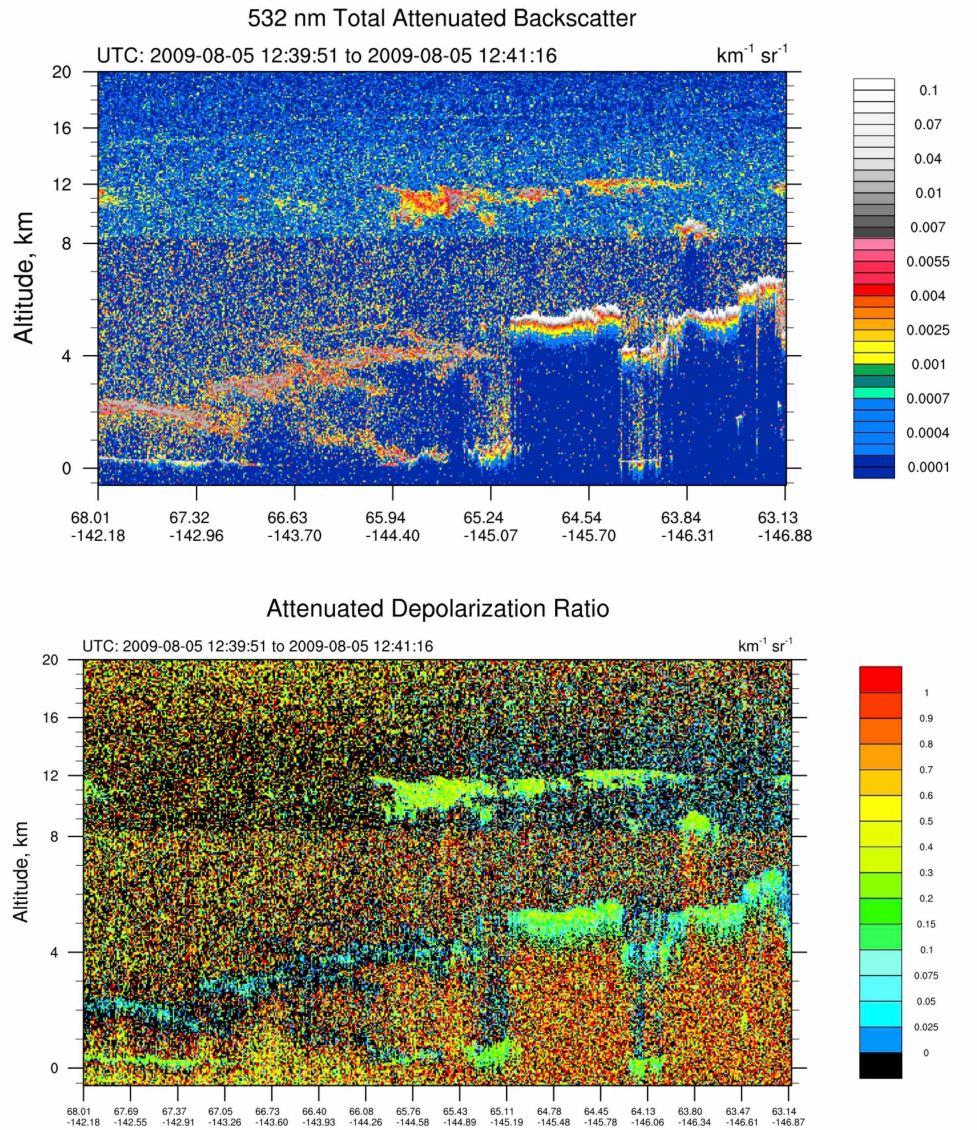
Figure 3.11 5 August attenuated backscatter and depolarization Top) Total attenuated backscatter for the CALIPSO path on 5 August 2009 at 12:01 UTC. Note the increase in backscatter from the surface up to 2 km. Bottom) Attenuated depolarization ratio along the CALIPSO path on 5 August 2009 at 12:01 UTC. Increase in depolarization at the surface up to 2 km is seen. Both images show particulate matter extending from the surface upward.
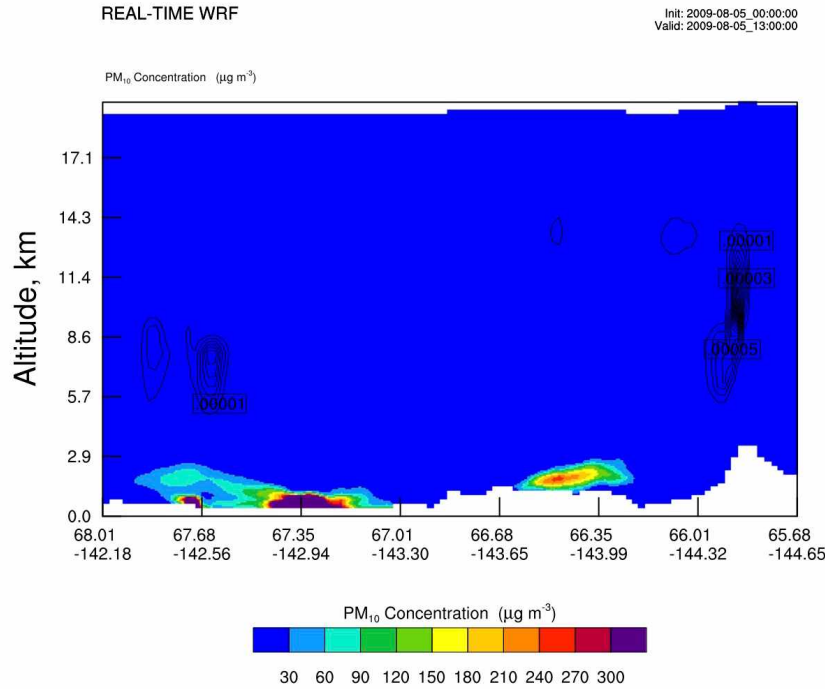
Figure 3.12 WRF/Chem cross section along the CALIPSO path on 5 August 2009 at 12:01 UTC. Mixing ratio is also plotted to show that the increase in backscatter and depolarization that was seen in Figure 3.11 are not clouds, the same signature of particulate matter extending from surface upward is also seen.

3.4 Conclusions from Model Evaluation

The comparison of simulated data to surface observations indicated that for meteorological quantities WRF/Chem produced acceptable results for use in this thesis. The largest errors were found with the 10 m wind speed and direction, but because of the relatively light winds throughout the model domain (excluding channeling effects) these errors are within the range of errors of current state-of-the-art models (cf. Hacker and Rife, 2007; Das et al., 2008).

The model results showed high temperature bias (2.7°C), but simulated 2 m temperature was well correlated with the observed 2 m temperature data (0.7).

Simulated and observed $PM_{2.5}$ concentrations broadly agreed with respect to the temporal trends, but notably differed in magnitude during portions of the study period. The average percent difference between the simulated and observed $PM_{2.5}$ is 42%. The difference in magnitude may be due to the offset in the wind direction and/or the overestimation of wind speed. To have a better idea it would be useful to have more sites recording $PM_{2.5}$, but the only other site within the model domain is missing data for this episode.

Based on the qualitative comparison with the CALIPSO lidar curtains, the model acceptably depicted locations of particulate matter close to the surface. But due to the cloudiness during the episode, the LIDAR was not able to reach the lower atmosphere for more than two days due to signal attenuation by clouds.

With regards to the presence of PM above cloud tops WRF/Chem had near steady state concentrations throughout the domain. This homogeneous concentration distribution was not the case according to CALIPSO. This discrepancy may be due to the coarse resolution of WRF/Chem in the upper troposphere. Note that the focal point of interests was in the ABL. WRF/Chem also did not produce most of the cirrus that were present, as well as the full vertical extent of cumulus.

Chapter 4

Results

This chapter discusses the measurements of temperature, dewpoint temperature, and concentrations of gaseous and particulate matter (PM) the ScanEagle would have been able to take if it had flown with respective sensors through the wildfire smoke plumes during the Crazy Mountain Complex Fires.

The sampling domain for the UAV is restricted to 60 km × 60 km as this corresponds to the area the ScanEagle can cover with a maximum of 20 hours of flight duration. As pointed out in Section 2.5, the examination of the WRF/Chem data revealed that wind speeds and wind directions were not a factor in sending the UAV off its path out of a grid cell when performing the sampling. During the Crazy Mountain fire, wind speeds were not strong enough to move the ScanEagle out of a 4 km × 4 km grid cell.

The WRF/Chem 20-hour average of each sampled variable is used as the "true value" that the mean values determined from the sampling along the various sampling patterns are compared to. This "true value" is also referred to as 'grand truth'. Recall that the 20 hour averaging is done based on the maximum flight time for the UAV while traveling at its cruising speed with payload.

The height above ground level (AGL) that the UAV should fly during this theoretical experiment was determined. It is important to understand that any ascent of the ScanEagle consumes fuel. This means that actually less time is available to sample at high than low altitudes AGL. Therefore, it was examined how the obtained mean distributions differ from each other when based on sampling at three different heights.

It was also determined whether the direction of travel and speed of the UAV would be a factor in the resulting temporal mean spatial distribution. Details of these experiments were discussed in Section 2.5.

4.1 Meteorology

4.1.1 Mean Temperature Distributions

The average temperature was calculated for each for WRF/Chem grid cell over a 20 hour period within the UAV sampling domain for each day from 3-10 August 2009 (e.g., Figure 4.1d). This spatial distribution of 20 hour mean temperatures is assumed as the 'grand truth' that the UAV sampling should ideally reproduce/provide when the sampled values are interpolated in space and averaged in time where the UAV took more than one measurement in its 20 hour flight.

When examining the WRF/Chem 20 hour mean temperature distributions, the largest differences with height are in regards to times of temperature maximums. The largest difference between the maximum temperature at 200 m and the maximum difference at 1000 m is consistently 8°C for all days examined. This value corresponds coarsely to the dry adiabatic temperature gradient of 0.98°C/100m, with a value of of 8°C/800m The minimum differences in temperature concerning height occur alongside the minimum temperatures with differences ranging between 2 and 5°C. Given that temperature typically decreases with height (except under inversion conditions), temperature differences are expected to occur between samples taken at different heights. Thus, the result shows no need for a repetitive discussion of individual heights. Therefore, only the 200 m height will be discussed in detail for all UAV samplings with respect to temperature.

4.1.1.1 Sampling Height

In the following discussion, 6 August will be the focus of the main findings of the temperature analysis because of the greatest variation between the halves of flight path, and as a result the largest biases. This means the worse case scenario is discussed.

The greatest differences between mean temperatures occurring on 6 August during the first and second halves of the sampling pattern was 11°C

(Figure 4.1a, c). This difference occurred on the northern edge of the sampling domain. The differences can be explained by the passage of a cold front at the time the UAV reached the northern edge of the sampling domain. During the second HOFP (Half Of Flight Path) when the UAV began to return to the starting point, temperatures over the whole UAV sampling domain had decreased by at least 2°C due to the front's progress. Due to the small time-lag between the reoccurring UAV overpasses, the differences were smaller between overpasses around the northeast corner than between data sampled during the first and second HOFP in the southwestern corner, for instance.

When compared to the 20 hour average of the 'grand truth', there was a 15% positive bias (sampled vs. 'grand truth') for the first HOFP for both the normalized mean biases (NMB) and fractional mean biases (FB). However, after the passing of the cold front in the second HOFP, there was a significant negative bias (p-value < 0.0001) with the NMB being -34% and where the FB was -28% when compared to the 20 hour average of the 'grand truth'.
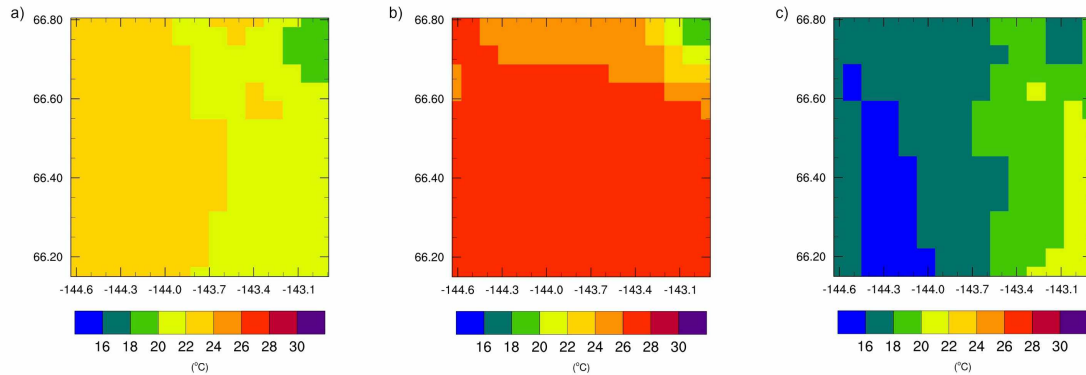
Figure 4.1 Mean spatial temperature distribution for 6 August 2009 a) Average temperature over the UAV sampling domain from 01-20 UTC 'grand truth' b) Temperatures sampled along the first HOFP and c) second HOFP.

Overall, when compared to the 'grand truth' the first HOFP mainly contributed to the positive bias. Despite the slightly higher bias than with the second HOFP, the correlation of temperature sampled on the first HOFP with

63

the 20 hour mean was better with a value of 0.7 than those of the second HOFP with the 20 hour mean (Table 4.1). Due to the front moving in, the UAV sampled in colder air than on the first HOFP leading to lower temperatures when compared to the 20 hour average creating a negative bias of -0.2°C. When compared to the 'grand truth' both halves of flight paths together create an accurate picture of the environment.

Table 4.1 Means and standard deviations, and skill scores of temperature three sampling heights as determined over the entire episode and sampling techniques. Sampling pattern 1 was used as the default pattern.

Flight Height	Grand Truth	Sampled	RMSE	SDE	Bias	Correlation
200 m (°C)	20.0±2.6	19.1±4.2	3.2	1.7	-0.1	0.3
500 m (°C)	19.9±2.7	18.1±4.7	1.1	1.2	~0	0.7
1000 m (°C)	13.9±2.5	14.3±3.1	0.6	0.8	~0	0.8

When averaged over the entire study period there are near isothermal conditions between the 200 and 500 m heights. On a day-to-day basis this signature was not there. Although temperatures were similar between the two layers they did not exhibit isothermal conditions. Higher RMSE, SDE, bias and lower correlation at the lowest levels is most likely due to the strong impact from surface conditions.

4.1.1.2 Sampling Pattern

As demonstrated by the 200 m discussion in the previous section, the following general behavior was found. Changing the direction of the flight path did not affect the 20 hour mean spatial distributions of temperatures for days that did not have a changing synoptic pattern as was seen on 6 August. However, under changing synoptic conditions, the mean differences between the first and second, as well as the first and third sampling patterns were

64

less than 2°C in magnitude in both cases. For each day, maximum differences between mean spatial temperature distributions ranged between 3 and 7°C. The largest differences were located near the edges of the UAV sampling domain. The differences were occurring due to the diurnal cycle. Values near the center of the UAV sampling domain had the smallest differences among different sampling patterns because the UAV passed over this area at roughly the same time, no matter which of the three sampling pattern was used when compared to the 20 hour average 'grand truth'.

The sampling on 6 August produced the largest differences in temperatures with regard to the chosen sampling pattern due to the passing of the cold front. The largest differences occurred between the first and third sampling pattern. This finding is expected as these sampling patterns are completely reversed from each other (Figure 2.5). Consequently, the sampling was detecting the presence of the cold front at different times and different locations. In Figure 4.2, the average sampled temperature for all sampling patterns is shown on the left column with the difference between the average sampled temperature and the 'grand truth' on the right.

Average sampled values were similar for the first and third sampling patterns that only differed with respect to the starting location. Thus, the areas of small and large differences appear to be rotated. The second sampling pattern provided a wider variation in average sampled temperature than the first and third sampling patterns. As a result, the difference between average sampled temperature and 'grand truth' is greater than that was found for the first and third sampling pattern. Thus, one may conclude that it is needed to consider the synoptic situation (passage of pressure systems and fronts) and the purpose of the sampling prior to deciding on a particular sampling pattern.
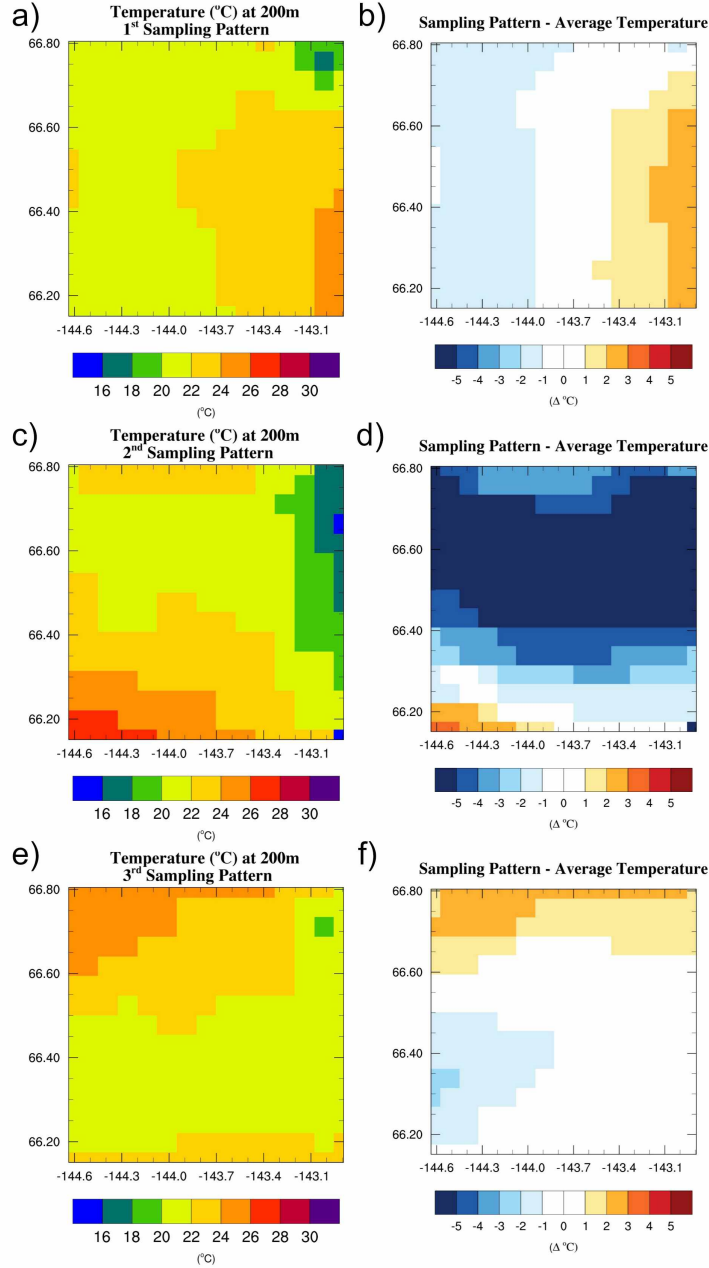
Figure 4.2 6 August comparison of 20 hour sampled mean temperatures from sampling a) c) e) and differences from the 20 hour mean temperatures from sampling and the 20 hour 'grand truth' b) d) f) for 6 August 2009 as obtained for the first sampling pattern a) b), the second sampling pattern c) d), and the third sampling pattern e) f). Note the 20 hour 'grand truth' can be seen in Figure 4.1a.

Due to the diurnal cycle, the UAV continually recorded lower temperatures on the second HOFP than the first HOFP for each sampling pattern. The RMSEs for all sampling patterns were similar, as were the SDEs. Biases varied in sign, but were of similar magnitudes (Table 4.2). Variations in biases were the result of the timing of the sampling and the diurnal cycle.

Based on these findings, it can be said that the mean distribution of sampled temperature is not affected by the sampling patterns except under changing synoptic conditions.

Table 4.2 Mean and standard deviations, and skill scores of temperature for the various sampling patterns at the 200 m, 500 m, and 1000 m height determined over the entire episode and UAV sampling domain.

Sampling Pattern	Grand Truth	Sampled	RMSE	SDE	Bias	Correlation
200 m						
1st (°C)	20.0±2.6	20.0±4.2	3.2	1.7	-0.1	0.3
2nd (°C)	20.0±2.6	22.9±4.1	3.3	1.9	-0.1	0.7
3rd (°C)	20.0± 2.6	20.0±3.8	3.5	1.6	-0.2	~0
500 m						
1st (°C)	19.9±2.7	18.1±4.7	1.1	1.2	~0	0.7
2nd (°C)	19.9±2.7	17.7±3.4	0.6	0.8	~0	0.6
3rd (°C)	19.9±2.7	17.8±3.9	0.8	1.1	~0	0.7
1000 m						
1st (°C)	13.9±2.5	14.3±3.1	0.6	0.8	~0	0.8
2nd (°C)	13.9±2.5	13.9±2.0	0.7	0.7	~0	0.8
3rd (°C)	13.9±2.5	13.9±1.8	0.7	0.8	~0	0.9

Other than at the 200 m height the third sampling pattern has the highest correlations to temperature. The reason for the correlation being approximately zero for the third sampling pattern at the 200 m height is due

to the cold front. Because the third sampling pattern starts in the northeast corner all sampling is done post cold front on 6 August, and as a result the correlation is lowered. This signature is not evident at the other heights because of the slope of the front; lower altitudes are subjected to colder air before upper altitudes. This can also be seen in the biases as the 200 m height is the only height that has a bias that is nonzero regardless of sampling direction.

4.1.1.3 Sampling Speed

When UAV flight speed is reduced, and hence sampling speed, the presence of diurnal temperature cycles was much more evident than with the change in sampling pattern or height. The reduced speed resulted in a more prevalent visibility of the diurnal cycle for all days during this investigation. With a reduced flight speed, the drop in temperatures can be seen prominently as the UAV progressed to the northeast during the first HOFP. The northward decrease of temperatures does not occur in this magnitude when sampling with normal cruising speed or at maximum speed (Figure 4.3). The only exception is the passing of the aforementioned cold front on 6 August. It is important to note that when the speed of the UAV was reduced the artificial sampling took longer than 20 hours, but is still compared to the 20 hour mean or the 'grand truth'. For a uniform analysis the last eight hours of the flight were not considered in the comparison to the 20 hour 'grand truth'.

The reduced speed is also responsible for the increase of temperatures found when examining the samples taken during the last 4 hours of the sampling period that occur on the following day. The sampling showed an increased temperature as compared to the sampling collected at cruising speed to be seen in the second HOFP. This warm up was not seen anywhere else because other experiments lasted 20 hours or less.

When the UAV travelled at maximum speed, the distributions obtained from sampling were typically closer to the WRF/Chem 20 hour average values, with the exception being 6 August when the cold front passed through (Table 4.3). On this day, the temperature distribution obtained by UAV-sampling overestimated the 20 hour mean temperatures by a maximum of 5°C for all three sampling speeds tested. The sampling at maximum speed captured very little of the passage of the cold front because the ScanEagle was always travelling ahead of the front's southward progression.

Table 4.3 Means and standard deviations, and skill scores of temperature for the various sampling speeds at the 200 m, 500 m and 1000 m height determined over the entire episode and sampling pattern 1 and cruising speed were the default settings.

Sampling Speed	Grand Truth	Sampled	RMSE	SDE	Bias	Correlation
200 m						
Maximum (°C)	20.0±2.6	22.6±6.0	2.9	1.5	0.1	0.3
Cruising (°C)	20.0±2.6	22.9±5.2	3.3	1.9	0.1	0.7
Minimum (°C)	20.0±2.6	21.7±6.8	3.5	4.0	~0	0.6
500 m						
Maximum (°C)	19.9±2.7	18.4±4.7	1.2	1.1	~0	0.9
Cruising (°C)	19.9±2.7	18.1±4.7	1.1	1.2	~0	0.7
Minimum (°C)	19.9±2.7	17.9±3.9	1.2	1.5	~0	0.7
1000 m						
Maximum (°C)	13.9±2.5	14.2±2.9	0.9	1.0	~0	0.8
Cruising (°C)	13.9±2.5	14.3±3.1	0.6	0.8	~0	0.8
Minimum (°C)	13.9±2.5	13.9±3.0	0.6	1.1	~0	0.8
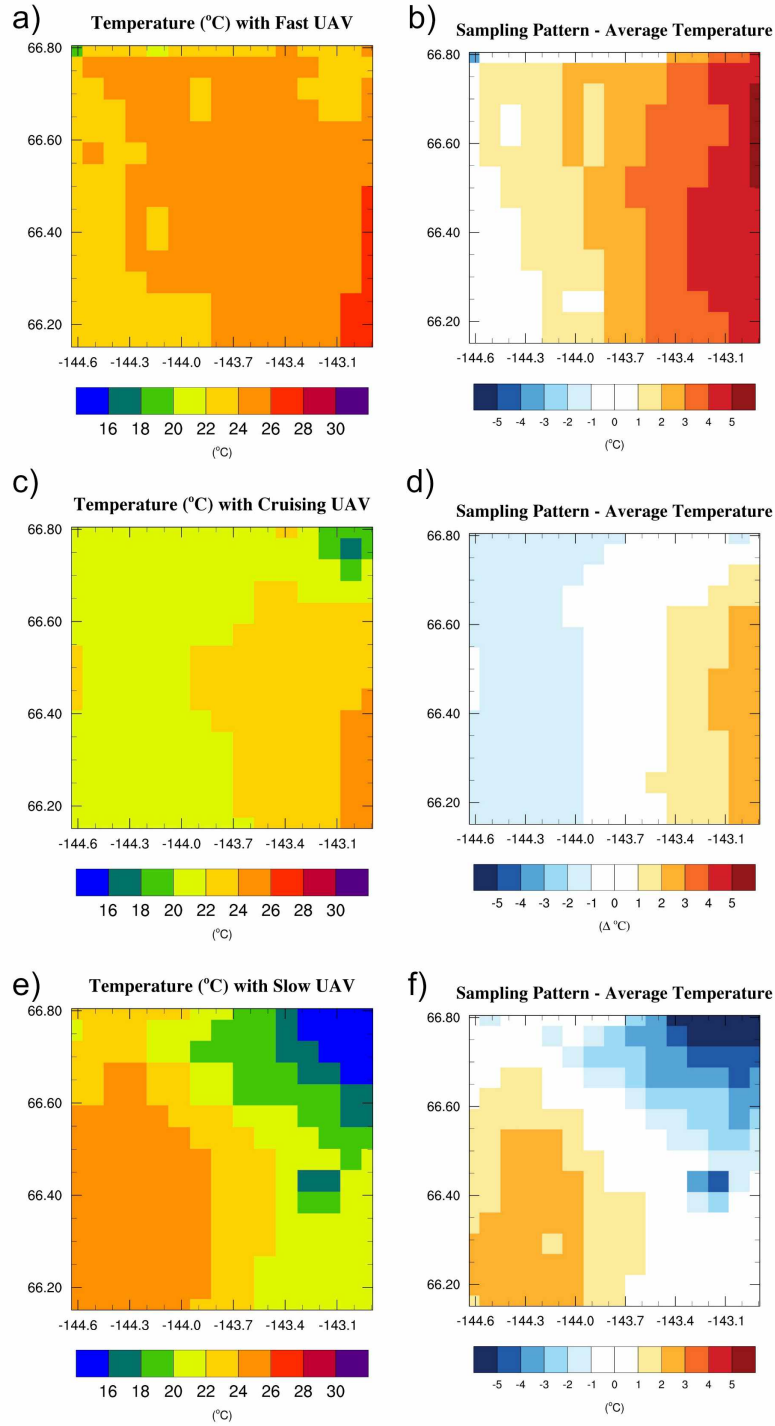
Figure 4.3 6 August sampled temperature data with UAV travelling at its maximum, cruising, and minimum speed (a), c), e) respectively). The difference between the sampled temperatures and the 20 hour average 'grand truth' is shown in b), d), f). The 20 hour average 'grand truth' is shown in Figure 4.1a

When the UAV travelled at its maximum speed, the 20 hour means derived from sampling were correlated the lowest with the lowest with the 20 hour mean of the 'grand truth' values. This fact is the result of the entire diurnal cycle not being captured because the flight did not sample 20 hours worth of data but s compared to the 20 hour 'grand truth'. This comparison is done to keep a consistent comparison between what the UAV sampled and what is considered to be the 'grand truth'.

Although the correlation for when the UAV travelled at its minimum speed was close to the correlation obtained when the UAV flew at cruising speed, the errors were larger for the minimum speed. These larger errors could be due to the fact that the flight time exceeds 24 hours. Consequently, the UAV samples more than one diurnal cycle. The lack of bias for when the UAV travelled at its slowest speed is most likely an artifact due to sampling for more than 20 hours. Therefore, biases due to warmer or cooler portions of the day cancel out when determining a 20 hour average. The highest correlation (0.9) for the entire period was with the maximum sampling speed and at the 500 m height. Based off of this finding it would suggest that the maximum sampling speed should be used for the best accuracy in temperature sampling. But with the correlation of 0.3 at the 200 m height this cannot be concluded. The correlations at the 1000 m height were equal for all sampling speeds.

4.1.2 Dewpoint temperature

Similar to temperature, there are also differences in dewpoint temperature with respect to height because dewpoint temperature decreases at a rate of 0.172 K / 100 m. The greatest differences between dewpoint temperature distributions at different heights coincide with the minimum dewpoint temperature over the whole UAV sampling domain. During most days, this difference was between 1°C and 2°C, with the extreme being 3.3°C

72

on 5 August. This larger difference was due to the approaching low-pressure system.

With these otherwise small differences in dewpoint temperatures over a difference of 800 m, it is again reasonable to conclude that the UAV travelling at the 200 m height is a good representation of the conditions up to 1000 m (Figure 4.4).
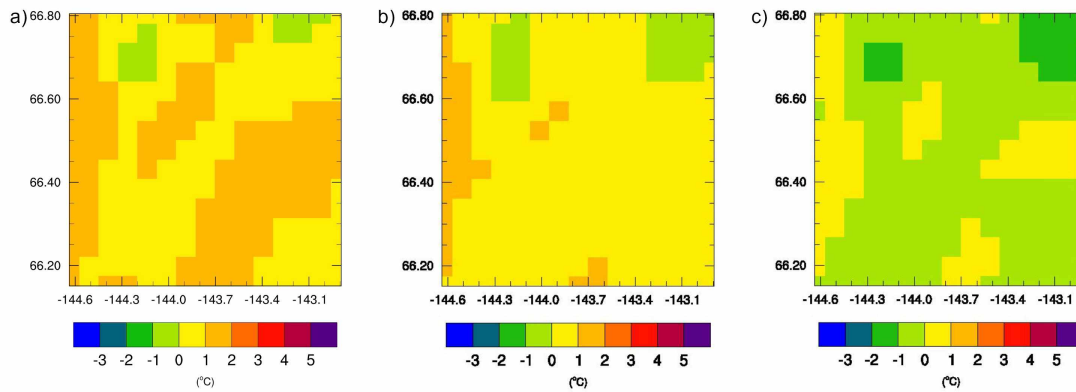
Figure 4.4 20 hour average of the 'grand truth' for dewpoint temperatures on 6 August 2009 at the a) 200 m, b) 500 m, and c) 1000 m heights.

4.1.2.1 Sampling Height

Examining the HOFPs for all days shows little to no differences between the first and second HOFP at same sampling height, indicating that there are no large fluctuations in space on a day-to-day basis. During the sampling period and at same sampling height there was a maximum dewpoint temperature difference of 1°C in a few of the grid cells (less than five per sampling path) within the UAV sampling domain.

Despite temperature having the greatest spatial and temporal variation during the sampling on 6 August, dewpoint temperature remained fairly constant with both the Normalized Mean Bias (NMB) and Fractional Bias (FB) being less than 1% in magnitude. This finding is an outstanding result given that the maximum difference between a HOFP and the 20 hour average is about positive 0°C, i.e. less than current measurement accuracy

73

for temperatures (Mölders, 2011). This means that a good understanding of the dewpoint temperature distribution can be achieved when sampling at the 200 m height when there are no changes in the synoptic conditions.

4.1.2.2 Sampling pattern

During the episode of this study, there were no large moisture fluxes during a particular day. As a result, there was not much change in dewpoint temperature on the diurnal scale. Consequently, changing the sampling pattern of the UAV had little to no effect on the 20 hour mean spatial distributions constructed from the sampled dewpoint temperatures (Table 4.4). Dewpoint temperatures did not change between sampling patterns causing the difference between the sampled dewpoint temperatures and the 20 hour 'grand truth' to be zero for all sampling patterns (Table 4.4).

With the sampling of dewpoint temperatures the pattern made no difference in results as RMSE were approximately zero for all sampling patterns at all heights. The correlations for all sampling patterns at all heights was 1.0, meaning that what was sampled matched the 20 hour 'grand truth' for all days during the study. Plots for dewpoint temperatures with the three sampling patterns are the same as 'grand truth' plots (for various heights) in Figure 4.4.

Table 4.4 Means and standard deviations, and skill scores of dewpoint temperatures for the various sampling patterns at 200 m, 500 m and 1000 m height determined over the entire episode and sampling. Note that the 1st sampling pattern is the default pattern of this study.

Sampling Pattern	Grand Truth	Sampled	RMSE	SDE	Bias	Correlation
200 m						
1st (°C)	1.0±0.3	1.0±1.0	~0	0.5	~0	1.0
2nd (°C)	1.0±0.3	1.0±1.0	~0	0.5	~0	1.0
3rd (°C)	1.0±0.3	1.0±1.0	~0	0.5	~0	1.0
500 m						
1st (°C)	0.5±1.5	0.5±1.5	~0	0.5	1.0	1.0
2nd (°C)	0.5±1.5	0.5±1.5	~0	0.5	1.0	1.0
3rd (°C)	0.5±1.5	0.5±1.5	~0	0.5	1.0	1.0
1000 m						
1st (°C)	-0.3±1.6	0±1.6	~0	0.5	0.3	1.0
2nd (°C)	-0.3±1.6	0±1.6	~0	0.5	0.3	1.0
3rd (°C)	-0.3±1.6	0±1.6	~0	0.5	0.3	1.0

4.1.2.3 Sampling Speed

Similar to the change in sampling pattern, changing the speed had very little effect on the mean distribution derived from the sampling results for both the increased and reduced speeds (Table 4.5). There were no differences between the HOFPs for the entire episode, except for 6 August, when the cold front went through.

On 6 August, the sampling with reduced speed shows a dramatic increase (up to 4°C) in dewpoint temperatures on the western portion of the sampling domain during the second HOFP. This increase was not seen at any other speed. The increase in dewpoint temperatures was only present over areas that were passed over on the early hours (00-04 UTC) of 7 August

because the flight duration for covering the entire sampling domain when flying at the reduced speed amounted to a total of 28 hours.

Other than the combination of reduced speed and the passing of the cold front, the sampling flight speed does not appear to have an influence on the mean dewpoint temperature distributions constructed from the sampled data even when there was a temporal trend in dewpoint temperatures.

Differences between sampled mean dewpoint temperatures and the 20 hour 'grand truth' values only occurred with the UAV travelling at its minimum speed. The differences occurred only in the western portion of the domain (Figure 4.5b) because this portion contains temperature samples only from the beginning of the day. Other than these differences sampling speed and pattern did not have any effect on dewpoint temperatures in Interior Alaska, where there is little diurnal variability of dewpoint temperatures.

Table 4.5 Means and standard deviations, and skill scores of dewpoint temperatures for the various sampling speeds at 200 m, 500 m and 1000 m height determined over the entire episode and sampling. Note that the 1st sampling pattern is the default.

Sampling Speed	Grand Truth	Sampled	RMSE	SDE	Bias	Correlation
200 m						
Maximum (°C)	1.0±0.3	1.0±1.0	~0	0.5	~0	1.0
Cruising (°C)	1.0±0.3	1.0±0.3	~0	0.5	~0	1.0
Minimum (°C)	1.0±0.3	1.6±0.6	0.7	1.0	0.4	0.3
500 m						
Maximum (°C)	0.5±1.5	0.5±1.5	~0	0.5	~0	1.0
Cruising (°C)	0.5±1.5	0.5±1.5	~0	0.5	1.0	1.0
Minimum (°C)	0.5±1.5	1.3±1.2	1.4	1.3	0.6	0.5
1000 m						
Maximum (°C)	-0.3±1.6	-0.3±1.6	~0	0.5	~0	1.0
Cruising (°C)	-0.3±1.6	0±1.6	~0	0.5	0.3	1.0
Minimum (°C)	-0.3±1.6	0.4±1.6	1.2	1.1	.5	0.6
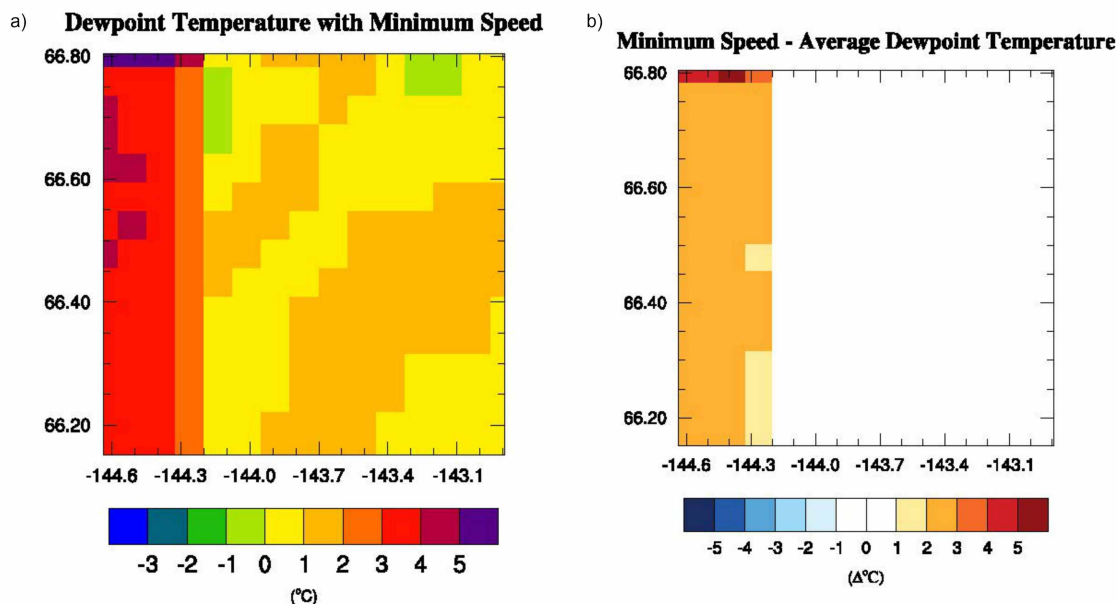
Figure 4.5 Sampled dewpoint temperature data with UAV travelling at its minimum speed a). The difference between the sampled temperatures and the 20 hour average 'grand truth' is shown in b). The 20 hour average 'grand truth' is shown in Figure 4.4 for 6 August 2009.

4.2 Gases

4.2.1 Inert Gas – CO

The National Ambient Air Quality Standard (NAAQS) for CO is currently 35 ppm in one hour or 9 ppm in an eight-hour average. Typically, the ambient CO concentration in Interior Alaska is about 3 ppm. During a wildfire the air quality will decrease not only over the fire, but also downwind due to transport.

Compared to some gases (CH_4, N_2O) that are present in Earth's atmosphere CO has a relatively short lifetime, on the order of months (Prather, 1996). However, when compared to the other gases that are emitted from wildfires CO's lifetime is relatively long, and can be used to track smoke from wildfires.

4.2.1.1 Sampling Height

The examination of the CO concentrations at varying heights showed that there was not much variation except for the typical decrease of CO concentrations with height (Figures 4.6 and 4.7). This vertical profile results from the CO source being at the ground. For example, the maximum concentration at 200 m on 7 August was 0.34 ppm, and at 1000 m the maximum concentration was 0.30 ppm. A contributing factor for this small concentration difference over this height span was the washout from the passage of the cold front on 6 August. While 5 August had a difference of 13.18 ppm between the 200 m and 1000 m levels, the time required for model spinup for chemistry permits no reliable discussion prior to the third day into the integration.

The beginning of 6 August had pre-frontal conditions with higher CO concentrations and greater differences between height levels than the CO concentrations on the days post cold front. For example, the difference in CO maximum concentrations between 200 m and 1000 m is 2.8 ppm. This difference is considerably larger than the 0.04 ppm difference on 7 August between these heights. For the duration of the study, absolute differences in the minimum values remained less than 1 ppm and absolute differences in the average concentrations were between 0 and 2 ppm (Figure 4.7). Based on the average differences, it is reasonable to conclude that excluding times of high concentration, i.e. sampling in the plume above the fire, using the lowest sampling height presents a reasonable picture of the CO concentrations from wildfire emissions in the first 200 to 1000 m of the atmospheric boundary layer. The 20 hour average CO concentrations at 200 m, 500 m, and 1000 m are shown in Figure 4.6.

When concentrations are compared at the various heights there is no large difference, allowing for the 200 m height to be used for further detailed discussion of the other experiments.

When comparing the CO concentrations sampled along the individual flight paths to the average CO concentration during the flight duration of 20 hours, it can be expected that with consistent atmospheric conditions the findings will be similar on a day-to-day basis.
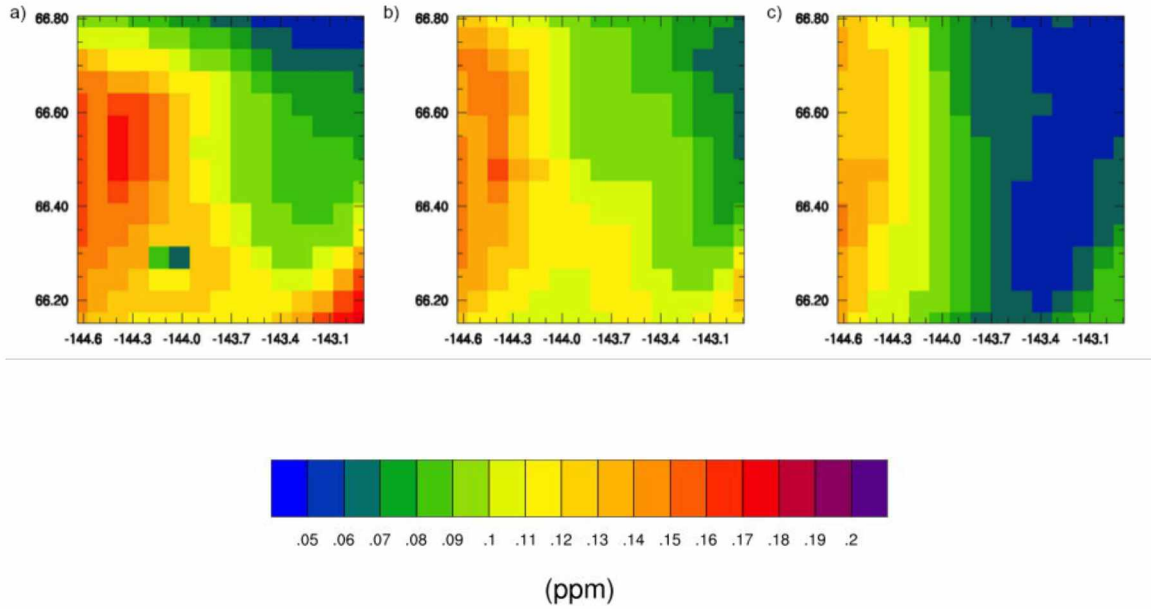
Figure 4.6 20 hour average 'grand truth' concentrations of CO at a) 200 m b) 500 m c) 1000 m heights for 7 August.
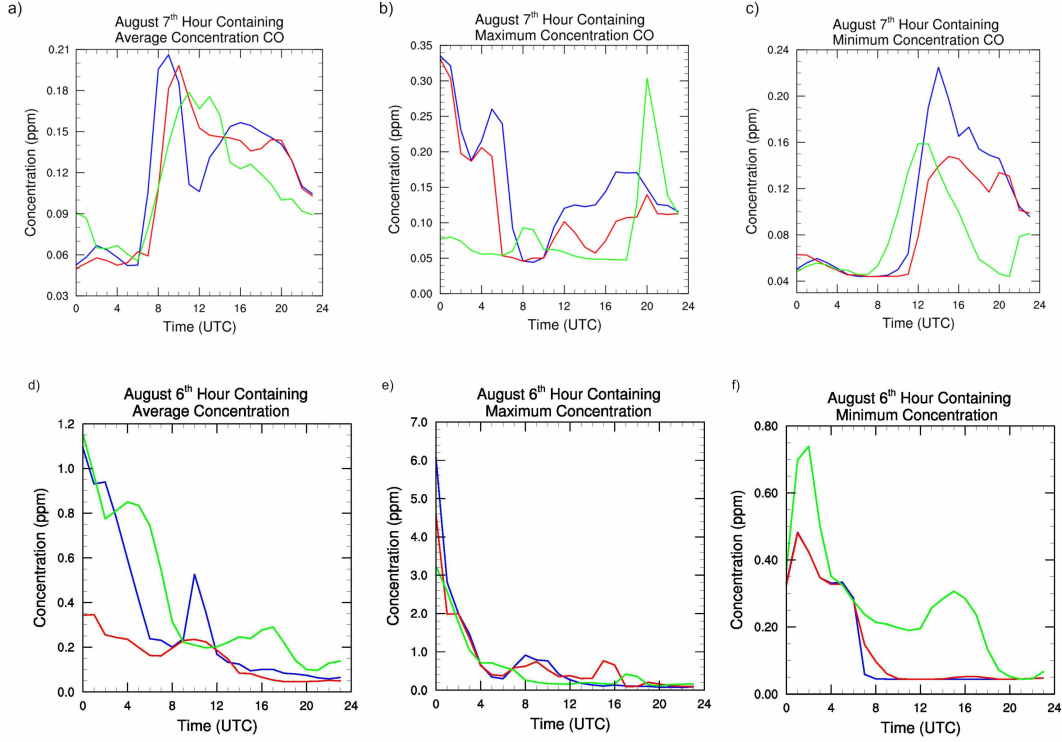
Figure 4.7: Average, maximum, and minimum CO concentrations at 200 m (blue), 500 m (red), and 1000 m (green). 7 August (a-c) shows typical conditions following precipitation. 6 August (d-f) shows a typical relationship of CO concentrations during the passage of the cold front.

4.2.1.2 Sampling Pattern

The first two sampling patterns produced similar 20 hour mean spatial CO concentration distributions in terms of where high and low concentrations of CO were located within the sampling domain. However, the second sampling pattern consistently had higher concentrations at hot spot regions when compared to the first sampling pattern. The third sampling pattern produced a different orientation of the gradient in CO concentrations than the former sampling pattern and the 20 hour mean distribution calculated from the WRF/Chem data (Figure 4.8). Specifically if high concentrations were seen in the south for the first and second sampling patterns, the third sampling pattern often suggested high concentrations to the north due to the different time at which the UAV went over the areas. This finding means

81

that the sampling pattern may affect the obtained spatial distribution and its extremes when the plume dispersion varies in space and/or time.

Overall the changes in sampling pattern did not increase or decrease the differences between the averaged sampled concentrations and the 20 hour 'grand truth'. Concentrations did vary between the sampling patterns, but these differences were little and are due to the timing of the UAV passing over the area.

Based off of Table 4.6 it can be seen that sampling patterns make little difference in the sampling of inert gases. Errors from sampling decrease at higher altitudes, most likely due to the gas being more dispersed in the horizontal plane.

Table 4.6 Means and standard deviations, and skill scores of CO concentration for the various sampling patterns at 200 m, 500 m and 1000 m height determined over the entire episode and sampling. Note that the 1st sampling pattern is the default.

Sampling Pattern	Grand Truth	Sampled	RMSE	SDE	Bias	Correlation
200 m						
1st (ppm)	0.2±0.4	0.2±0.6	0.1	0.1	-0.1	0.8
2nd (ppm)	0.2±0.4	0.2±1.4	0.2	0.2	0.1	0.7
3rd (ppm)	0.2±0.4	0.2±0.2	0.1	0.1	-0.2	0.7
500 m						
1st (ppm)	0.1±0.1	0.1±0.1	0.02	0.03	-0.1	0.7
2nd (ppm)	0.1±0.1	0.1±0.2	0.01	0.02	-0.1	0.7
3rd (ppm)	0.1±0.1	0.1±0.1	0.02	0.04	0.1	0.9
1000 m						
1st (ppm)	0.1±0.2	0.1±0.1	0.02	0.03	-0.1	0.8
2nd (ppm)	0.1±0.2	0.1±0.1	0.01	0.03	-0.1	0.9
3rd (ppm)	0.1±0.2	0.1±0.1	0.02	0.04	0.1	0.9
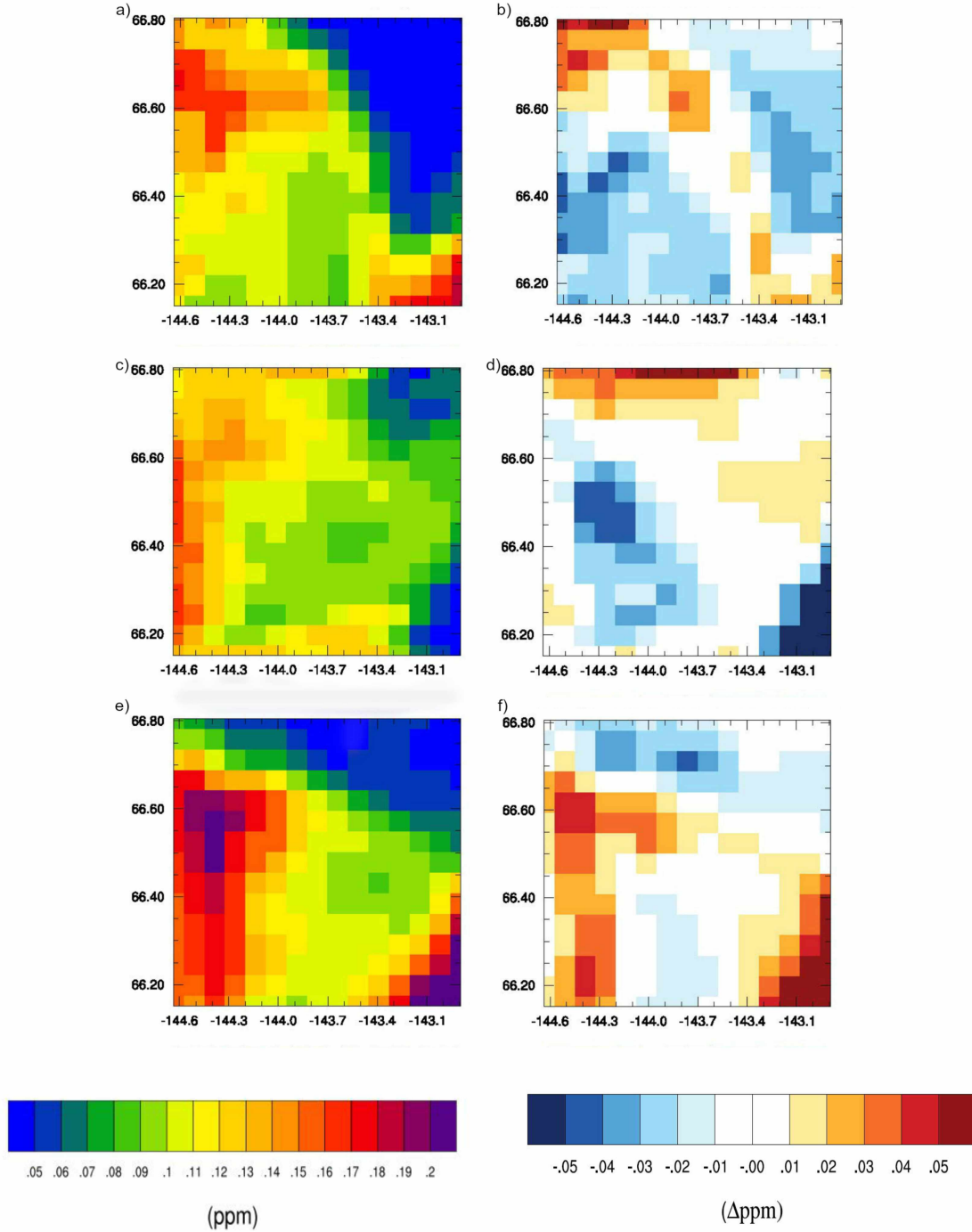
Figure 4.8: CO concentrations recorded by UAV on 7 August. a-b) CO concentration sampled and the difference between that and the 'grand truth' for the 1st sampling pattern. c-d) CO concentrations for the 2nd sampling pattern and the difference between the concentrations and the 'grand truth'. e-f) CO concentrations sampled with the 3rd sampling pattern and the difference between that and the 'grand truth'. The 'grand truth' concentrations for the 200 m height can be seen in Figure 4.6a

4.2.1.3 Sampling Speed

With only minor differences (less than 20 ppb) between the CO concentration distributions obtained for sampling at minimum speed, cruising speed, and maximum speed of the UAV, one can conclude that flight speed does not play a role for the accuracy of the derived concentration distribution in the case of non-reactive gases. When compared to the 20 hour average, the first HOFP overestimated CO concentrations on average 0.14 ppm as compared to the WRF/Chem mean distribution. The second HOFP was underestimating concentrations on average by 0.11 ppm as compared to the WRF/Chem mean distribution. These errors were mainly located in the southeast sector of the UAV sampling domain. Elsewhere the sampled CO concentrations do not create notable errors when compared to the 20 hour mean 'grand truth'.

Results from the change in speed were similar to that with the change in sampling pattern. As a result of CO having a long lifetime (relative to other gases released from fires) it can be concluded that neither speed nor sampling pattern makes a large difference in the sampling of CO concentrations.

As seen in Table 4.7 when the UAV travels at the maximum speed the correlation does increase slightly when compared to other sampling speeds at the corresponding heights. The error associated with sampling at different heights decreases with an increase in height.

Table 4.7 Means and standard deviations, and skill scores of CO concentration for the various speeds at 200 m, 500 m and 1000 m height determined over the entire episode and sampling. Note that the 1st sampling pattern is the default.

Sampling Speed	Grand Truth	Sampled	RMSE	SDE	Bias	Correlation
200 m						
Maximum (ppm)	0.2±0.4	0.2±0.9	0.1	0.2	0.1	0.9
Cruising (ppm)	0.2±0.4	0.2±0.6	0.1	0.1	-0.1	0.8
Minimum (ppm)	0.2±0.4	0.2±0.6	0.1	0.1	-0.2	0.6
500 m						
Maximum (ppm)	0.1±0.1	0.1±0.1	0.03	0.04	-0.1	0.8
Cruising (ppm)	0.1±0.1	0.1±0.1	0.02	0.02	-0.1	0.6
Minimum (ppm)	0.1±0.1	0.1±0.1	0.05	0.04	0.4	0.7
1000 m						
Maximum (ppm)	0.1±0.2	0.1±0.1	0.01	0.03	~0	0.9
Cruising (ppm)	0.1±0.2	0.1±0.1	0.01	0.03	-0.1	0.9
Minimum (ppm)	0.1±0.2	0.1±0.1	0.02	0.03	-0.1	0.8

4.2.2 Primary Pollutants

Primary pollutants from wildfires are any pollutant that is released directly from the fire and has not undergone any chemical reaction. In this thesis, SO_2 and NO are primary pollutants that have the highest concentrations, and undergo reactions forming secondary pollutants and are also precursor gases for aerosols.

Commonly, SO_2 reacts with other compounds to form PM. In addition, to NO contributing to nitrate aerosol formation there are, among others, the reaction between NO and O_3 to produce O_2 and NO_2.

$$NO + O_3 \rightarrow NO_2 + O_2 \hspace{4cm} 4.1$$

4.2.2.1 SO_2

According to the EPA, the NAAQS for primary SO_2 is set at 75 ppb in 1 hour (EPA, 2015). In Interior Alaska, the typical concentrations for SO_2 is approximately 35 ppb. Values above the 35 ppb will be a decrease in air quality for this region of Alaska, and any concentration above 75 ppb is in violation of air quality standards.

The 20 hour average concentration distribution of SO_2 or the 'grand truth' values all had the highest values at the edge of the UAV sampling domain (cf. Figure 4.9). Advection also assisted in the spatial distribution of SO_2 as seen in Figure 4.9.
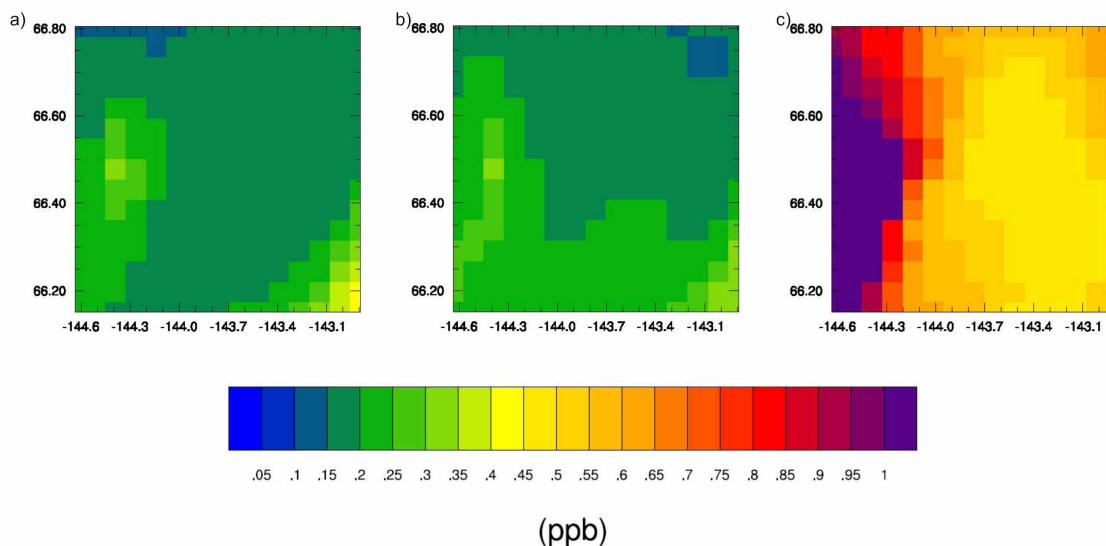
Figure 4.9 20 hour average SO_2 concentrations for 7 August according to the 'grand truth' at 200 m (a), 500 m (b), and 1000 m (c).

4.2.2.1.1 Sampling Height

Differences between average concentrations at varying heights were consistently close to 0 ppm (therefore not shown). When there were peak SO_2 concentrations they were recorded at higher altitudes, but these higher concentrations were hardly different from those at lower altitudes, and to recommend a higher altitude for the sampling than 200 m would not change the results.

Unlike the results obtained for CO, SO_2 does not have any clear trends to its biases. Strong negative and positive biases as well as values around zero occur for both NMB and FB throughout the episode.

Distinct differences in SO_2, occurred between the first and second HOFPs; lower SO_2 concentrations typically occurred during the first HOFP than during the second HOFP. This is a result of the timing of photolytic reactions.

Other reactions may also be occurring with trace gases such as dimethyl sulfide (DMS), which is a common trace gas released during the burning of some plants. No evidence was seen of gaseous SO_2 forming solid

87

aerosols that would be classified as particulate matter as the decrease of SO_2 was not correlated spatially with increase in particulate matter.

4.2.2.1.2 Sampling Pattern

After the passage of the cold front on 7 August, the difference between the 20 hour average and the sampled SO_2 concentrations from a UAV flight was approximately 0 ppm for the majority of the UAV sampling domain excluding the southeast corner for all sampling patterns. During this time, a northwest wind pushed the smoke plume to the southeast. There were higher SO_2 concentrations in the southeast corner compared to the rest of the sampling domain that were only present with the first HOFP for the first and third patterns (Figure 4.10). The second sampling pattern did not exhibit these concentrations because the UAV went over the southeast corner early in the day when the center of the low-pressure system was located near the southeast corner of the UAV sampling domain leading to a northwesterly wind in this area.

By the second HOFP on 8 August, the highest SO_2 concentrations were located at the central and northern portion of the UAV sampling domain due to a southwesterly wind shifting the position of the plume from the southeast to the central/northern portion. The wind speeds were lower than on 7 August allowing for the plume to be more dispersed, rather than containing it to an area as was true on the preceding day. For sampling it is crucial to consider wind direction and speed as to make sure the highest concentrations are sampled.

Regardless of the sampling pattern the largest differences between the average sampled concentrations and the 20 hour 'grand truth' values occurred along the edges of the sampling domain. This trend in differences was true for all days during the episode.
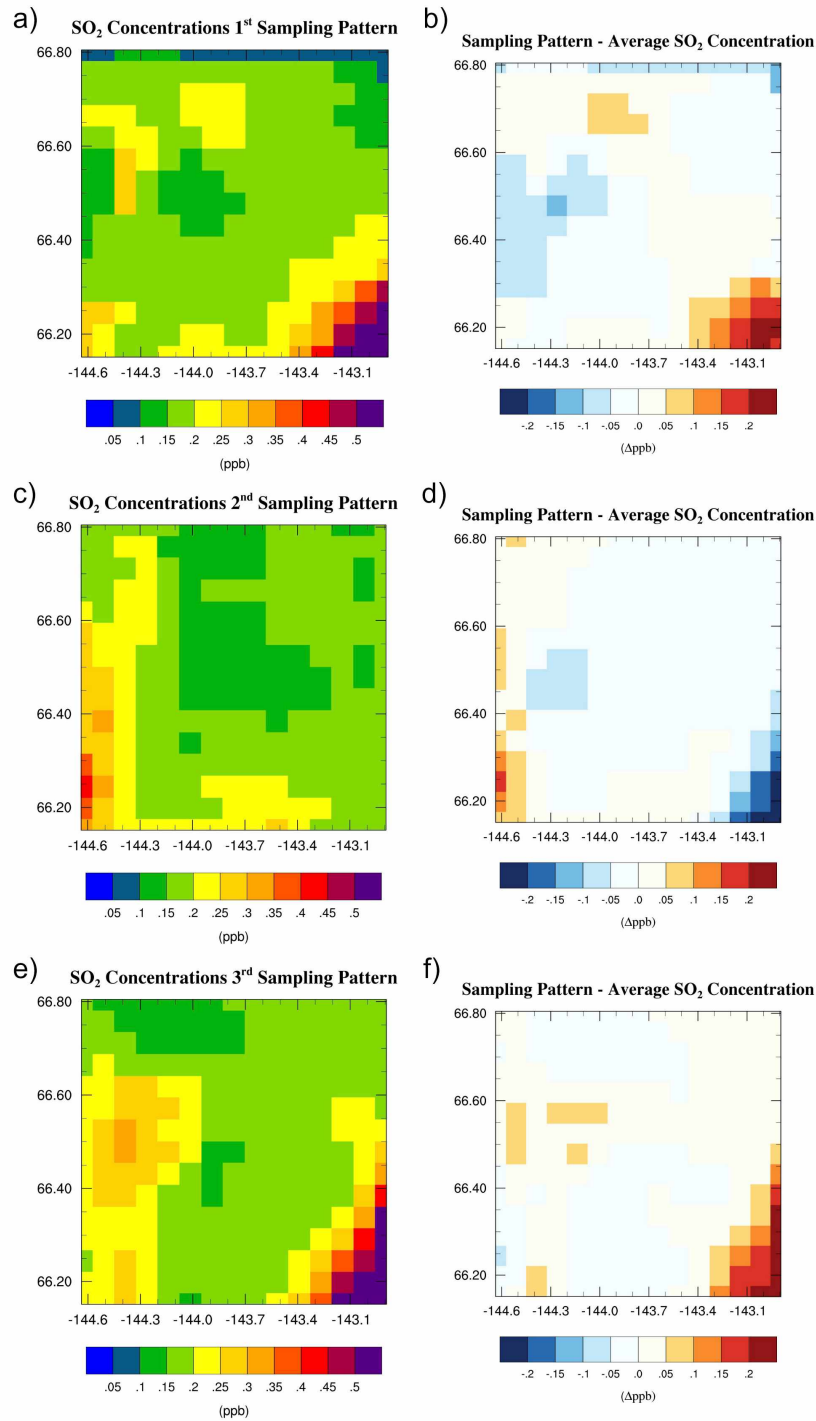
Figure 4.10 Average sampled concentrations of SO_2 in ppb on 7 August. a-b) 1st sampling pattern concentrations and the difference between the mean concentrations derived from the sampling and the 'grand truth' values. c-d) 2nd sampling pattern determined concentrations and the respective difference. e-f) 3rd sampling pattern determined concentrations and its difference values. 'Grand truth' concentrations are displayed in Figure 4.9.

4.2.2.1.3 Sampling Speed

No definitive features existed regarding whether speed made a difference when monitoring SO_2 from a UAV. For instance, SO_2 was overestimated and underestimated within areas of high and low concentrations, respectively, when the UAV was travelling at its maximum speed on 6 August. The same was found when the UAV traveled at the stall speed as well. These trends were most obvious for 6 August prior to the passing of the cold front, but they were still present after the passing of the cold front but to a lower magnitude.

Overall, when the UAV was travelling at the stall speed there was more variability in the SO_2 concentrations than with the standard cruising speed and the maximum speed possible (Table 4.8). This means that the spatial and temporal fine structure is better captured with minimum speed than maximum in the case of SO_2.

Table 4.8 Means and standard deviations, and skill scores of SO_2 concentration for the various speeds at 200 m, 500 m and 1000 m height determined over the entire episode and sampling. Note that the 1st sampling pattern is the default.

Flight Speed	Grand Truth	Sampled	RMSE	SDE	Bias	Correlation
200 m						
Maximum (ppb)	0.4±1.0	0.5±1.5	0.3	0.4	0.1	0.7
Cruising (ppb)	0.4±1.0	0.4±1.2	0.5	0.3	0.7	0.6
Minimum (ppb)	0.4±1.0	0.4±1.1	0.2	0.2	-0.1	0.6
500 m						
Maximum (ppb)	0.2±0.9	0.2±0.4	0.1	0.1	0.1	0.9
Cruising (ppb)	0.2±0.9	0.2±0.2	0.1	0.1	-0.1	0.7
Minimum (ppb)	0.2±0.9	0.2±0.5	0.1	0.1	~0	0.8
1000 m						
Maximum (ppb)	0.7±2.6	0.8±3.0	0.4	0.7	0.2	0.9
Cruising (ppb)	0.7±2.6	0.2±2.0	0.5	0.4	0.2	0.9
Minimum (ppb)	0.7±2.6	0.6±0.5	0.4	0.5	-0.2	0.6

The 20 hour average sampled concentrations are roughly similar to not only the 'grand truth', but also to the concentrations obtained at other speeds. However, when the UAV travelled at its stall speed larger differences were spread throughout the UAV domain and not in a localized area as was true

91

for when the UAV traveled at its cruising and maximum speeds (Figure 4.11 and Table 4.8). It would be advised to sample SO_2 concentrations at cruise to maximum speeds to minimize the errors.
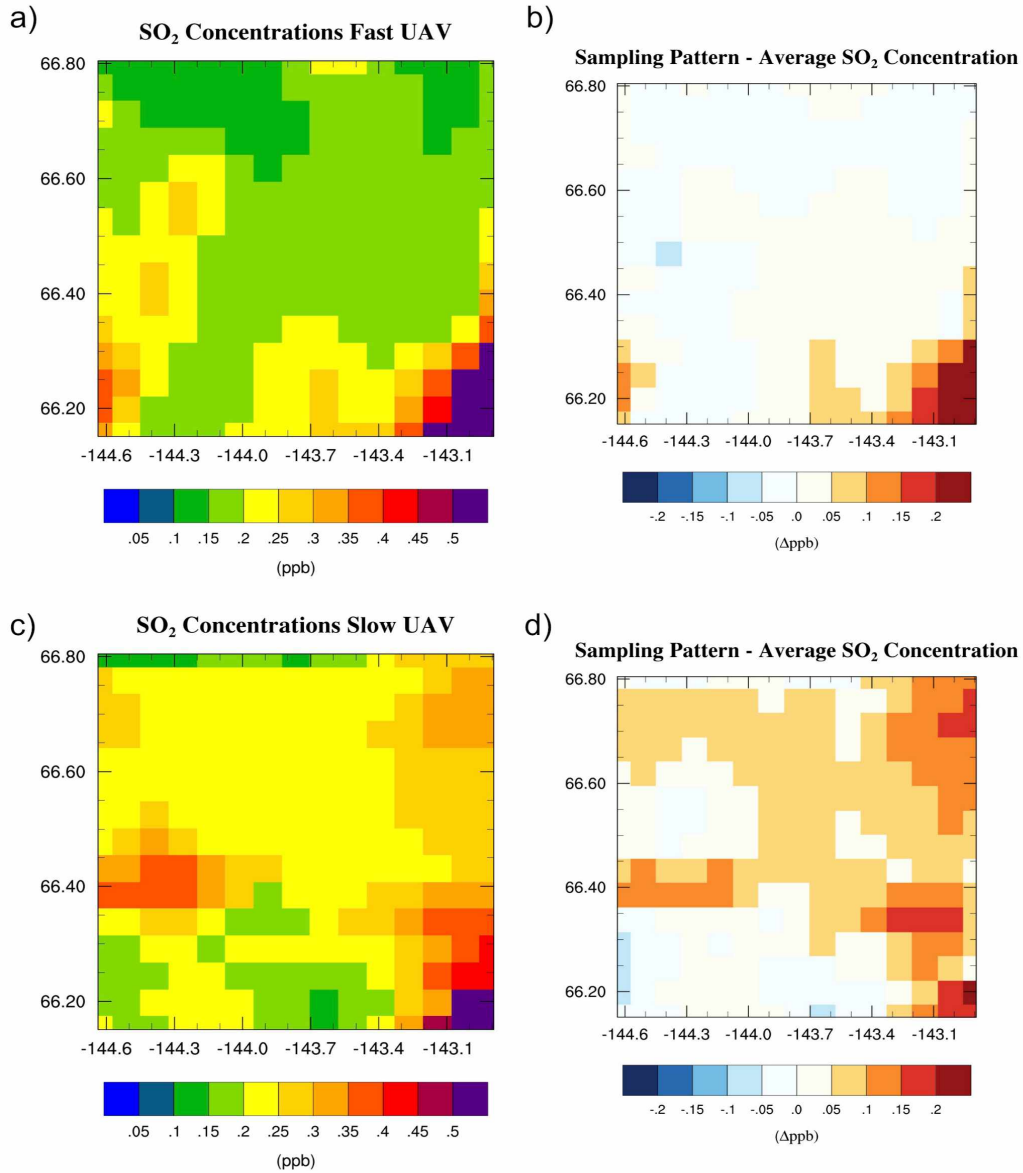
Figure 4.11: Sampled SO_2 concentrations for 7 August with UAV travelling at various speeds. a-b) Concentrations and differences from the 'grand truth' for when UAV was travelling at its maximum speed. c-d) Concentrations and differences from the 'grand truth' for when the UAV was travelling at its minimum speed. The 'grand truth' values are shown in Figure 4.9, and the concentrations and differences for when the UAV travelled at its minimum speed is Figure 4.10 a, b.

4.2.2.2 NO

The main sources of NO in the troposphere are from the combustion of fossil fuels, biomass burning, lightning, microbial processes in soils, and stratospheric downwelling (Logan, 1983). In this episode over northern Interior Alaska, the main source of NO is the fire. Nitric oxide rapidly reacts with ozone producing nitrogen dioxide and dioxygen (Equation 4.1). NO_2 then undergoes photolysis producing NO and O (Logan, 1983).

Due to the reactivity of NO, the NAAQS is for NO_2 with the maximum concentration for a one hour average being 100 ppb.

4.2.2.2.1 Sampling Height

The overall maximum concentration of NO was 1 ppb occurred on 6 August during hour 16 of the flight. During the hours of 06-13 UTC, the NO concentrations consistently dropped to $1.0 \cdot 10^{-6}$ ppm. During these hours, the sun is low in the sky and little solar radiation is reaching the lower atmosphere. As a result, photochemical reactions either drop in efficiency or cease altogether. In the latter case, the lack of photolysis is causing the dramatic decrease in NO concentrations; with no photolytic reactions occurring, O_3 is not breaking down into its oxygen components and is free to bond with NO to form NO_2 and O_2 (Equation 4.1).

As a result, values for the first HOFP were considerably lower when compared to the second HOFP; the greatest difference being 15 ppb. Other than this reaction, NO showed very similar behavior than discussed above for SO_2.

When comparing the 20 hour average values at various heights the average difference between the concentrations was approximately 0.002 ppb, with the a similar spatial distribution with very little offset. An example of the spatial distribution is seen in Figure 4.12 with maximum concentrations in the southeast corner and a second hot spot in the west. Throughout the

episode there was near constant concentrations of NO in the central region of the UAV domain.
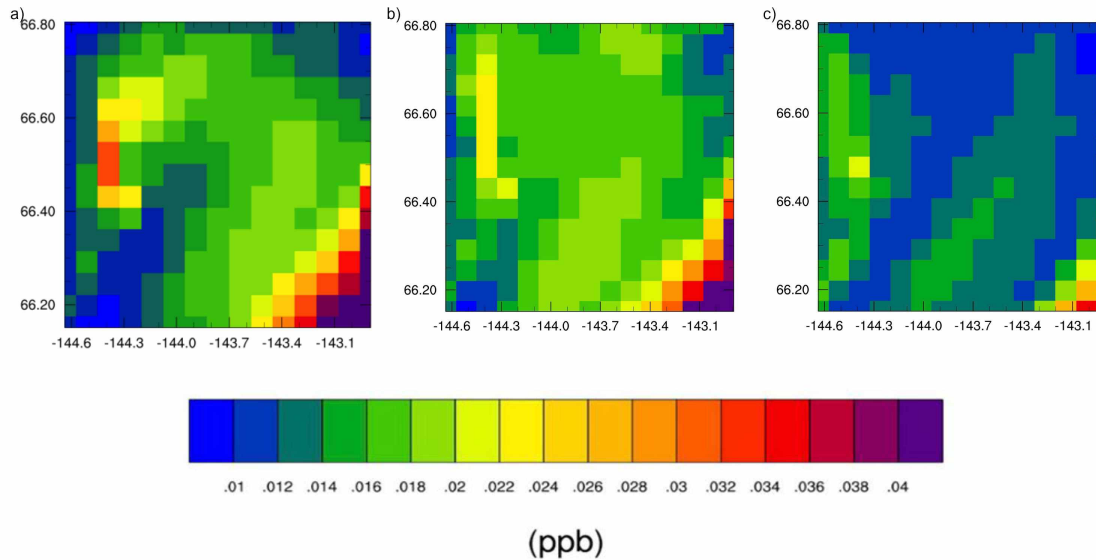
Figure 4.12 20 hour 'grand truth' average of NO concentrations at a) 200 m, b) 500 m, and c) 1000 m on 7 August.

4.2.2.2.2 Sampling Pattern

Changing the sampling pattern affected the location where the 20 hour mean distribution would display the high concentrations of NO when there was no photolysis to reduce the concentrations. The highest NO concentrations were in locations where the UAV traveled over in the morning or evening hours.

Higher concentrations were more dispersed through the UAV sampling domain on 6 August prior to the passing of the cold front; after this frontal passage, elevated NO concentrations were more localized (Figure 4.13).

The HOFP that records the highest NO concentrations is dependent on when the UAV travels over the area of highest concentrations meaning that the sampling of NO is time dependent. On 6 August, the highest NO concentrations with the first sampling pattern were recorded in the second HOFP, but with the second sampling pattern the highest NO concentrations

94

were recorded for the first HOFP. This means that because of the photolytic reactions involving NO, concentrations can differ depending on the time they were recorded.
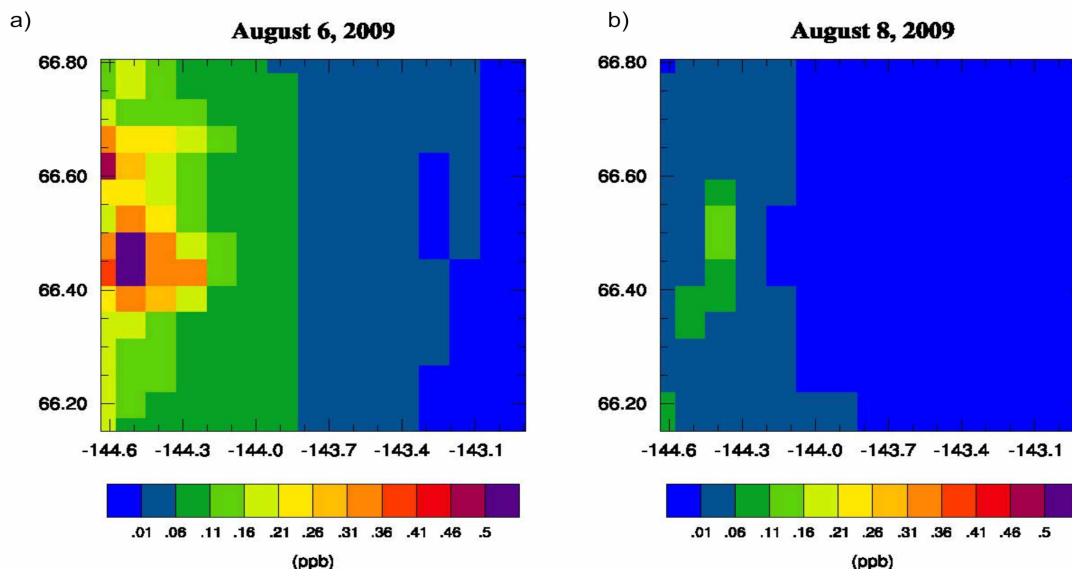
Figure 4.13 NO concentrations for second sampling pattern and first HOFP for 6 August (a) and 8 August (b).

In areas with high concentrations of NO, concentrations were overestimated when constructing the spatial distribution from the sampled values as compared to the 20 hour average of the 'grand truth'. The NO concentrations were underestimated in areas with low concentrations when compared to the 20 hour average of the 'grand truth'. This underestimation is a result of the 20 hour average's including unequal amounts of hours with day-time and night-time dominated chemistry (Equation 4.1).

This result suggests that sampling NO concentrations over the majority of a day, which are dominated by photolytic reactions, decreased the concentrations for much of the sampled domain. The opposite is true for areas where the UAV records high concentrations. Thus, one may conclude that spatial distributions containing reactive species that are influenced by

photochemistry should only be constructed separately for conditions when daytime and nighttime chemistry occur.

Table 4.9 Means and standard deviations, and skill scores of NO concentration for the various sampling patterns at 200 m, 500 m and 1000 m height determined over the entire episode and sampling. Note that the 1st sampling pattern is the default.

Sampling Pattern	Grand Truth	Sampled	RMSE	SDE	Bias	Correlation
200 m						
1st (ppb)	0.03 ±0.1	0.75±0.2	0.01	0.01	0.2	0.6
2nd (ppb)	0.03 ±0.1	0.03±0.2	0.03	0.03	-0.1	0.2
3rd (ppb)	0.03 ±0.1	0.02±0.2	0.04	0.03	-0.3	0.6
500 m						
1st (ppb)	0.02±0.4	0.02±0.1	0.02	0.01	-0.3	-0.3
2nd (ppb)	0.02±0.4	0.02±0.1	0.01	0.01	-0.2	-0.2
3rd (ppb)	0.02±0.4	0.02±0.2	0.02	0.03	0.1	0.8
1000 m						
1st (ppb)	0.01±0.2	0.01±0.1	0.01	0.01	-0.1	0.4
2nd (ppb)	0.01±0.2	0.01±0.1	0.01	0.01	-0.2	0.1
3rd (ppb)	0.01±0.2	0.01±0.1	0.01	0.02	0.1	0.7

There was a large variation between the 20 hour average sampled NO concentration with respect to the biases and the correlations when the UAV flew along different sampling patterns (Table 4.9). Recall that NO concentrations regularly dropped between the hours of 06 and 13 UTC.

Based on the large differences between sampling patterns it is recommended to take samples of NO prior to or after the photolytic reaction (Equation 4.1) to avoid the large variations.

At the 500 m height, the correlations for the first and second sampling patterns are negative, this is likely a result from the rainout on 6 August.

The reason for these sampling patterns' correlation being negative is that at this altitude the precipitation was more variable in time. At the 200 m level precipitation was consistent during the hours when cold front was passing. Whereas at the 500 m height precipitation during sampling did not match what the 20 hour 'grand truth' was recording.

4.2.2.2.3 Sampling Speed

With all speeds examined in this study, the differences between the 20 hour average from sampling and the 20 hour average 'grand truth' occurred mainly along the edges of the UAV sampling domain rather than in the center (Figure 4.14). The differences are related to when the UAV goes over the area. Along the edges of the sampling domain, the NO concentrations are either recorded prior to or after the occurrence of photochemical reactions. When the UAV samples data prior to the dominance of photochemistry, the 'true' NO values are overestimated by 0.1 to 0.3 ppb (Table 4.10).

Due to the long daylight hours at this latitude even in August (approximately 18 hours between sunrise and sunset), the 20 hour mean NO concentration distribution obtained from the UAV observations underestimated the 20 hour mean of the 'grand truth' by a maximum of 0.2 ppb.
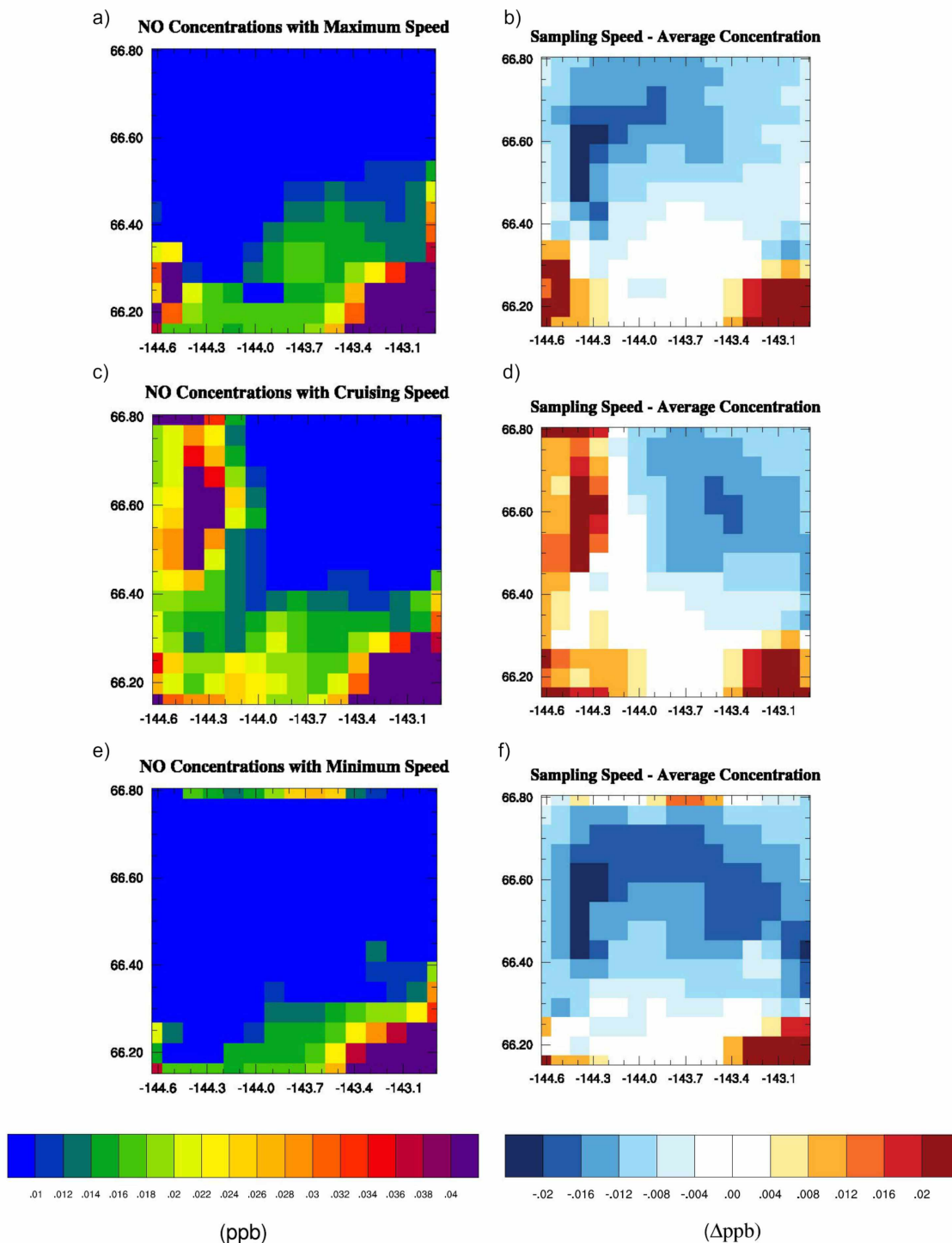
Figure 4.14 Average sampled concentrations of NO in ppb on 7 August. a-b) Maximum sampling speed concentrations and the difference between sampled concentrations and the 'grand truth' values. c-d) Cruising speed concentrations and the respective difference. e-f) Minimum speed concentrations and its difference values. 'Grand truth' concentrations seen in Figure 4.12.

Table 4.10 Means and standard deviations, and skill scores of NO concentration for the various speeds at 200 m, 500 m and 1000 m height determined over the entire episode and sampling. Note that the 1st sampling pattern is the default.

Flight Speed	Grand Truth	Sampled	RMSE	SDE	Bias	Correlation
200 m						
Maximum (ppb)	0.03 ±0.1	0.02±0.2	0.03	0.03	-0.2	0.7
Cruising (ppb)	0.03 ±0.1	0.75±0.2	0.01	0.01	0.2	0.6
Minimum (ppb)	0.03 ±0.1	0.03±0.2	0.03	0.03	0.2	0.5
500 m						
Maximum (ppb)	0.02±0.4	0.01±0.2	0.02	0.02	-0.2	0.8
Cruising (ppb)	0.02±0.4	0.02±0.1	0.02	0.01	-0.3	-0.3
Minimum (ppb)	0.02±0.4	0.02±0.2	0.02	0.02	0.3	0.7
1000 m						
Maximum (ppb)	0.01±0.2	0.01±0.1	0.01	0.02	-0.2	0.7
Cruising (ppb)	0.01±0.2	0.01±0.1	0.01	0.01	-0.1	0.4
Minimum (ppb)	0.01±0.2	0.01±0.1	0.01	0.02	0.2	0.7

When examining the differences in concentrations of NO with varying UAV speed there is less variation than when the UAV travelled different sampling pattern. The UAV was able to sample both high and low concentrations of NO for all speeds the only difference being the spatial placement of the high concentrations. Errors do still occur because of the decrease in concentrations every day and the time when the UAV flew over an area.

A close examination of the HOFP was done because of the distinct differences in NO concentrations that occur every day.

The signs of the average biases for the varying speeds were reversed for each HOFP, the magnitudes between HOFPs were not similar. When the UAV travelled at its maximum speed, the FB for the first HOFP was 35%, whereas for the second HOFP the FB -780%. The NMB for the first and second HOFP were 12% and -163%, respectively. The positive bias for the first HOFP was the result of most of the sampling taking place before photolysis set on.

The signs for the biases obtained for the minimum speed were opposite of that obtained of the fast-moving UAV. The FB and NMB were -6% and -76% for the first HOFP, while they were 18% and 12%, respectively, for the second HOFP. The time where the NO concentrations drop down to 1 ppt was sampled by the UAV only in the first HOFP. All of the second HOFP occurred later in the day when the photochemical reactions are not as strong and NO concentrations can build up. This means that NO concentrations sampled by the UAV were low in the first HOFP due to the decrease in NO concentrations. When the UAV sampled its second HOFP NO concentrations were building back up by the photolysis of NO_2.

Based on these findings for a UAV to monitor the primary pollutant NO, it would be recommended that individual flights occur during either day or night, as photochemistry really affects the results.

The recommendation to sample prior to or after the photochemical reactions that was mentioned in section 4.2.2.2.2 still holds true for varying speeds.

4.2.3 Secondary Pollutant – O_3

Secondary pollutants are the product of some reaction involving primary pollutants. The ozone present during this event is the result of the photolysis of $NO_x=NO+NO_2$ and VOCs. The NAAQS for O_3 is for an eight hour average concentration and its highest value without adverse health effects is 0.075 ppm. On average, the O_3 concentration in the Interior is 0.05 ppm.

Despite the creation of O_3, there were no observable peaks during any of the days. Despite the reactions with NO that occurred between 06 and 13 UTC, there was no minimum in the O_3 concentrations during that timeframe. At this time of the year, sunrise is between 04:30 and 05:00 AKDT and sunset is between 23:00 and 22:30 AKDT. Therefore, there was little time of complete darkness, so at least some photolysis occurred for most of the day keeping O_3 concentrations stable.

4.2.3.1 Sampling Height

Since NO was discussed in detail at the 200 m height, for consistence O_3 will also be discussed at the 200 m height. Despite nearly constant ozone values (Figure 4.15) there were consistent positive biases of 8 to 14% (NMB) and 8 to 12% (FB) for the first HOFP. The second HOFP has consistent negative biases ranging between -0.05% and -22% (NMB) and -5% and -35% (FB).
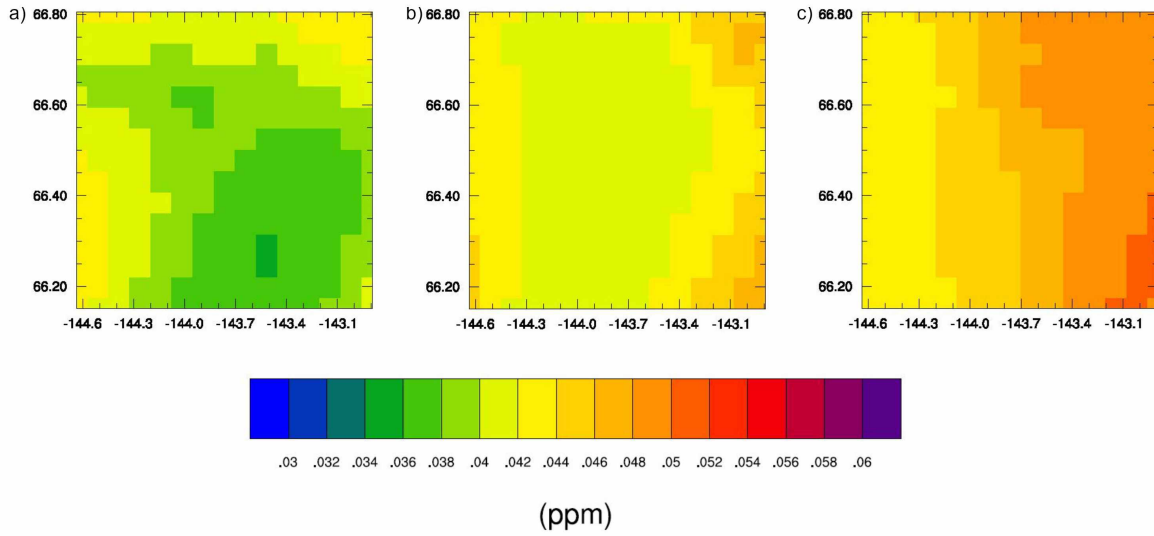
Figure 4.15 20 hour average concentrations of O_3 on 7 August for a) 200 m, b) 500 m and c) 1000 m heights. Fairly uniform 'grand truth' concentrations were observed for all days during the episode.

4.2.3.1 Sampling Pattern

Due to the low spatial and temporal changes gradients in O_3 the first and second sampling patterns produced similar results in terms of 20 hour mean O_3 concentration distributions, with only slight shifts in the orientation of the plume (Figure 4.16a, c, d). With this shift in the plume the differences between the 20 hour mean determined from the sampled concentrations and the 20 hour average 'grand truth' were also shifted (Figure 4.16b, d, f). The magnitudes of the differences were all fairly similar for all days during the episode.

The third sampling pattern showed the same trend as the other patterns for all days except the first HOFP on 6 August and the second HOFP on 8 August. Then the 20 hour mean O_3 concentrations obtained from the UAV sampling overestimated and underestimated, respectively, when compared to the 20 hour average O_3 concentrations of the 'grand truth'. The differences between the 20 hour mean O_3 concentrations obtained by the different sampling patterns were due to the orientation of the plume that changed with time depending on the prevailing wind direction.

102
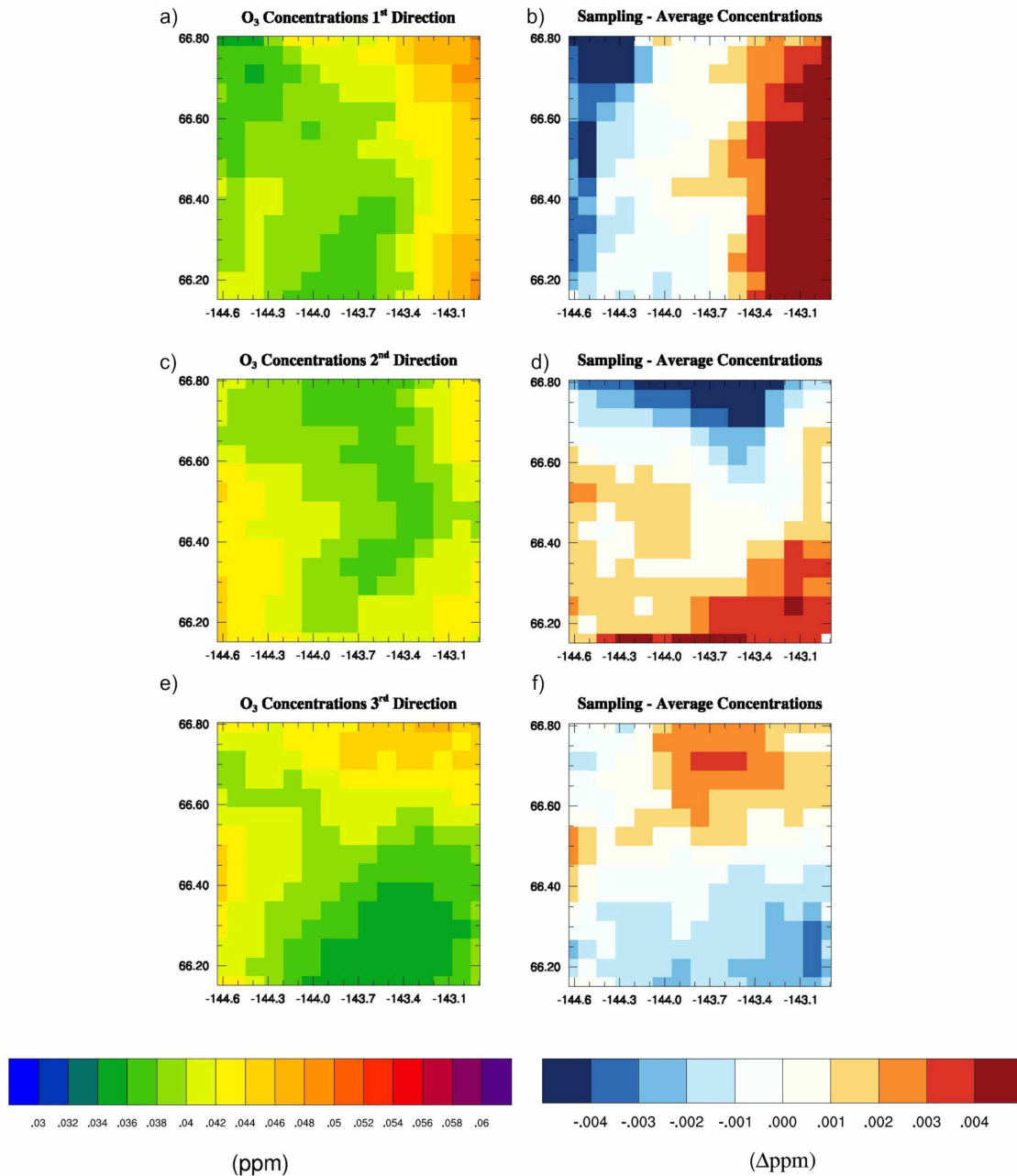
Figure 4.16 Average sampled concentrations of O_3 in ppm on 7 August. a-b) 1st sampling pattern concentrations and the difference between sampled concentrations and the 'grand truth' values. c-d) concentrations obtained by the 2nd sampling pattern and the respective difference. e-f) concentrations obtained by the 3rd sampling pattern and its difference values. 'Grand truth' concentrations seen in Figure 4.15.

103

4.2.3.3 Sampling Speed

The 20 hour mean O_3 concentrations were higher for both the data sampled at maximum and stall speeds compared to when the UAV was travelling at its standard cruising speed (Figure 4.17). 8 August's second HOFP was the only time when concentrations sampled at the cruising speed were higher than that of the maximum and minimum speeds. During this time, a tongue with O_3 concentrations less than 20 ppb extended from the south northward. The 20 hour mean O_3 concentration distributions derived from sampling at the maximum and stall speeds were also higher than those of the 20 hour average O_3 concentration distributions for all days and all HOFPs.

When the UAV traveled at its standard cruising speed, the obtained 20 hour mean O_3 values were the closest to the 20 hour average concentrations of the 'grand truth'.

Based on these findings, one has to conclude that the obtained 20 hour mean O_3 distribution is sensitive to the sampling speed. The fact that accuracy is less at enhanced as well as at reduced speed suggests that an optimum sampling speed may exist for O_3. Here further, investigations may be necessary to determine that speed.

Based on the distributions of 20 hour mean O_3 concentrations and their respective differences to the 'grand truth', it is recommended that for sampling of O_3 the UAV should travel at its regular cruising speed as slower and faster speeds skew results away from the 'grand truth'.

Figure 4.17 Average sampled concentrations of O_3 in ppm on 7 August with differing travel speeds. a-b) Concentrations obtained at the maximum sampling speed and the difference between sampled concentrations and the 'grand truth' values. c-d) Concentrations obtained at the cruising speed concentrations and the respective difference. e-f) Concentrations obtained at the stall speed and its difference values. The 'grand truth' can be seen in Figure 4.15.

4.3 Particles
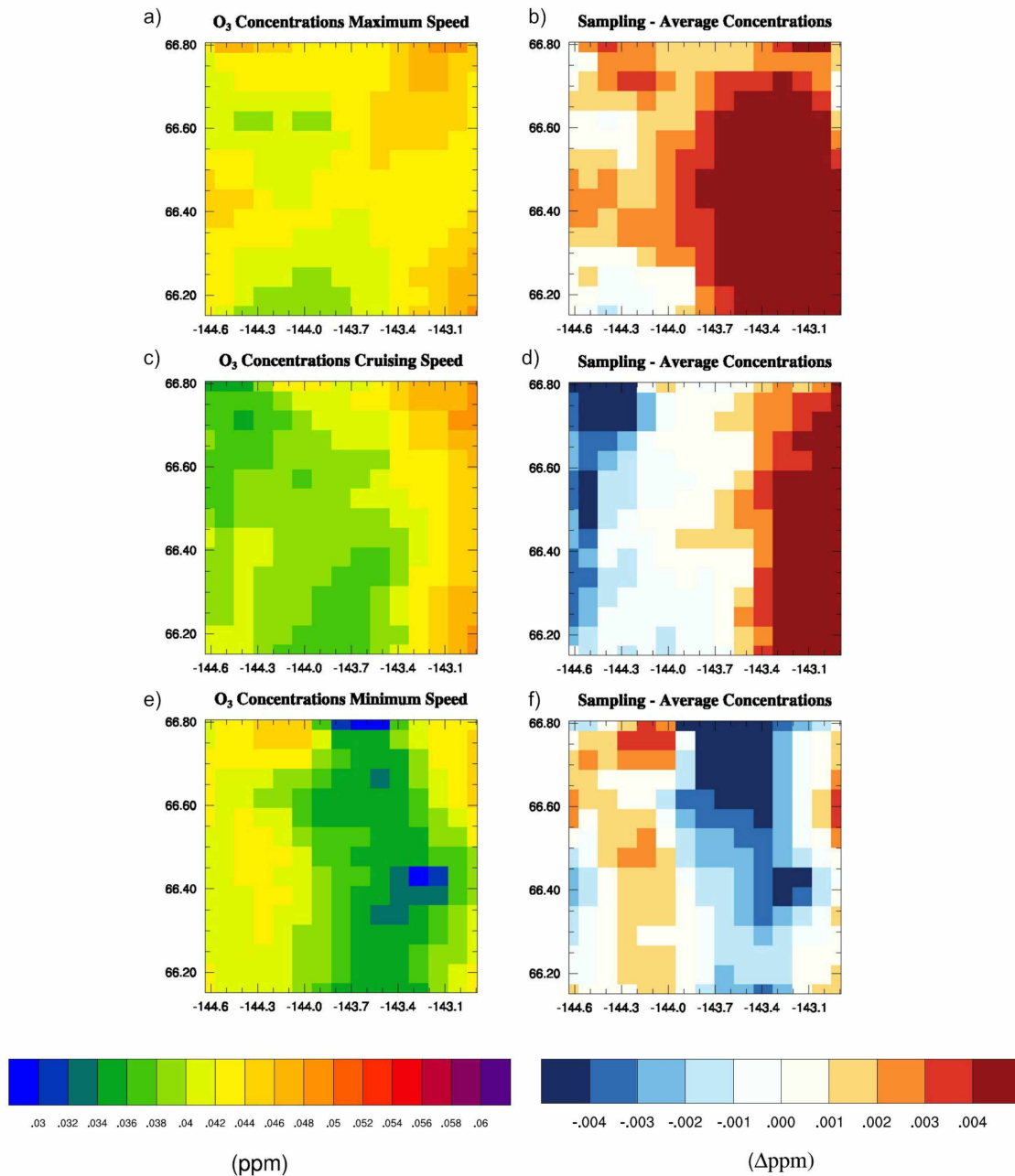
Particulate matter is released from fire by the burning of biomass. Particulate matter can also be created by reactions from gases (gas-to-particle conversion). Currently, the NAAQS for PM_{10} is 150 $\mu g/m^3$ for a 24-hour period. For $PM_{2.5,}$ which is included into PM_{10} the NAAQS is 35 $\mu g/m^3$ in a 24-hour period. The annual mean and 24 hour mean $PM_{2.5}$ concentrations for Fairbanks were 11.2 and 44.3 $\mu g/m^3$ in 2008, respectively. Higher concentrations of PM lower visibility and reduce the air quality (Porter, 2009; Mölders et al., 2010; 2013).

4.3.1 PM_{10}

For this study, the 20 hour average and maximum concentrations of PM_{10} are higher at low altitude than at the top of the ABL. However, there were instances, when concentrations at 1000 m were higher than those close to the ground. This exception from the general picture was most evident on 7 August. Then the maximum PM_{10} concentration was 71.9 $\mu g/m^3$ at 1000 m and 6.23 $\mu g/m^3$ at 200 m, but these peak values were missed by the UAV sampling because PM_{10} concentrations are very variable in time.

In Figure 4.18, the sampled PM_{10} concentrations at the 200 m, 500 m, and 1000 m height are shown for 7 August. Despite the overall trend, when the UAV sampled the concentrations it found the highest concentrations in the lowest level. It is important to note that the UAV sampled concentrations were within the NAAQS, as the cold front had passed through the previous day washing out the PM_{10} from the atmosphere.
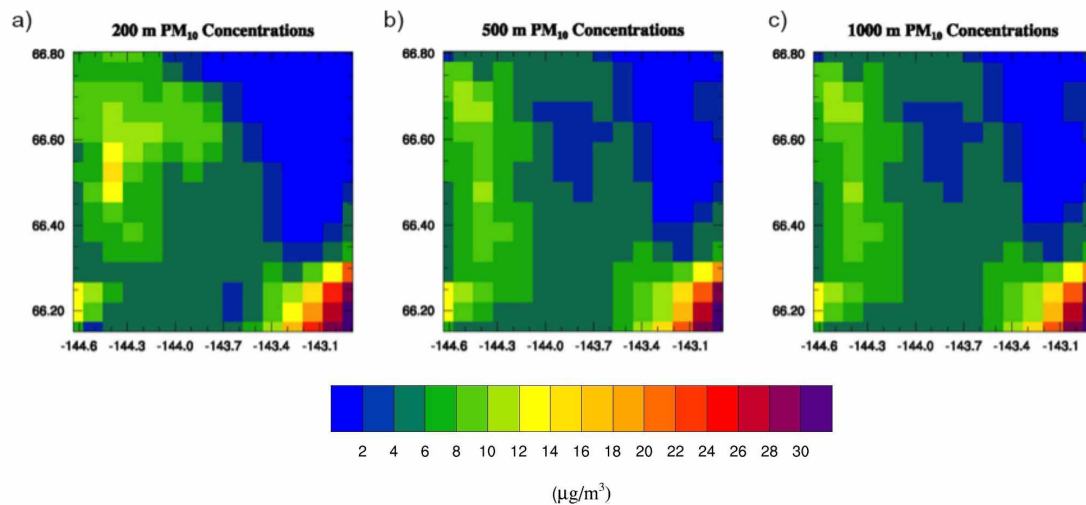
Figure 4.18 PM_{10} concentrations ($\mu g/m^3$) at varying heights. 200 m (a), 500 m (b), and 1000 m (c) heights for 7 August. The UAV did not pick up on higher concentrations at the 1000 m height due to timing of the passage of the UAV.

4.3.1.1 Sampling Height

The large differences in PM_{10} concentration with height mostly occurred for the maximum and minimum values over the whole sampling domain. There was less variation between hours that have PM_{10} concentrations close to the 20 hour average PM_{10} concentrations. Based on the little variability that occurs between individual hours that have PM_{10} concentrations close to the 20 hour average values, it is reasonable to use the 200 m height for the UAV flights since it is not practical to fly higher in altitude to identify the locations of extreme conditions.

Sampling at a level that has the highest concentrations is not always necessary or worth the expense and time (especially if the highest concentrations are typically at lower altitudes). Because PM becomes an issue with breathing as well as ground visibility, it would be more useful to have a distribution of mean concentrations at lower levels. In addition, due to the settling of PM_{10}, PM_{10} from above will eventually reach this lower level,

107

and monitoring only the lowest level would save in time and money especially when sampling multiple chemical species with different UAVs (Figure 4.19). It is important to remember that flying with multiple instruments on a UAV can create a payload that is too large for the UAV to carry.

Due to the passing of the cold front on 6 August, large differences existed between the first HOFP and the second HOFP. The highest PM_{10} concentrations were recorded prior to the passing of the front. On this day, a low-pressure system centered over the Interior produced scattered rain showers. These showers scavenged particles, which lowered the PM_{10} concentrations in the UAV sampling domain. Despite the decrease in PM_{10} concentrations, the maximum concentration of PM_{10} during the first HOFP was 1021.3 µg/m³. According to the WRF/Chem data ('grand truth'), the maximum PM_{10} concentration, however, was 323.0 µg/m³. The minimum PM_{10} values sampled were close to the lowest possible value being about 0.3 µg/m³ which would be considered background concentrations. Consequently, on 7 August, one finds little overall differences between the 20 hour distributions obtained for the different heights as most PM_{10} is washed out after the passing of the front and hence concentrations are below the NAAQS.
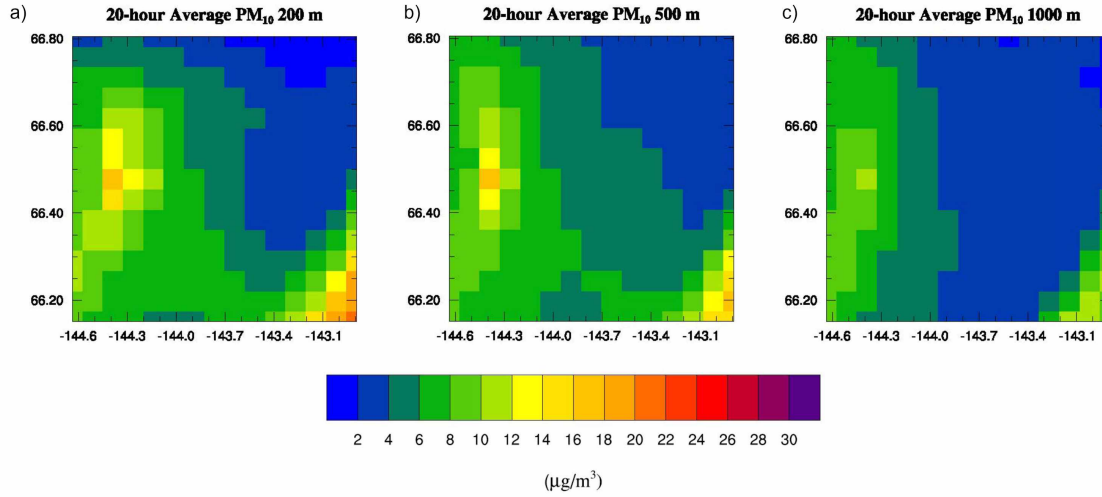
Figure 4.19 20 hour average concentrations (µg/m³) of PM$_{10}$ on 7 August at the 200 m, a) 500 m, b) 1000 m, c) heights. All concentrations are below the NAAQS, as were the concentrations that were observed by the UAV for all days after the cold front.

While the precipitation amounts for the second HOFP were considerably lower than for the first HOFP, the UAV did not pick up on some of the higher concentrations due to the timing of the flight (Figure 4.20). The mean PM$_{10}$ distribution obtained when sampling on 6 August produced a total RMSE of 360.1 µg/m³. The other days experienced overall considerably lower concentrations of PM$_{10}$ due to the washout/rainout processes that occurred earlier in the episode. Subsequently, the absolute errors were much smaller when compared to the 20 hour average of the 'grand truth' than for the days earlier in the episode when concentrations were high.

When determining the relative errors, one has to conclude that PM concentrations recorded by the UAV are very dependent on timing as well as weather conditions. For example, the highest errors occur prior to the passing of the cold front when there was much more variability in the PM$_{10}$ concentrations than later.
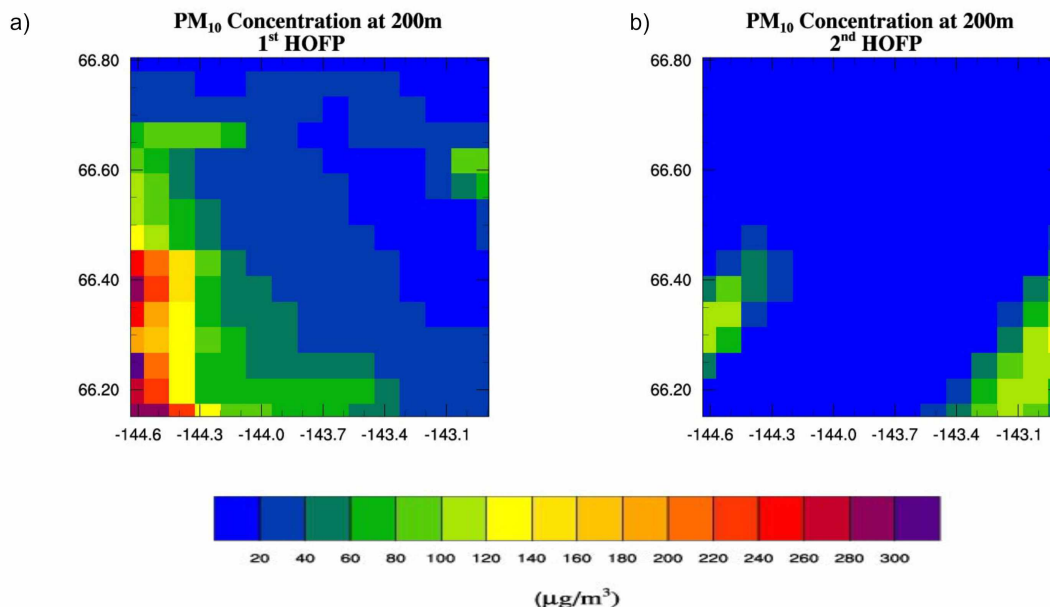
Figure 4.20 First and second HOFP for 6 August 2009 for PM_{10}. a) First HOFP for 6 showing high concentrations where the UAV went over early in the day as well transport to the SW from a NE wind. b) Second HOFP for 6 August, this time occurred during a rain shower which washed out most of the particulate matter leaving only higher concentrations in select areas, slight banding of PM_{10} can be seen, this is caused by the plume being stretched from the NE to SW from the NE wind.

4.3.1.2 Sampling Pattern

The obtained mean distributions of PM_{10} concentrations were much more dependent on the UAV sampling pattern than the meteorological or gaseous quantities, especially in cases with precipitation. As seen in Table 4.11 the errors were higher, and there was much more variation in sampled concentrations. The reasoning for less variation and smaller errors in the third sampling pattern is because the UAV followed the precipitation on 6 August and had lower concentrations making the difference smaller between the sampled and 'grand truth' concentrations. Overall, the differences between sampled and 'grand truth' PM_{10} concentrations had little reoccurring patterns of where high and low concentrations were located based on sampling patterns (for example, 7 August in Figure 4.21).

Correlations increase with height with the first and second sampling patterns because there is a more even distribution of PM_{10} at these levels.

110

The first and second sampling pattern also does not follow the cold front and precipitation that occurred on 6 August.

Table 4.11 Means and standard deviations, and skill scores of PM_{10} concentration for the various speeds at 200 m, 500 m and 1000 m height determined over the entire episode and sampling. Note that the 1st sampling pattern is the default.

Sampling Pattern	Observed	Sampled	RMSE	SDE	Bias	Correlation
200 m						
1st ($\mu g/m^3$)	21.6±30	25.3±39	42.6	37.2	0.1	0.7
2nd ($\mu g/m^3$)	21.6±30	27.6±53	45.9	35.9	-0.1	0.7
3rd ($\mu g/m^3$)	21.6±30	22.0±27	17.1	11.4	-0.2	0.7
500 m						
1st ($\mu g/m^3$)	21.0±47	24±45	32.7	54.7	0.3	0.9
2nd ($\mu g/m^3$)	21.0±47	22±67	36.5	61.7	0.2	0.9
3rd ($\mu g/m^3$)	21.0±47	30.7±34	21.8	48.4	-0.2	0.7
1000 m						
1st ($\mu g/m^3$)	17.0±78	18±104	17.2	29.1	0.2	0.9
2nd ($\mu g/m^3$)	17.0±78	19±98	24.9	38.6	0.3	0.9
3rd ($\mu g/m^3$)	17.0±78	24.9±76	20.7	8.0	-0.3	0.3
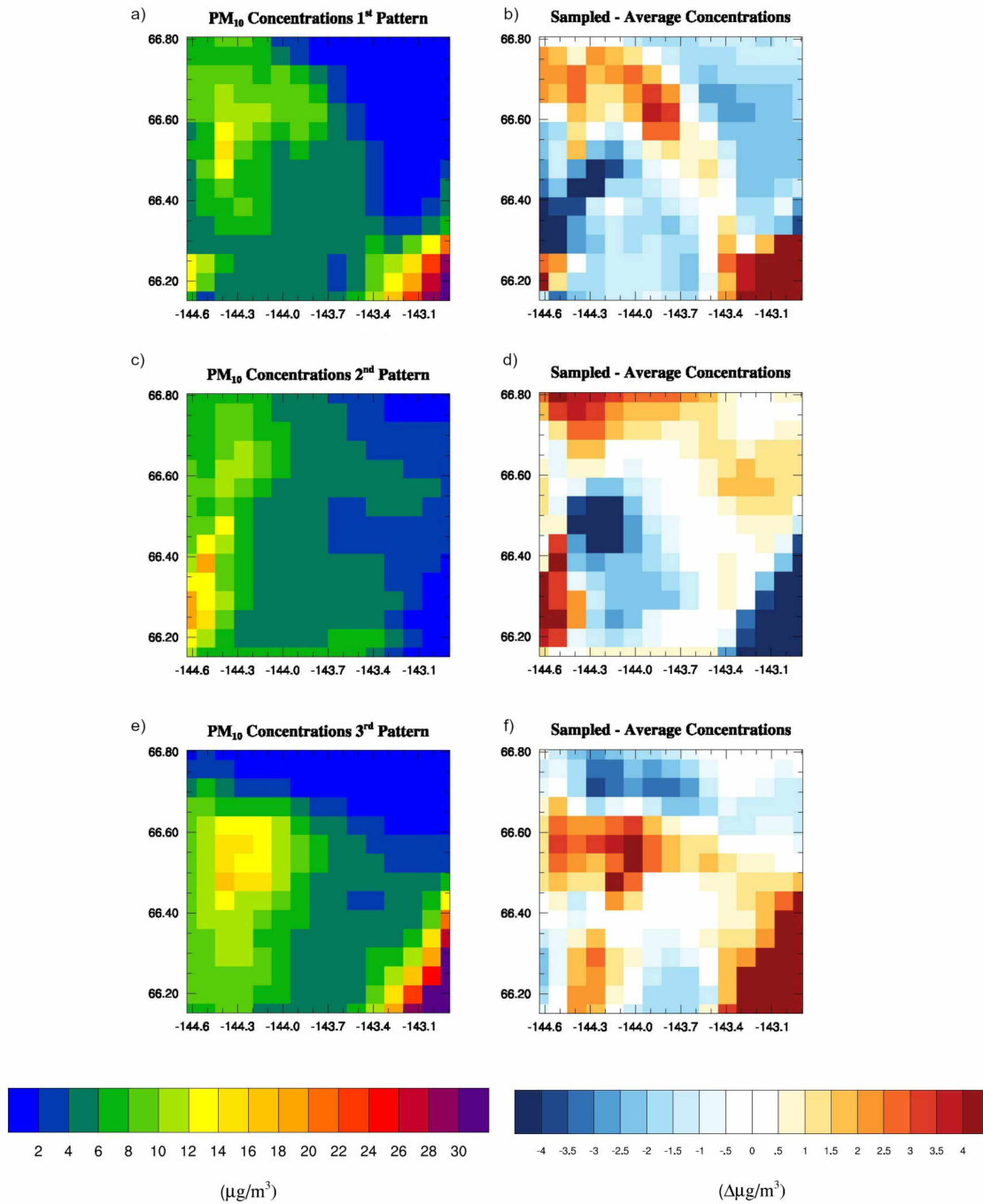
Figure 4.21 Average sampled concentrations of PM_{10} in µg/m³ on 7 August with varying directions. a-b) Concentrations obtained by the 1st sampling pattern and the difference between sampled concentrations and the 'grand truth' values. c-d) Concentrations obtained by the 2nd sampling pattern and the respective difference. e-f) Concentrations obtained by the 3rd sampling pattern concentrations and its difference values. The 'grand truth' can be seen in Figure 4.19.
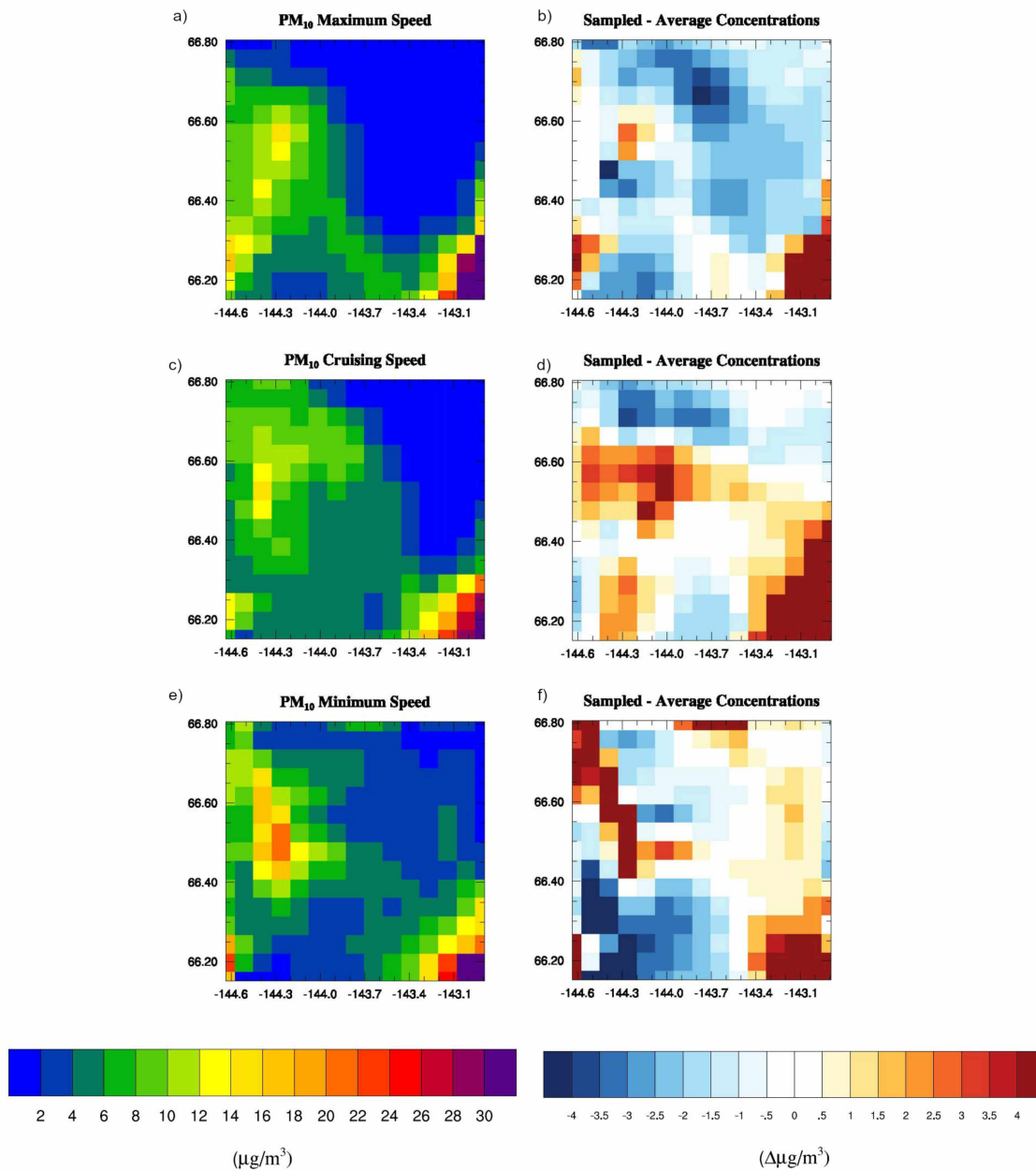
4.3.1.3 Sampling Speed

When the UAV was traveling at its maximum speed, it was able to record higher PM_{10} concentrations than it was able to capture when traveling at cruising speed or at its minimum speed. This behavior was especially true for 6 August, the day of the passing of the cold front because it stayed in front of the front at the maximum speed.

Due to the enhanced speed of the UAV, all of the first HOFP and the majority of the second HOFP were sampled prior to the washout of the PM_{10}. Whereas with minimum speed the highest concentrations may have been missed because the UAV sampled PM_{10} concentrations after scavenging.

Slight differences were found between the 20 hour mean PM_{10} concentration distributions gained when the UAV was travelling at its cruising speed and when it was travelling at its minimum speed. These differences can be mainly attributed to the location of high PM_{10} concentrations and not the concentrations themselves. When comparing the 20 hour PM_{10} concentration distributions obtained from the UAV flight at minimum speed to the 20 hour average derived from the WRF/Chem data ('grand truth'), the plume dispersion is distorted.

Unlike the varying sampling patterns when the UAV travelled at different speeds the differences between the 20 hour mean values calculated from the sampled data and the 'grand truth' had similar spatial structures; meaning that in areas where 20 hour mean concentrations were underestimated for one speed they were underestimated for all, just with varying magnitudes (Figure 4.22).

Due to the temporal and spatial variability of PM_{10} it would be most reasonable to take samples at the lowest altitude, and at the UAV cruising speed. When determining the sampling pattern it is critical to take into account the meteorological conditions such as wind speed/direction as well as precipitation. Especially when the intent is to document the severity of the polluted situation.

114

Figure 4.22 Average sampled concentrations of PM_{10} in µg/m³ on 7 August with varying speeds. a-b) Concentrations obtained by the maximum sampling speed and the difference between concentrations and the 'grand truth' values. c-d) Concentrations obtained by the cruising speed and the respective difference. e-f) Concentrations obtained by the stall speed and its difference values. The 'grand truth' can be seen in Figure 4.19.

115

4.3.2 PM$_{2.5}$

Looking at the 20 hour mean distributions of the 'grand truth', like for PM$_{10}$, PM$_{2.5}$ concentrations vary with height, where higher AGL heights have the highest concentrations which can be seen by the large variation in 'grand truth' PM$_{2.5}$ concentrations in Table 4.12. For the majority of the episode between 6 August and 10 August, the maximum PM$_{2.5}$ concentrations were occurring at the 200 m level (Figure 4.23). Although the sampled concentrations are higher at the 500 m and 1000 m height the range of concentrations is higher at these levels. Meaning that the concentrations are more variable, whereas at the 200 m height the concentrations are more uniform.

Table 4.12 Means and standard deviations, and skill scores of PM$_{2.5}$ concentration for the various speeds at 200 m, 500 m and 1000 m height determined over the entire episode and sampling. Note that the 1st sampling pattern is the default.

Flight Altitude	Grand Truth	Sampled	RMSE	SDE	Bias	Correlation
200 m (μg/m^3)	9.4±9	9.9±15	6.2	6.7	0.1	0.3
500 m (μg/m^3)	10.2±9	12.1±27	8.3	12.8	0.1	0.5
1000 m (μg/m^3)	9.4±38	16±21	12.4	13.0	0.3	0.9

8 August, had the greatest differences in 20 hour mean PM$_{2.5}$ concentrations at different heights with a difference of 9 μg/m^3 between the 1000 m and 200 m heights.

When hours containing minimum values were examined, the 200 m height had lower 20 hour mean PM$_{2.5}$ concentrations compared to the 500 m and 1000 m heights. When looking at hours containing PM$_{2.5}$ concentrations

116

around the 20 hour average value, there was one day where all heights had similar $PM_{2.5}$ concentrations throughout the day, meaning that there was a well-mixed ABL. There were two days with higher $PM_{2.5}$ concentrations at the 500 m height, and two days with the highest concentrations being at 200 m.

On 6 and 7 August, the 500 m height had highest 20 hour mean $PM_{2.5}$ concentration, but lower overall concentrations when compared to concentrations sampled at different heights, followed by 1000 m and 200 m with the lowest 20 hour mean $PM_{2.5}$ concentrations. During this time, there were light rain showers simulated in Circle, AK with the highest cloud ceilings occurring at 250 m. The most efficient washout occurred below 500 m where precipitation was present, whereas at elevations above 500 m, some of the $PM_{2.5}$ likely served as cloud condensation nuclei (CCN), thereby contributing to the decrease in $PM_{2.5}$ concentrations besides rainout. This was not seen in the PM_{10} data because as $PM_{2.5}$ swells it may shift into the PM_{10} class.
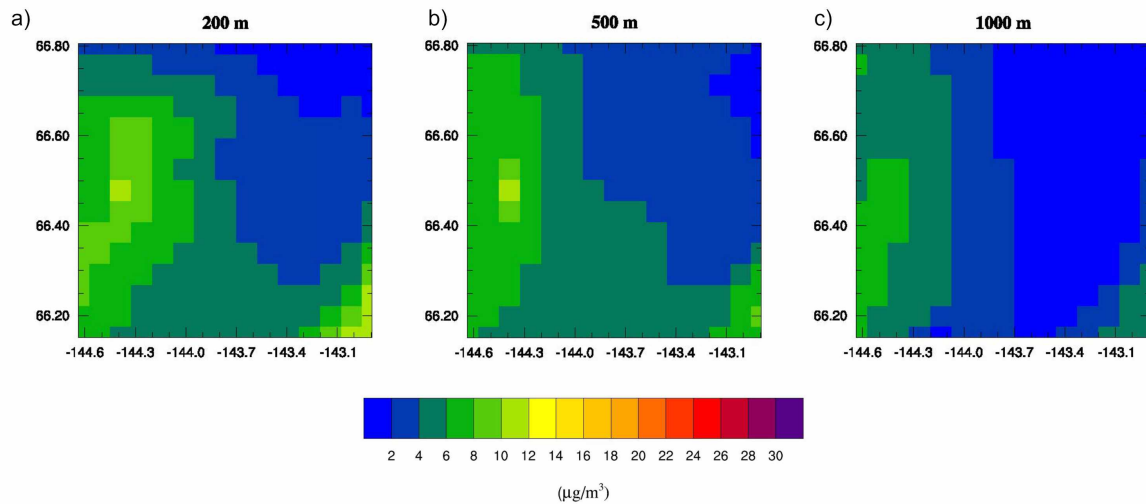
Figure 4.23: 20 hour average $PM_{2.5}$ concentrations at the a) 200 m, b) 500 m, and c) 1000 m heights on 7 August.

4.3.2.1 Sampling Height

The 200 m height was used for the detailed discussion of the 20 hour mean $PM_{2.5}$ concentrations derived from the UAV sampling. This height was chosen because under quiescent conditions the highest $PM_{2.5}$ concentrations were located at this level. Thus, discrepancies become more obvious than at the other levels.

During the episode of this study, the second HOFPs have higher $PM_{2.5}$ concentrations with a total percent increase of 1057% over the first two days with this sampling pattern.

As mentioned before, starting on 6 August, $PM_{2.5}$ concentrations decreased due to the passing of a cold front resulting in over 50% of the UAV sampling domain being below the NAAQS of 35 μg/m^3. Overall, the 20 hour mean $PM_{2.5}$ concentration distributions derived from the UAV records for $PM_{2.5}$ followed that of the PM_{10} throughout the entire episode of this study at the 200 m height.

Throughout the episode the greatest variability between the 20 hour mean derived from the sampled $PM_{2.5}$ concentrations and the 20 hour average from the 'grand truth' occurred at the 200 m level, due to the marginal dispersion of the plume in the horizontal direction at this level (Figure 4.24). At higher altitudes, the plume has expanded and created a more uniform distribution of $PM_{2.5}$ concentrations, and as a result the differences between the 'grand truth' and the sampled concentrations are smaller at these levels (Figure 4.24).
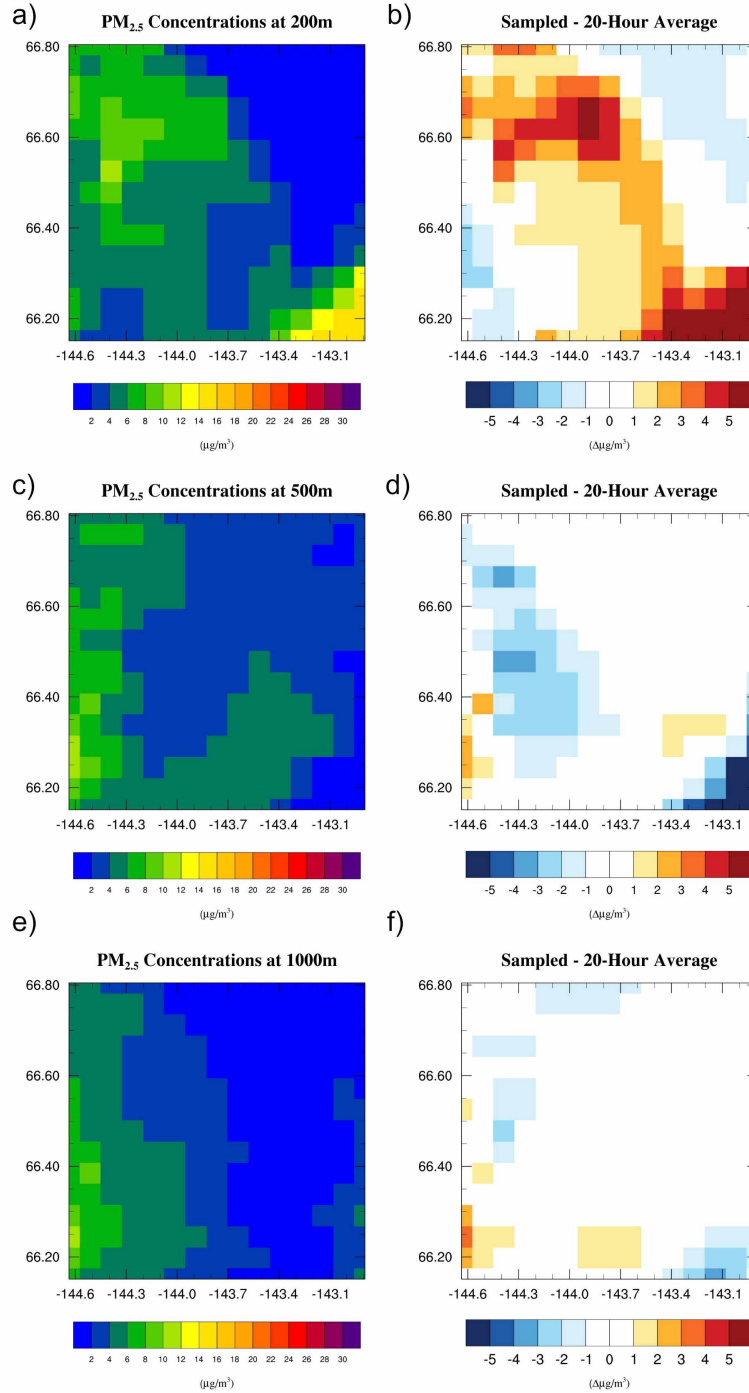
Figure 4.24 Average sampled concentrations of $PM_{2.5}$ in μg/m³ on 7 August with varying heights. a-b) Concentrations obtained by the 1st sampling pattern and the difference between sampled concentration and the 'grand truth' values. c-d) Concentrations obtained by the 2nd sampling pattern and the respective difference. e-f) Concentrations obtained by the 3rd sampling pattern and its difference values. The 'grand truth' can be seen in Figure 4.23a.
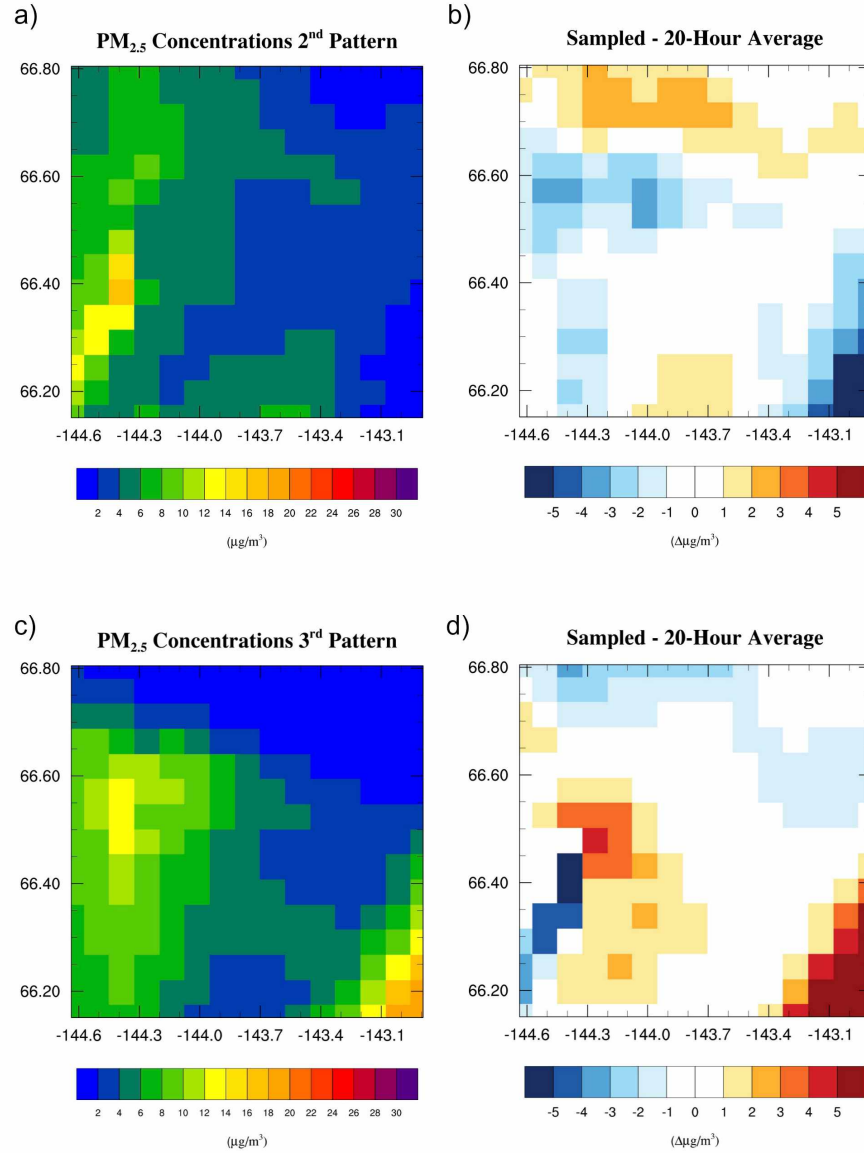
4.3.2.2 Sampling Pattern

The 20 hour average $PM_{2.5}$ concentrations from the WRF/Chem ('grand truth') were lower concentrations than those obtained by the sampling along the three UAV sampling patterns. These differences were due to the passing of the aforementioned cold front. The lowest 20 hour average $PM_{2.5}$ concentrations occurred in the northern portion of the UAV domain (Figure 4.25).

The first and second sampling patterns produced similar results to the 20 hour average $PM_{2.5}$ concentration distributions in terms of placement of the highest concentrations (Figures 4.24a, 4.25a). However, the second sampling pattern yielded to slightly higher $PM_{2.5}$ concentrations (over 300 $\mu g/m^3$ compared to 170 $\mu g/m^3$ in first sampling pattern. The third sampling pattern failed to capture these high concentrations in the first HOFP, with a recorded maximum of 100 $\mu g/m^3$. For the second HOFP the recorded $PM_{2.5}$ concentrations were similar in all three sampling patterns, and were closer to the 20 hour average $PM_{2.5}$ concentrations ('grand truth', Figure 4.25).

The 20 hour average $PM_{2.5}$ concentrations for 8 August showed an area with low, but near uniform $PM_{2.5}$ concentrations. However, the first HOFP for all sampling patterns showed a much more variable environment. Each flight path had an area of low $PM_{2.5}$ concentrations that were slightly above 0 $\mu g/m^3$ (background concentrations) as well as an area with $PM_{2.5}$ concentrations exceeding 16 $\mu g/m^3$, which was contaminated by the plume.

The locations of the 20 hour average low/high concentrations differ for each sampling pattern, and in areas that were in the first quarter of the whole flight. This feature suggests that the varying 20 hour average $PM_{2.5}$ concentration distribution was a product of timing and vertical mixing rather than any horizontal transport of $PM_{2.5}$. Note that the emissions are constant over the entire time. The $PM_{2.5}$ concentrations sampled on the second HOFPs were near uniform and closely matched the 20 hour average concentrations derived from the 'grand truth'. The first sampling pattern produced slightly

120

lower 20 hour $PM_{2.5}$ concentrations (a difference of 2 µg/m³) than what should be found according the 20 hour average of the WRF/Chem ('grand truth') data.

Figure 4.25 Average sampled concentrations of $PM_{2.5}$ in µg/m³ on 7 August. a-b) Concentrations obtained by the 2nd sampling pattern and the difference between sampled concentrations and the 'grand truth' values. c-d) Concentrations obtained by the 3rd sampling pattern and the respective difference. The first sampling pattern and its difference from the 'grand truth' can be seen in Figure 4.24a), b).

4.3.2.2 Sampling Speed

The greatest differences throughout the sampling domain between the 20 hour average from the UAV records and the 20 hour average 'grand truth' of WRF/Chem occurred when the UAV was travelling at its slowest speed (Figure 4.26c,d)

When the UAV travelled at its cruising speed or its maximum speed the difference between the 20 hour average and the 20 hour average concentrations derived from the UAV sampling showed more spatial variability than that obtained when sampling at the minimum speed. Independent of speed, the UAV derived 20 hour average concentrations generally underestimated the 20 hour $PM_{2.5}$ concentrations of the 'grand truth' (Figure 4.26a, b)

Average biases ranged from 2 to 66% for both the FB and the NMB, respectively. The lowest biases occurred when the UAV was travelling at its maximum speed with an average FB of 2% and an average NMB of -21%. In regards to the minimum speed, the average FB was -66% and the average NMB was -48%.
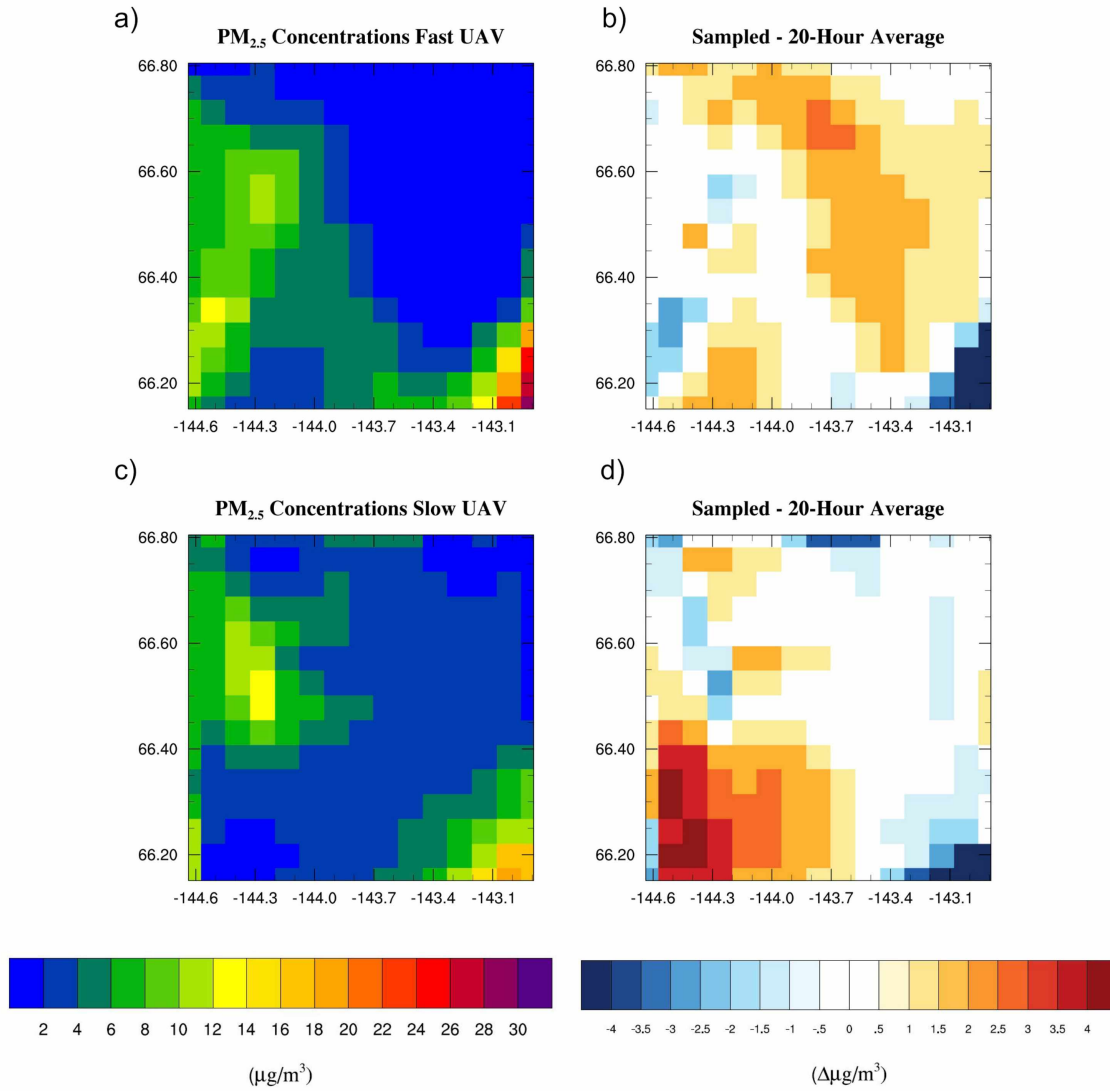
Figure 4.26 Average sampled concentrations of $PM_{2.5}$ in µg/m³ on 7 August with varying speeds. a)-b) Concentrations obtained by the maximum sampling speed and the difference between sampled concentrations and the 'grand truth' values. c)-d) Concentrations obtained by the minimum sampling speed and the respective difference. The cruising sampling speed and its difference from the 'grand truth' can be seen in Figure 4.24a, b. The 'grand truth' values are shown in Figure 4.23a.

4.3.3 Comparison of $PM_{2.5}$ and PM_{10}

Comparing the sampling of $PM_{2.5}$ and PM_{10} is important because not only is $PM_{2.5}$ included in PM_{10} but also because PM often undergoes stratification in the atmosphere, with typical highest concentrations at the lowest levels.

For both $PM_{2.5}$ and PM_{10}, there were times where concentrations were decreasing with an increase with height. There were only four exceptions where the concentration increased with height. The concentration differences between $PM_{2.5}$ and PM_{10} were consistently around 0.1 μg/m^3 (i.e. about the order of magnitude of current state-of-the-art measurement accuracy). Because PM_{10} includes $PM_{2.5}$ all of the average concentrations for 20 hour periods were higher for PM_{10} than $PM_{2.5}$ at all three heights AGL.

The difference was taken to determine the concentrations of particulate matter between the diameter 2.5 to 10 μm. The difference between the PM_{10} and $PM_{2.5}$ concentrations for all days was less than that of $PM_{2.5}$. This finding means that in the ABL most of the particulate matter was $PM_{2.5}$, which causes health issues as it can travel into the lungs.

4.3.3.1 Comparison of $PM_{2.5}$ and PM_{10}: Sampling Pattern

When the sampling pattern was changed, the concentrations of $PM_{2.5}$ and PM_{10} were positively correlated with the placement of high and low concentrations in the same spots. There was no instance where there were high concentrations of one size particulate matter and low for the other size at a particular point.

4.3.3.2 Comparison of $PM_{2.5}$ and PM_{10}: Sampling Speed

Similar to the different sampling pattern, changes in UAV speed yielded high and low concentrations of $PM_{2.5}$ and PM_{10} that were positively correlated with regards to spatial distribution. The concentrations of PM_{10}

were higher than that of $PM_{2.5}$ with increasing speed, as expected because $PM_{2.5}$ is a fraction of the PM_{10}.

Chapter 5
Conclusions

The Crazy Mountain Complex of fires occurred in northern Interior Alaska and consisted of four fires that started on 20 June 2009 and lasted until 31 August 2009. These fires affected the community of Circle, Alaska as well as vehicular traffic along the Steese Highway. It resulted in temporary flight restrictions near the plumes of these fires (AICC, 2009).

The majority of the smoke from these fires was contained within the ABL. With this containment to the ABL, the Crazy Mountain Complex fires is a good test case for theoretical analysis of how UAV could be used to assess the daily mean concentration distributions of various contaminants emitted by fires.

During the fire, the University of Alaska Fairbanks Geophysical Institute's ACUASI team conducted multiple flights into the Crazy Mountain Complex fires with the ScanEagle. The ScanEagle was equipped with an infrared (IR) camera that was used to determine the edge of the fires (ACUASI, 2015b). The IR monitoring of the fire by the UAV flights helped resource management decisions, but data was not collected to assess the chemical composition of the plume and/or the transport of the gases and particulates from the fire emissions.

If equipped with chemical and meteorological monitoring equipment, UAVs can monitor within wildfire plumes where it is too hazardous to monitor using manned aircrafts. Monitoring of meteorological variables such as temperature and dewpoint temperature would be beneficial in forecasting the spread of fires and the vertical transport due to buoyancy. While wind direction and speed would also be extremely beneficial for determining how a fire would spread, the payload weight restrictions on the ScanEagle deem it impossible to have meteorology/chemistry and wind instruments aboard the aircraft at the same time (INSITU, 2014). Furthermore, any wind

127

measurements require an inertial platform. However, a UAV cannot be considered as such.

Wind in Interior Alaska is typically light and variable, especially in the ABL, so it would be more beneficial for the other variables to be measured instead.

Data from a WRF/Chem simulation performed for the most active time of the Crazy Mountain fires served as a 'grand truth'. These data were assumed to represent atmospheric conditions during the wildfire. An evaluation by means of surface meteorological and particulate matter data as well as CALIPSO, METAR report and MODIS data demonstrated that the WRF/Chem simulations provided a realistic dataset of a wildfire situation.

Three different UAV sampling patterns were designed. Along these patterns various meteorological and chemical quantities were sampled from the WRF/Chem data that was assumed to represent the atmospheric conditions during a wildfire ('grand truth'). The sampling was repeated for different heights (200 m, 500 m, 1000 m) as well as at minimum, cruising, and maximum UAV flight speed. Using the sampled data 20 hour averages were constructed and evaluated against the 20 hour averages determined directly from the model output produced by WRF/Chem. Differences in the mean distributions obtained by sampling were analyzed with respect to the different sampling methods as well as the mean distribution of the WRF/Chem 'grand truth'.

This study is beneficial to furthering the use of UAVs for studying of atmospheric physical and chemical conditions because it can help determine which heights, patterns, and speeds the UAV should travel at with certain synoptic conditions. Knowing these parameters ahead of time is useful when planning field campaigns, as it would not only save time, but also money given that it would cut back on flights with less representative data. Considering the level at which the UAV should fly is crucial, since meteorological and chemical properties vary in the vertical.

In the case of the Crazy Mountain Complex, the majority of the plume was contained within the ABL (0 to 1000 m AGL). Above 1000 m, concentrations of all chemical species were close to the background conditions, i.e. only marginal, if at all affected by the fires. For example, at 3 km only extremely high concentrations in areas of high upward velocity occurred in the WRF/Chem data, and by 5 km there was no sign of a fire according to WRF/Chem output.

Flying the UAV at the lowest altitude possible that provides a good grasp of the plume extension, composition and contaminant concentrations not only allows for the maximum concentrations to be recorded but would also save time and money in a field experiment.

When the assumed UAV sampled at various heights, the differences in meteorological quantities were due to the environmental temperature lapse rate and the dewpoint temperature lapse rate. Concentrations of gases were nearly uniform with height due to the strong mixing within the ABL when comparing the 200 m, 500 m, and 1000 m levels. PM concentrations varied the most when comparing concentrations at various altitudes, but the sampling could not reveal any stratification of $PM_{2.5}$ and PM_{10} between the three height levels examined in this study. As a result, one may conclude that the lowest flight level can be chosen as a good representation of the conditions within the ABL during a fire event of similar characteristics than the Crazy Mountain Complex fires.

Changes in sampling pattern yielded greater differences in the mean distributions derived from the measured variables than changing the flight level. When considering the meteorological conditions the diurnal cycle as well as an approaching weather system may affect the derived mean distribution. Thus, when the large-scale synoptic situation suggests the approach of a frontal system, the sampling pattern has to be carefully chosen with the intended use of the data in mind. Mean distributions may differ notably when the sampling occurs prior to or after the frontal passage. In

interpretation of mean distributions frontal approaches and the impacts of the diurnal cycle are hard to distinguish. Considering the diurnal cycle is also imperative in the interpretation of gases that undergo photochemical reactions.

Similar problems arise when changing the speed of the UAV. At maximum speed, details of the fire-plume composition and extremes can be missed. It was not until the second HOFP that impacts photochemical reactions could be seen in the sampled data in the case of photochemically affected species (NO, O_3). If the sampling domain was smaller than what was used in this study, the decrease or increase of chemical species could be missed entirely.

At minimum speed, changes from photochemical reactions are clearly seen, but it is at the cost of recording features in the fire plume that exist for shorter periods of time. Thus, one has to conclude that one can either optimize the flight speed to capture differences due to photochemical reactions or to capture the heterogeneity of the concentrations in the plume.

The overall meteorological conditions in the fire area are important to assess when choosing a sampling pattern as they can have great impacts on mean concentrations determined from the sampled data. Note that the meteorological conditions also strongly impact the fire conditions and spread (Foster, 1983).

For accurate average concentrations within wildfire plumes, it is best to have the UAV fly when the sampling domain has been synoptically quiescent. As fronts pass through a region the atmosphere undergoes washout and rainout processes. It takes multiple days for concentrations to build back up to the levels prior to the frontal passage. If fronts go through, noting the levels and thickness of clouds is important to determine the levels at which the atmospheric pollutants were washed/rained out.

In summary, sampling should be done at the lowest altitude possible since the most comprehensive dataset can be gathered this way. In regards to

the sampling pattern, it is imperative that meteorological conditions such as wind and precipitation are considered in planning of the flight so any increases/decreases in concentrations can be accounted for. The sampling pattern can create biases of high/low concentrations of chemical species that photochemically react so timing must be considered. Similarly, when a UAV flies at various speeds, biases can be present purely due to the timing of when the UAV goes over an area. To assist in decreasing biases it would be beneficial to employ the use of air quality models such as WRF/Chem to forecast where the highest concentrations of pollutants will be and how they will be advected throughout the atmosphere.

Deciding on the best speed and pattern is dependent on the goals of the research. For an overall study, I would suggest flying a UAV at its cruising speed as it is not only practical in terms of costs but also gives a good representative picture of the concentrations throughout the day. I would recommend multiple flights if possible with varying patterns in order to cover different areas at the same time every day, therefore limiting biases created by timing.

Regardless of flight pattern, speed, or altitude it is crucial that the instrumentation aboard a UAV is capable of recording meteorological and chemical conditions within a fire plume. For temperature and dewpoint temperature it is recommended that instrumentation accuracy is within 2°C, as this is the acceptable residual error in thermocouples used for meteorological measurements (Brock and Richardson, 2001). Also since sampling would be used in the warm season in scenarios that are not extremely temperature sensitive (i.e. not dealing with the freezing/melting point of water).

Instrumentation to monitor concentrations of gaseous species currently has the capability to monitor concentrations in parts per billion (Campbell Scientific, 2015). It would be best for this accuracy to be present on

instruments developed for UAVs, allowing for a maximum of 10 ppb in variance.

In regards to particulate matter instrumentation, measurements are often based off of an intake flow rate that in L/min (Chow and Watson, 1998). Because of the velocity of the UAV it would be recommended to have a low inflow velocity. Accuracy should be within 5 $\mu g/m^3$. With all quantities it would be ideal if continuous measuring was available. However, measurements taken at most every hour would allow for a general picture of the environment to be developed.

Based off of the results from this thesis, the most accurate sampling of the environment would occur at the 200 m height and at cruising speed. In terms of sampling direction it is important to take into account the weather conditions, and if the chemical species undergoes photochemical reactions.

Generally, wildfires occur in a relatively localized area and have the potential to last several months, especially in the northern latitudes. It is easier to plan the exact details (location, times of flights, etc.) of a field campaign in advance than with other spatially and temporally isolated meteorological events. The ability to plan a UAV field campaign in advance is favorable, especially in the United States where getting the waiver to fly a UAV in an area can take an extended period of time (FAA, 2015).

Overall, the use of UAVs would be beneficial in monitoring conditions over a wildfire as well as understanding the local effects of the emissions on air quality and visibility. Knowing the chemical composition of the plume would aid in the understanding the threat for downwind communities and the potential changes in downwind ecosystems after the fire, as the soil and water chemistry change both at the fire location as well as downwind of the event.

References

Ackermann, I. J., H. Hass, M. Memmesheimer, C. Ziegenbein, and A. Ebel, 1995: The parameterization of the sulfate-nitrate-ammonia aerosol system in the long-range transport model EURAD. *Meteor. and Atmos. Phys.*, **57**, 101-114.

Ackermann, I. J., H. Hass, M. Memmesheimer, A. Ebel, F. S. Binkowski, and U. Shankar, 1998: Modal aerosol dynamics model for Europe: development and first applications. *Atmos. Environ.*, **32**, 2981-2999.

ACUASI, a) cited 2015: RxCADRE, Florida, USA. [Available online athttp://acuasi.alaska.edu/content/rxcadre-florida-usa]

ACUASI, b) cited 2015: Unmanned aircraft map northern fires. [Available online at http://acuasi.alaska.edu/media/press-releases/unmanned-aircraft-map-norrthern-fires]

Alaska Department of Natural Resources, retrieved data 2009: Burning in Alaska. [Available online at http://www.atmos-chem-phys.net/7/4043/2007/acp-7-4043-2007.pdf]

Alaska Interagency Coordination Center (AICC), retrieved date 2009: Alaska fire season. 2009 [Available online athttp://fire.ak.blm.gov/content/aicc/stats/archive/2009.pdf]

Alaska Public Lands Information Centers, retrieved date 2014: Fires in Alaska. [Available online at http://alaskacenters.gov/fires-in-alaska.cfm]

Amiro, B., J. I. MacPherson, and R. L. Desjardins, 1999: BOREAS flight measurements of forest-fire effects on carbon dioxide and energy fluxes. *Agric. For. Meteorol.*, **96**, 199–208.

Andreae, M. O., and P. Merlet, 2001: Emission of trace gases and aerosols from biomass burning. *Global Biogeochem. Cycles*, **15**, 955–966.

Avissar, R. and R. A. Pielke, 1989: A parameterization of heterogeneous land surface for atmospheric numerical models and its impact on regional meteorology. *Mon. Wea. Rev.*, **117**, 2113-2136.

Backer, D. M., S. E. Jensen, and G. R. McPherson, 2004: Impacts of fire-suppression activities on natural communities. *Conserv. Biol.*, **18**, 937–946.

Barnard, J. C., J. D. Fast, G. Paredes-Miranda, W. P. Arnott, and A. Laskin, 2010: Technical note: Evaluation of WRF-Chem "aerosol chemical to aerosol optical properties" module using data from MILAGRO campaign. *Atmos. Chem. Phys.*, **10**, 7325-7340.

Bieniek, P. A., 2007: Climate and predictability of Alaska wildfires. M.S. Thesis, Dept. of Atmospheric Sciences, University of Alaska Fairbanks, Fairbanks, AK USA, 92 pp.

Bieniek, P. A., U. S. Bhatt, R. L Thoman, H. Angeloff, J. Partain, J. Papneau, F. Fritsch, E. Holloway, J. E. Walsh, C. Daly, M. Shulski, G. Hufford, D. F. Hill, S. Calos, and R. Gens, 2011: Climate divisions for Alaska based on objective methods. *J. Meteorl. and Climotol.*, **51**, 1276-1289.

Bieniek, P. A., J. E. Walsh, R. L. Thoman, and U. S. Bhatt, 2014: Using climate divisions to analyze variations and trends in Alaska temperature and precipitation. *J. Climate*, **27**, 2800-2818.

Binkowski, F. S. and U. Shankar, 1995: The regional particulate matter model: 1. model description and preliminary results. *J. Geophys. Res.*, **100D12**, 26191–26209.

Bowman, D. M. J. S., and F. H. Johnston, 2005: Wildfire smoke, fire management, and human health. *Eco. Health,* **2**, 76-80.

Brock, F. V., and S. Richardson, 2001: *Meteorological measurement systems.* Oxford University Press, New York, NY, USA, 290 pp.

Campbell Scientific, retrieved date 2015: Air quality and pollution. [Available online at https://www.campbellsci.com/air quality#more]

Chang, J. S., F. S. Binkowski, N. L. Seaman, J. N. McHenry, P. J. Samson, W. R. Stockwell, C. J. Walcek, S. Madronich, P. B. Middleton, J. E. Pleim and H. H. Lansford, 1989: The regional acid deposition model and engineering mode. State-of-Science/Technology, Report 4, National Acid Precipitation Assessment Program, Washington, DC. 98 pp.

Chang, J. C., and S. R. Hanna, 2004: Air quality model performance evaluation. *Meteor. Atmos. Phys.*, **87**,167-196.

Chang, J. T., and P. J. Wetzel, 1991: Effects of spatial variations of soil moisture and vegetation on the evolution of a prestorm environment: A numerical case study. *Mon. Wea. Rev.*, **119**, 1368–1390.

134

Chapman, E. G., W. I. Gustafson Jr., R. C. Easter, J. C. Barnard, S. J. Ghan, M. S. Pekour, and J. D. Fast, 2009: Coupling aerosol-cloud-radiative processes in the WRF-Chem model: Investigating the radiative impact of elevated point sources. *Atmos. Chem. Phys.*, **9**, 945–964.

Cheng, W. Y. Y. and W. J. Steenburgh, 2005: Evaluation of surface sensible weather forecasts by the WRF and the Eta Models over the western United States. *Wea. Forecasting*, **20**, 812–821.

Chou, M., and M. J. Suarez, 1994: An efficient thermal infrared radiation parameterization for use in general circulation models. NASA Tech. Memo. 104606, 85 pp.

Chow, J. C., and J. G. Watson, 1998: Guideline on speciated particulate monitoring. *EPA*, 291 pp.

Christian, T. J., B. Kleiss, R. J. Yokelson, R. Holzinger, P. J. Crutzen, W. M. Hao, B. H. Saharjo, and D. E. Ward, 2003: Comprehensive laboratory measurements of biomass-burning emissions: 1. Emissions from Indonesian, African, and other fuels. *J. Geophys. Res.*, **108**, 4719.

Collins, R. L., and C. F. Cahill, 2000: Lidar and aerosol measurements in the planetary boundary layer: results of the Frostfire experiment. *Appl. Phys. Lab, Johns Hopkins University under contract, 807939.* 25 pp.

Damoah, R., N. Spichtinger, C. Forster, P. James, I. Mattis, U. Wandinger, S. Beirle, T. Wagner, and A. Stohl, 2004: Around the world in 17 days - hemispheric-scale transport of forest fire smoke from Russia in May 2003. *Atmos. Chem. Phys.*, **4**, 1311– 1321.

Das, S., R. Ashrit, G. R. Iyengar, S. Mohandas, M. D. Gupta, J. P. George, E. N. Rajagopal, and S. K. Dutta, 2008: Skills of different mesoscale models over Indian region during monsoon season: Forecast errors. *J. Earth Syst. Sci*, **117**, 603-620.

DeBano, L. F., D. G. Neary, and P. F. Folliott, 1998: *Fire effects on ecosystems.* John Wiley & Sons. New York, NY, USA, 333 pp.

Dissing, D., and D. Verbyla, 2003: Spatial patterns of lightning strikes in Interior Alaska and their relations to elevation and vegetation. *Can. J. For. Res.*, **33**, 770–782.

Dugdale, S. J., 2007: An evaluation of imagery from an unmanned aerial vehicle (UAV) for the mapping of intertidal macroalgae on Seal Sands,

Tees Estuary, UK. M.S. Thesis, Durham University, Durham, UK. 145 pp.

EC-JRC/PBL, cited 2014: EUROPA – EDGAR homepage. [Available online at http://edgar.jrc.ec.europa.eu]

Eidsvik, K. J., A. Holstad, I. Lie, and T. Utnes, 2004: A prediction for local wind variations in mountainous terrain. *Boundary Layer Meteor.*, **112**, 557-586.

Elston, J. S., J. Roadman, M. Stachura, B. Argrow, A. Houston, and E. Frew, 2011: The tempest unmanned aircraft system for in situ observations of tornadic supercells: Design and VORTEX2 flight results. *J. F. Robot.*, **28**, 461–483.

Elston, J. S., B. Argrow, M. Stachura, D. Weibel, D. Lawrence, and D. Pope, 2015: Overview of small fixed-wing unmanned aircraft for meteorological sampling. *J. Atmos. Oceanic Technol.*, **32**, 97-115.

Environmental Protection Agency, 2009: Appendix O: CMAQ Model Performance Evaluation for 2001. [Available online at http://www.epa.gov/ttnecas1/regdata/RIAs/Appendix%20O--Model%20Eval.pdf]

Environmental Protection Agency, a) retrieved date 2013: Particulate matter. [Available online at http://www.epa.gov/airquality/particulatematter/basic.html]

Environmental Protection Agency, b) retrieved date 2013: Wildfires. [Available online at http://epa.gov/naturaldisasters/wildfires/index.html]

Environmental Protection Agency, retrieved date 2015: National ambient air quality standards (NAAQS). [Available online at http://www.epa.gov/air/criteria.html]

ESRI Data – Maps, retrieved date 2014: Basemaps. [Available online at http://www.esri.com/data/basemaps]

Ezequiel, C. A. F., M. Cua, N. C. Libatque, G. L. Tangonan, R. Alampay, R. T. Labuguen, C. M. Favila, J. L. E. Honrado, V. Canos, C. Devaney, A. B. Loreto, J. Bacusmo, and B. Palma, 2014: UAV aerial imaging applications for post-disaster assessment, environmental management

and infrastructure development. *2014 Int. Conf. Unmanned Aircr. Syst.*, Orlando, FL, IEEE, 274–283.

FAA, retrieved date 2015: Unmanned aircraft systems (UAS) regulations & policies. [Available online at https://www.faa.gov/uas/regulations_policies/]

Ferguson, S. A., R. L. Collins, J. Ruthford, and M. Fukuda, 2003: Vertical distribution of nighttime smoke following a wildland biomass fire in boreal Alaska. *J. Geophys. Res*, **108**, 4743-4715.

Foster, D. R., 1983: The history and pattern of fire in the boreal forest of southeastern Labrador. *Canadian Journal of Botany*, **61(9)**, 2459-2471.

Freijtas, S. R., K. M. Longo, M. A. F. Silva Dias, and P. Artaxo, 1996: Numerical modeling of air mass trajectories from the biomass burning areas of the Amazon basin. *Ann. Acad. Bras. Sci.*, **68** Supplement 1, 193-206.

Grell, G. A., and D. Dévényi,, 2002: A generalized approach to parameterizing convection combining ensemble and data assimilation techniques. *Geophys. Res. Let.*, **29**, 38-1-38-4.

Grell, G. A., S. E. Peckham, R. Schmitz, S. A. McKeen, G. Frost, W. C. Skamarock, and B. Eder, 2005: Fully coupled "online" chemistry within the WRF model. *Atmos. Environ.*, **39**, 6957-6975.

Grell, G. A., S. R. Freitas, M. Stuefer, and J. Fast, 2011: Inclusion of biomass burning in WRF-Chem: Impact of wildfires on weather forecasts. *Atmos. Chem. Phys.*, **11**, 5289-5303.

Guenther, A., P. Zimmerman, and M. Wildermuth, 1994: Natural volatile organic compound emission rate estimates for U.S. woodland landscapes. *Atmos. Environ.*, **28**, 1197-1210.

Gupta, P., S. A. Christopher, J. Wang, R. Gehrig, Y. Lee, N. Kumar, 2006: Satellite remote sensing of particulate matter and air quality assessment over global cities. *Atmos. Environ.*, **40**, 5880-5892.

Hacker, J. P., and D L. Rife, 2007: A practical approach to sequential estimation of systematic error on near-surface mesoscale grids. *Wea. Forecasting*, **22**, 1257–1273.

Hawbaker, T. J., V. C. Radeloff, A. D. Syphard, Z. Zhu, and S. I. Stewart, 2008: Detection rates of the MODIS active fire product in the United States. *Remote Sens. Environ.*, **112**, 2656–2664.

Heilman, W. E., Y. Liu, S. Urbanski, V. Kovalev, and R. Mickler, 2014: Wildland fire emissions, carbon, and climate: Plume rise, atmospheric transport, and chemistry processes. *For. Ecol. Manag.*, **317**, 70–79.

Hines, K. M., and D. H. Bromwich, 2008: Development and testing of Polar Weather Research and Forecasting (WRF) Model. Part I: Greenland ice sheet meteorology. *Mon. Wea. Rev.*, **136**, 1971–1989.

Hines, K. M., D. H. Bromwich, L. Bai, M. Barlage, and A. G. Slater, 2011: Development and testing of Polar WRF. Part III: Arctic land. *J. Climate*, **24**, 26–48.

Hodzic, A., S. Madronich, B. Bohn, S. Massie, L. Menut, and C. Wiedinmyer, 2007: Wildfire particulate matter in Europe during summer 2003: Meso-scale molding of smoke emissions, transport and radiative effects. *Atmos. Chem. Phys.*, **7**, 4043-4064.

Houghton, J. T., G. J. Jenkins, and J. J. Ephraums, 1990: *Climate change: The IPCC scientific assessment.* Cambridge Univ. Press, New York, 364 pp.

Houghton, J. T., L. G. Meira Filho, B.A. Callander, N. Harris, and A. Kattenberg, 1995: *Climate change 1995: The science of climate change.* Cambridge Univ. Press, New York, 572 pp.

Hu, Y., M., M. Vaughan, Z. Liu, B. Lin, P. Yang, D. Flittner, B. Hunt, R. Kuehn, J. Huang, D. Wu, S. Rodier, K. Powell, C. Trepte, and D. Winker, 2007: The depolarization - attenuated backscatter relation: CALIPSO lidar measurements vs. theory. *Opt. Express*, **15**, 5327–5332.

INSITU, retrieved date 2014: ScanEagle Capabilities. [Available online at http://www.insitu.com/systems/scaneagle/capabilities]

Janjić, Z. I., 1994: The step-mountain eta coordinate model: Further developments of the convection, viscous sublayer, and turbulence closure schemes. *Mon. Wea. Rev.*, **122**, 927-945.

Jiang, X., C. Wiedinmyer, F. Chen, Z. Yang, J. C. Lo, 2008: Predicted impacts of climate and land use change on surface ozone in the Houston, Texas, area. *J. Geophys. Res.*, **113D20**, 312-328.

Johnson, E. A., and K. Miyanishi, 2001: *Forest fires behavior and ecological effects*. Academic Press, San Diego, CA, USA, 594 pp.

Jun, M., and R. D'Andrea, 2003: Path planning for unmanned aerial vehicles in uncertain and adversarial environments. *Cooperative control: Models, applications and algorithms*. University of Florida & Air Force Research Lab, Springer, New York City, NY, USA. 95-110.

Kanakidou, M., J. H. Seinfeld, S. N. Pandis, I. Barnes, F. J. Dentener, M. C. Facchini, R. Van Dingenen, B. Ervens, A. Nenes, C. J. Nielsen, E. Swietlicki, J. P. Putaud, Y. Balkanski, S. Fuzzi, J. Horth, G. K. Moortgat, R. Winterhalter, C. E. L. Myhre, K. Tsigaridis, E. Vignati, E. G. Stephanou, and J. Wilson, 2005: Organic aerosol and global climate modeling: a review. *Atmos. Chem. Phys.*, **5**, 1053-1123.

Kasischke, E. S., D. Verbyla, T. S. Rupp, A. D. McGuire, K. A. Murphy, R. Jandt, J. L. Barnes, E. E. Hoy, P. A. Duffy, M. Calef, and M. R. Turetsky, 2010: Alaska's changing fire regime — implications for the vulnerability of its boreal forests. *Can. J. For. Res.*, **40**, 1313–1324.

Kinney, P. L., 2008: Climate change, air quality, and human health. *Am. J. Prev. Med.*, **35**, 459–67.

Knuth, S. L. and J. J. Cassano, 2011: An analysis of near-surface winds, air temperature, and cyclone activity in Terra Nova Bay, Antarctica, from 1993 to 2009. *J. Appl. Meteorol. Climatol.*, **50**, 662–680.

Kosmatka, J. B., C. E. Foerster, M. Lega, G. Persechino, retrieved date 2010: Air quality plume detection and monitoring using UAVs and unmanned rotorcraft. *Proc. Nat. Air Quality Conf.: Air quality forecasting, mapping and monitoring communicating air quality*, Raleigh, NC. [Available online at http://www.epa.gov/airnow/2010conference/naqc/forecasting/kosmatka_final.pdf]

Langmann, B., B. Duncan, C. Textor, J. Trentmann, and G. R. van der Werf, 2009: Vegetation fire emissions and their impact on air pollution and climate. *Atmos. Environ.*, **43**, 107-116.

Leelasakultum K., N. Mölders, H. N. Q. Tran, and G. A. Grell, 2012: Potential impacts of the introduction of low-sulfur fuel on $PM_{2.5}$ concentrations at breathing level in subarctic city. *Adv. Meteorol.*, **2012**, 16 pp.

Levine, J. S., 1991: *Global biomass burning: Atmospheric, climatic, and biospheric implications*. MIT Press, Cambridge, Mass. 569 pp.

Levine, J. S. 1996: *Biomass burning and global change*. **Vol 2.**, MIT Press, Cambridge, Mass., 902 pp.

Lin, Y., R. D. Farley, and H. D. Orville, 1983: Bulk parameterization of the snow field in a cloud model. *J. Climatol. Appl. Meteorol.*, **22**, 1065- 1092.

Liu, Y., S. Goodrick, and W. Heilman, 2014: Wildland fire emissions, carbon, and climate: wildfire-climate interactions. *J. For. Ecol. & Manag.*, **317**, 80-96.

Logan, J. A., 1983: Nitrogen oxides in the troposphere: global and regional budgets. *J. Geophys. Res.*, **88**, 10785-10807.

Lotspeich, F. B., and E. W. Mueller, 1971: Effects of fire in the taiga on the environment. *Proc. Fire in the N. Env.*, Fairbanks, AK, Alaska Forest Fire and Council and Alaska Section, Society of American Foresters, 45- 50.

Lynch, J.A., J. S. Clark, N. H. Bigelow, M. E. Edwards, and B. P. Finney, 2003: Geographic and temporal variation in fire history in boreal ecosystems of Alaska. *J. Geophys. Res*. **108D**(1), 8152.

Madden, J. M., 2014: Using WRF/Chem, in-situ observations, and CALIPSO data to simulate smoke plume signatures on high-latitude pixels. M.S. Thesis. Department of Atmospheric Sciences, University of Alaska Fairbanks, Fairbanks, AK, USA. 106 pp.

Madronich, S., 1987: Photodissociation in the atmosphere, 1. Actinic flux and the effects of ground reflections and clouds. *J. Geophys. Res.*, **92**, 9740-9752.

Marris, E., 2013: Drones in science: Fly and bring me data. *Nature*, **498**, 156-158.

Martin, S., J. Bange, and F. Beyrich, 2011: Meteorological profiling of the lower troposphere using the research UAV "M²AV Carolo". *Atmos. Meas. Tech.*, **4**, 705-716.

McClelland, J. W., R. M. Holmes, B. J. Peterson, and M. Stieglitz, 2004: Increasing river discharge in the Eurasian Arctic: Consideration of dams, permafrost thaw, and fires as potential agents of change. *J. Geophys. Res.*, **109**, D18102.

McCormick, M. P., 2005: Airborne and spaceborne lidar. In: *Lidar, range-resolved optical remote sensing of the atmosphere*, C. Weitcamp, Ed, Springer Science+Media Inc. New York City, NY, USA. 355–397.

McCreary, A., retrieved date 2014: Fighting wildfires from aloft. [Available online at http://methowvalleynews.com/2014/07/31/fighting-wildfires-from-aloft/]

McGuiney, E., M. Shulski, and G. Wendler, 2005: Alaska lightning climatology and application to wildfire science. Extended Abstract, *Conf. on Meteorological applications of lightning*, San Diego, CA, Amer. Meteor. Soc., P2.14

Mellor, G. L., and T. Yamada, 1982: Development of a turbulence closure model for geophysical fluid problems. *Rev. Geophys. Space Phys.*, **20**, 851-875.

Middleton, P., W. R. Stockwell, and W. P. R. Carter, 1990: Aggregation and analysis of volatile organic compound emissions for regional modeling. *Atmos. Environ.*, **24**, 1107-1133.

Mishchenko, M. I., and K. Sassen, 1998: Depolarization of lidar returns by small ice crystals: An application to contrails. *Geophys. Res. Lett.*, **25**, 309–312.

Mlawer, E. J., S. J. Taubman, P. D. Brown, M. J. Iacono, and S. A. Clough, 1997: Radiative transfer for inhomogeneous atmospheres: RRTM, a validated correlated-k model for the longwave. *J. Geophys. Res.*, **102**, 16663-16682.

Mölders, N., A. Raabe, and G. Tetlaff, 1996: A comparison of two strategies on land surface heterogeneity used in a mesoscale β meteorological model. *Tellus*, **48A**, 733-749.

Mölders, N., and G. Kramm, 2007: Influence of wildfire induced land-cover changes on clouds and precipitation in Interior Alaska — A case study. *Atmos. Res.*, **84**, 142–168.

Mölders, N., 2008: Suitability of the Weather Research and Forecasting (WRF) model to predict the June 2005 fire weather for Interior Alaska. *Wea. Forecasting*, **23**, 953–973.

Mölders, N., S. E. Porter, C. F. Cahill, and G. A. Grell, 2010: Influence of ship emissions on air quality and input of contaminants in southern Alaska National Parks and wilderness Areas during the 2006 tourist season. *Atmos. Environ.*, **44**, 1400-1413.

Mölders, N., H. N. Q. Tran, P. Quinn, K. Sassen, G. E. Shaw, and G. Kramm, 2011: Assessment of WRF/Chem to simulate sub-Arctic boundary layer characteristics during low solar irradiation using radiosonde, SODAR, and surface data. *Atmos. Pollut. Res.*, **2(3)**, 283-299.

Mölders, N., 2011: *Land-use and land-cover changes, impact on climate and air quality*. Springer, New York City, NY, USA. 190 pp.

Mölders, N., T., Huy, C. F. Cahill, L. Ketsiri, T. Tran, 2012: Assessment of WRF/Chem PM2.5 forecasts using mobile and fixed location data from the Fairbanks, Alaska winter 2008/09 field campaign. *Atmos. Pollut. Res.*,**3**,180-191.

Mölders, N., S. Gende, and M. Pirhalla, 2013: Assessment of Cruise-Ship Activity Influences on Emissions, Air Quality, and Visibility in Glacier Bay National Park" *Atmos. Pollut. Res.*, **4**, 435-445.

Mölders, N., 2014, Personal Communication, WRF/Chem simulations.

Monin, A. S., and A. M Obukhov, 1954: Basic laws of turbulent mixing in the surface layer of the atmosphere. *Tr. Akad. Nauk SSSR Geophiz. Inst*, **24**, 163-187.

Mott, J. A., P. Meyer, D. Mannino, S. C. Redd, E. M. Smith, C. Gotway-Crawford, and E. Chase, 2002: Wildland forest fire smoke: Health effects and intervention evaluation, Hoopa, California, 1999. *West. J. Med.*, **176**, 157–162.

Müller, D., I. Mattis, U. Wandinger, A. Ansmann, D. Althausen, and A. Stohl, 2005: Raman lidar observations of aged Siberian and Canadian forest fire smoke in the free troposphere over Germany in 2003: Microphysical particle characterization. *J. Geophys. Res.*, **110**, D17201.

Murayama, T., D. Müller, K. Wada, A. Shimizu, M. Sekiguchi, and T. Tsukamoto, 2004: Characterization of Asian dust and Siberian smoke with multi-wavelength Raman lidar over Tokyo, Japan in spring 2003. *Geophys. Res. Lett.*, **31**, L23103.

Nance, J. D., P. V. Hobbs, L. F. Radke, and D. E. Ward, 1993: Airborne measurements of gases and particles from an Alaskan wildfire. *J. Geophys. Res.*, **98**, 14873-14882.

NASA EOSDIS, retrieved date 2015: Near real-time data. [Available online at http://lance-modis.eosdis.nasa.gov/imagery/subsets/?area=global]

NCEP (National Centers for Environmental Prediction) retrieved date 2000 [Available online at http://www.ncep.noaa.gov]

NOVA/PBS, retrieved date 2002: Timeline of UAVs. [Available online at http://www.pbs.org/wgbh/nova/spiesfly/uavs.html]

NPS (National Park Service), retrieved date 2014: Alaska wildfire management program. [Available online at http://www.nps.gov/fire/wildland-fire/connect/regional-programs/alaska.cfm]

NRC (National Research Council): Committee on air quality management in the United States, board on environmental studies and toxicology, board on atmospheric sciences and climate, Division on Earth and Life Studies, 2004, air quality management in the United States. National Academies Press, Washington, D.C., USA. [ISBN 0-309-08932-8], 426 pp.

NWCG (National Wildfire Coordination Group), retrieved date 2009: Crazy Mountain Complex, incident status overview. [Available online at https://fam.nwcg.gov/fam-web/hist_209/hist_r_print_209_head_2009?v_number=AK-UYD-000897&v_report_date=08/01/2009&v_hour=2200&v_gaid=AK]

NWS (National Weather Service) retrieved date 2014, Archived Maps 2009. [Available online at http://pafc.arh.noaa.gov/data/archive/sfcmap/2009/]

Olsen, D. L., J. B. Cronan, D. McKenzie, J. L. Barnes, A. E. Camp, M. Tjoelker, J. Northway, and P. Eagle, 2011: Compiling, synthesizing and analyzing existing boreal forest fire history data in Alaska – final report to the joint fire science program. PROJECT #06-3-1-26, 27 pp.

PaiMazumder, D. and N. Mölders, 2009: Theoretical assessment of uncertainty in regional averages due to network density and design. *J. Appl. Meteorol. Climatol.*, **48**, 1643–1666.

Patterson M. C. L., A. Mulligan, J. Douglas, J. Robinson, L. Wardell, and J. S. Pallister, 2005: Volcano surveillance by ACR Silver Fox. *Amer. Inst. of Aero. and Astro*, **1**, 26-29.

Peckham, S. E.. G. A. Grell, S. A. McKeen, M. Barth, G. Pfister, C. Wiedinmyer, J. D. Fast, W. I. Gustafson, S. J. Ghan, R. Zaveri, R. C. Easter, J. Barnard, E. Chapman, M. Hewson, R. Schmitz, M. Salzmann, and S. R. Freitas, 2011: WRF/Chem Version 3.3 User's Guide. 96 pp.

Phan, C., and H. H. T. Liu, 2008: A cooperative UAV/UGV platform for wildfire detection and fighting. *Proc. Asia Simulation Conf*, Kuala Lumpur, Malaysia, IEEE Computer Society, 494-498.

Piccot, S. D., J. J. Watson, and J. W. Jones, 1992: A global inventory of volatile organic compound emissions from anthropogenic sources. *J. Geophys. Res.*, **97**, 9897–9912.

Plumb, E., NWS, 2015: Personal Correspondence.

Porter, S. E., 2009: Investigation of the impact of ship emissions on atmospheric composition and deposition into remote, coastal landscapes of southwest Alaska. M.S. Thesis, Department of Atmospheric Sciences, University of Alaska Fairbanks, Fairbanks, AK, USA. 122 pp.

Prather, M. J., 1996: Time scales in atmospheric chemistry: Theory, GWPs for CH_4 and CO, and runaway growth. *Geophys. Res. Lett.*, **23**, 2597-2600.

Runge H., W. Rack, A. Ruiz-Leon, and M. Hepperle, 2007: A solar powered HALE-UAV for arctic research. *1st CEAS European Air and Space Conference*, Berlin Germany. 1-6 pp.

Sassen, K., 2002: Indirect climate forcing over the western US from Asian dust storms. *Geophys. Res. Lett.*, **29**, 103–1–103–4.

Sassen, K., and V. I. Khvorostyanov, 2008: Cloud effects from boreal forest fire smoke: Evidence for ice nucleation from polarization lidar data and cloud model simulations. *Environ. Res. Lett.*, **3**, doi:10.1088/1748–9326/3/2/025006.

Sauter, B. and T. Henmi, 2004: *Average forecast errors using MM5 and WRF over complex terrain: Utah, July/August 2003 and January/February 2004.* No. ARL-MR-597. Army Research Lab White Sands Missile Range, NM. 24 pp.

Schell, B., I. J. Ackermann, H. Hass, F. S. Binkowski, and A. Ebel, 2001: Modeling the formation of secondary organic aerosol within a comprehensive air quality model system. *J. Geophys. Res.*, **106**, 28275-28293.

Seinfeld, J. H., and S. N. Pandis, 2006: *Atmospheric chemistry and physics: From air pollution to climate change.* Wiley, Hoboken, NJ, USA. 1232pp.

Shulski, M., and G. Wendler, 2007: *The Climate of Alaska.* University of Alaska Press, Fairbanks, AK, USA. 216 pp.

Simpson, D., A. Guenther, C. N. Hewitt, and R. Steinbrecher, 1995: Biogenic emissions in Europe. 1. Estimates and uncertainties. *J. Geophys. Res.*, **100D**, 22875–22890.

Skamarock, C. W., J. B. Klemp, J. Dudhia, D. O. Gill, D. M. Barker, M. G. Duda, X. Huang, W. Wang, and J. G. Powers, 2008: *A description of the advanced research WRF Version 3.* NCAR Tech. Note NCAR/TN–475+STR, 125 pp.

Smirnova, T. G., J. M. Brown, and S. G. Benjamin, 1997: Performance of different soil model configurations in simulating ground surface temperature and surface fluxes. *Mon. Wea. Rev.*, **125**, 1870-1884.

Smirnova, T. G., J. M. Brown, S. G. Benjamin, and D. Kim, 2000:, Parameterization of cold-season processes in the MAPS land-surface scheme. *J. Geophys. Res.*, **105**, 4077–4086.

Solazzo, E., R. Bianconi, G. Pirovano, V. Matthias, R. Vautard, M. D. Moran, K. W. Appel, B. Bessagnet, J. Brandt, J. H. Christensen, C. Chemel, I. Coll, J. Ferreira, R. Forkel, X. V. Francis, G. Grell, P. Grossi, A. B.

Hansen, A. I. Miranda, U. Nopmongcol, M. Prank, K. N. Sartelet, M. Schaap, J. D. Silver, R. S. Sokhi, J. Viras, J. Werhahn, R. Wolke, G. Yarwood, J. Zhang, S. T. Rao, and S. Galmarini, 2012: Operational model evaluation for particulate matter in Europe and North America in the context of AQMEII. *Atmos. Environ.*, **53**, 75-92.

Stockwell, W. R., P. Middleton, J. S. Chang, and X. Tang, 1990: The second generation regional acid deposition model chemical mechanism for regional air quality modeling. *J. Geophys. Res.*, **95**, 16343-16367.

Tran, H. Q. N., and N. Mölders, 2012: WRF/Chem simulations for the Crazy Mountain Fires.

Tran, H. Q. N., and N. Mölders, 2014: WRF/Chem simulations setup.

UCAR, 2012: Wildfires, weather and climate. [Available online at https://www2.ucar.edu/news/backgrounders/wildfires-weather-climate]

U. S. Census Bureau, retrieved date 2014: State and county quick facts: Alaska. [Available online at http://quickfacts.census.gov/qfd/states/02000.html]

U.S.G.S. (U.S. Geological Survey) retrieved date 2014: Ecosystems and climate history of Alaska. [Available online at http://gec.cr.usgs.gov/archive/alaska/alaskaB.html]

van der Werf G. R., J. T. Randerson, L. Giglio, G. J. Collatz, M. Mu, P. S. Kasibhatla, D. C. Morton, R. S. DeFries, Y. van Jin, and T. T. van Leeuwen, 2010: Global fire emissions and the contribution of deforestation, savanna, forest, agricultural, and peat fires (1997-2009). *Atm. Chem. Phys.*, **10**, 11707-11735.

Val Martín, M. V., R. E. Honrath, R. C. Owen, G. Pfister, P. Fialho, and F. Barata, 2006: Significant enhancements of nitrogen oxides, black carbon, and ozone in the North Atlantic lower free troposphere resulting from North American boreal wildfires. *J. Geophys. Res.*, **111 D23S60**.

Vicente, A., C. Alves, A. I. Calvo, A. P. Fernandes, T. Nunes, C. Monteiro, S. M. Almeida, and C. Pio, 2013: Emission factors and detailed chemical composition of smoke particles from the 2010 wildfire season. *Atmos. Environ.*, **71**, 295–303.

146

Vidale, P. L., R. A. Pielke, L. T. Steyaert, and A. Barr, 1997: Case study modeling of turbulent and mesoscale fluxes over the BOREAS region. *J. Geophys. Res.*, **102(D24)**, 29167–29188.

von Storch and F. W. Zwiers, 2001: *Statistical analysis in climate research.* Cambridge University Press. New York, NY, USA. 484 pp.

VORTEX2, retrieved date 2015: VORTEX2 2009-2010. [Available online at http://www.vortex2.org/home/]

Wandinger, U., D. Müller, C. Böckmann, D. Althausen, V. Matthias, J. Bösenberg, V. Wieß, M. Fiebig, M. Wendisch, A. Stohl, and A. Ansmann, 2002: Optical and microphysical characterization of biomass- burning and industrial-pollution aerosols from multiwavelength lidar and aircraft measurements. *J. Geophys. Res.*, **107**, 8125-8145.

Wandinger, U., 2005: Introduction to lidar. In: *Lidar, range-resolved optical remote sensing of the atmosphere*, C. Weitcamp, Ed., Springer Science+Business Media Inc., New York City, NY, USA. 1-18.

Ward, D. E., and C. C. Hardy, 1991: Smoke emissions from wildland fires. *Env. Int.*, **17**, 117-134.

Weaver, L. K., 2009: Carbon monoxide poisoning. *N. Engl. J. Med.*, **360**, 1217–1225.

Wendler, G., J. Conner, B. Moore, M. Shulski, and M. Stuefer, 2010: Climatology of Alaskan wildfires with special emphasis on the extreme year of 2004. *Theor. Appl. Climatol.*, **104**, 459-462.

Wesely M. L., 1989: Parameterization of surface resistance to gaseous dry deposition in regional numerical models. *Atmos. Environ.*, **16**, 1293-1304.

Western Regional Climate Center, retrieved date 2014: RAWS USA climate archives. [Available online at http://www.raws.dri.edu/index.html]

Yokelson, R. J., R. Susott, D. E. Ward, J. Reardon, and D. W. T. Griffith, 1997: Emissions from smoldering combustion of biomass measured by open-path Fourier transform infrared spectroscopy. *J. Geophys. Res.*, **102**, 18865-18877.

Zhang, Y., V. Dulière, P. W. Mote, and E. P. Salathé Jr, 2009: Evaluation of WRF and HadRM mesoscale climate simulations over the US Pacific Northwest. *J. Climate,* **22(20)**, 5511-5526.

Zhuang, Q., A. D. McGuire, K. P. O'Neill, J. W. Harden, V. E. Romanovsky, and J. Yarie, 2002: Modeling soil thermal and carbon dynamics of a fire chronosequence in Interior Alaska. *J. Geophys. Res.*, **108**, 8147.

Appendix

## 20 Hour Average of Meteorological and Chemical Quantities Pre and Post Cold Front

5 August is shown here because it is under quiescent synoptic conditions.

Sampling results on these days were similar to the results that were discussed in Chapter 4. Meaning differences and errors were similar no matter what day was being examined.
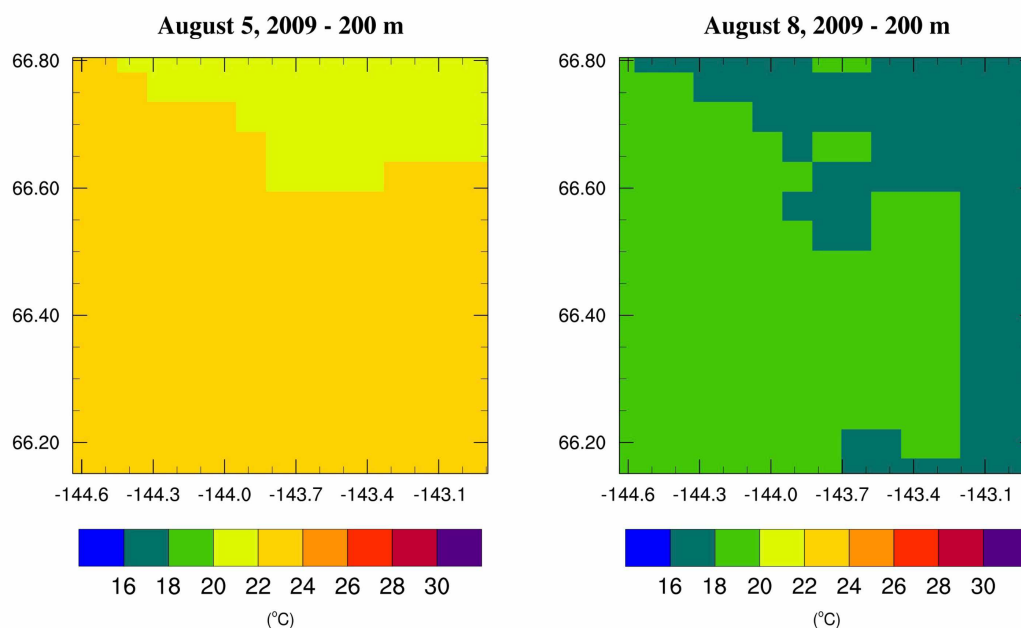
Figure A-1 The 20 hour 'grand truth' average temperatures on 5 August and 8 at the 200 m height. Valid for the 200 m height, all sampling directions, and all sampling speeds.
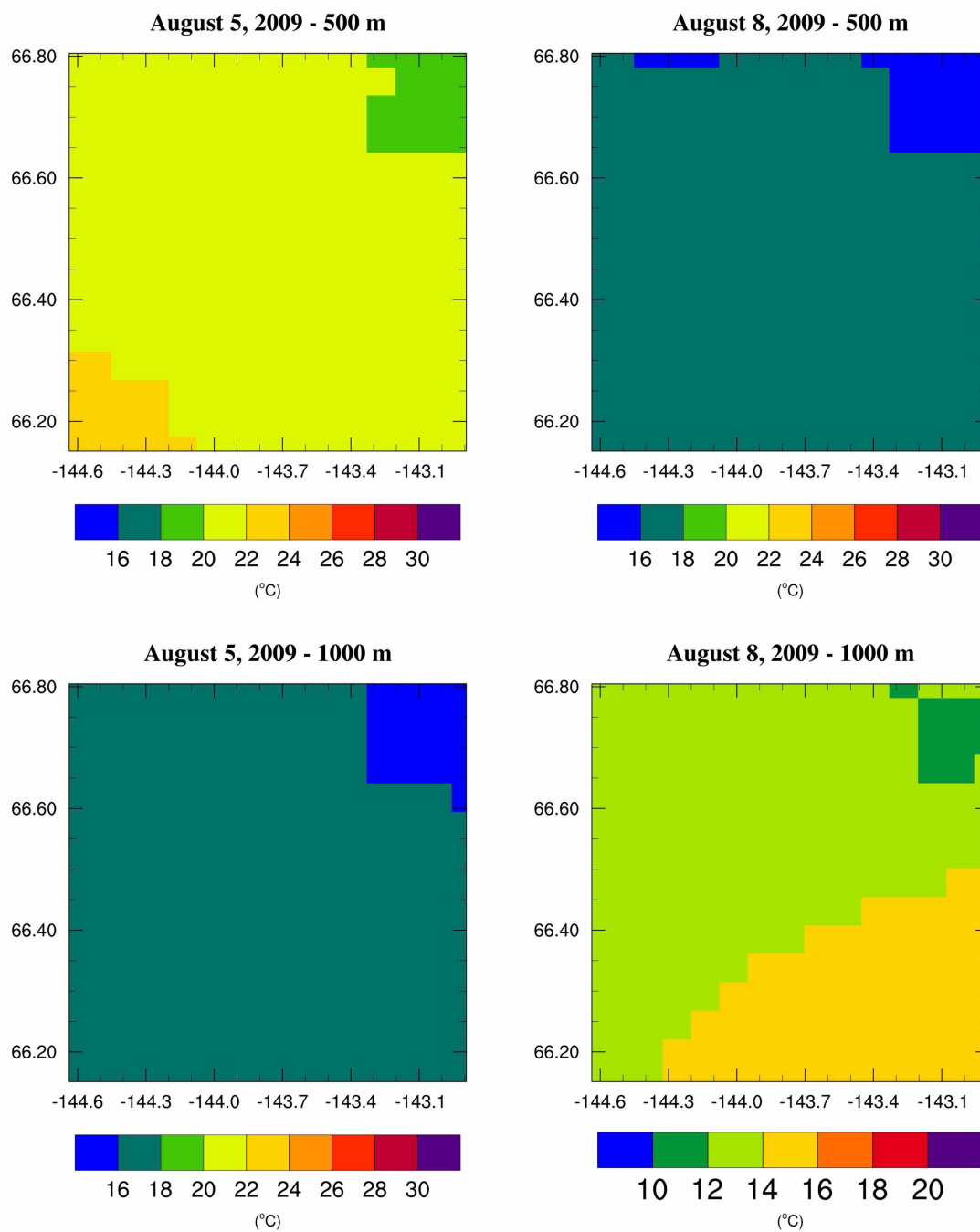
Figure A-2 The 20 hour 'grand truth' average temperatures on 5 August and 8 at the 500 and 1000 m heights. Note the different scale for 8 August at the 1000 m height. Vaild for the respective heights, all sampling directions, and all sampling speeds.

150
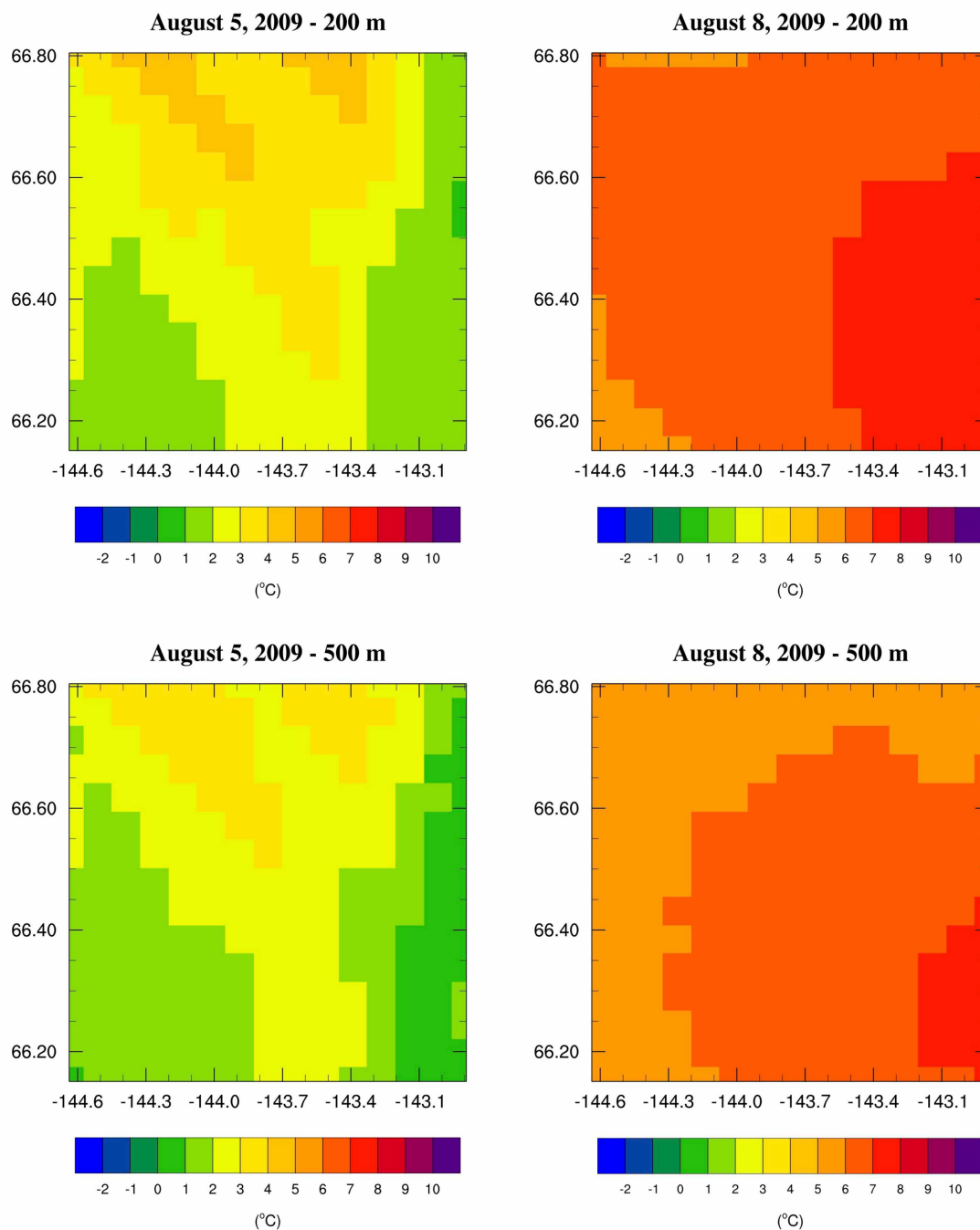
Figure A-3 The 20 hour 'grand truth' average dewpoint temperatures on 5 and 8 August at the 200 and 500 m heights. Valid for the respective heights, all sampling directions, and all sampling speeds.

August 5, 2009 - 1000 m

August 8, 2009 - 1000 m
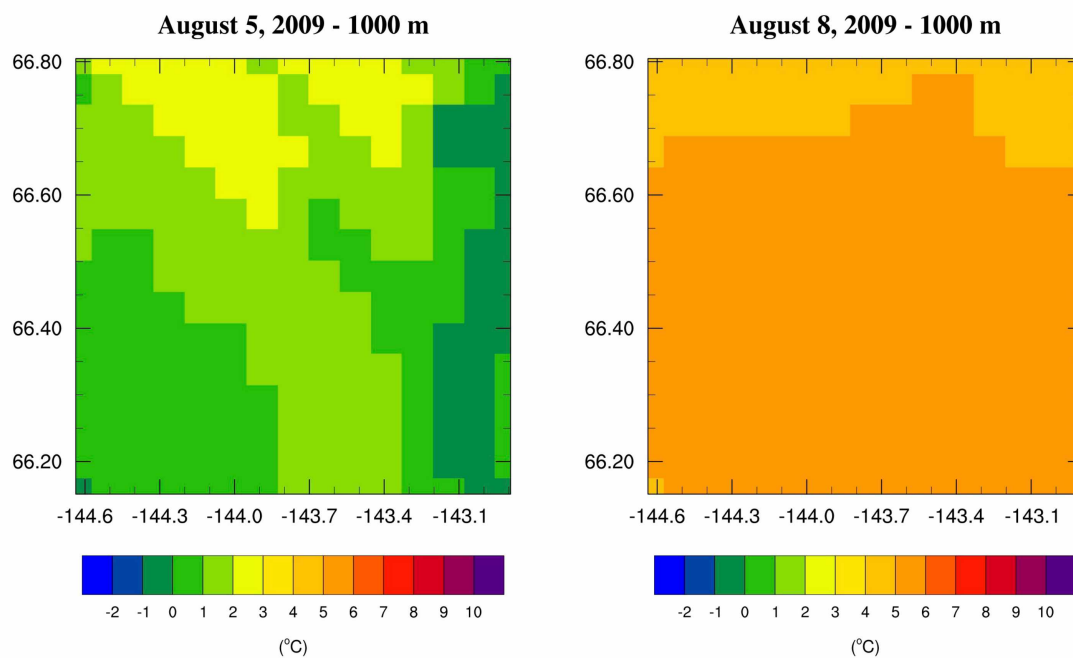
Figure A-4 The 20 hour 'grand truth' average dewpoint temperatures on 5 and 8 August at the 1000 m height. Vaild for the 1000 m height, all sampling directions, and all sampling speeds.
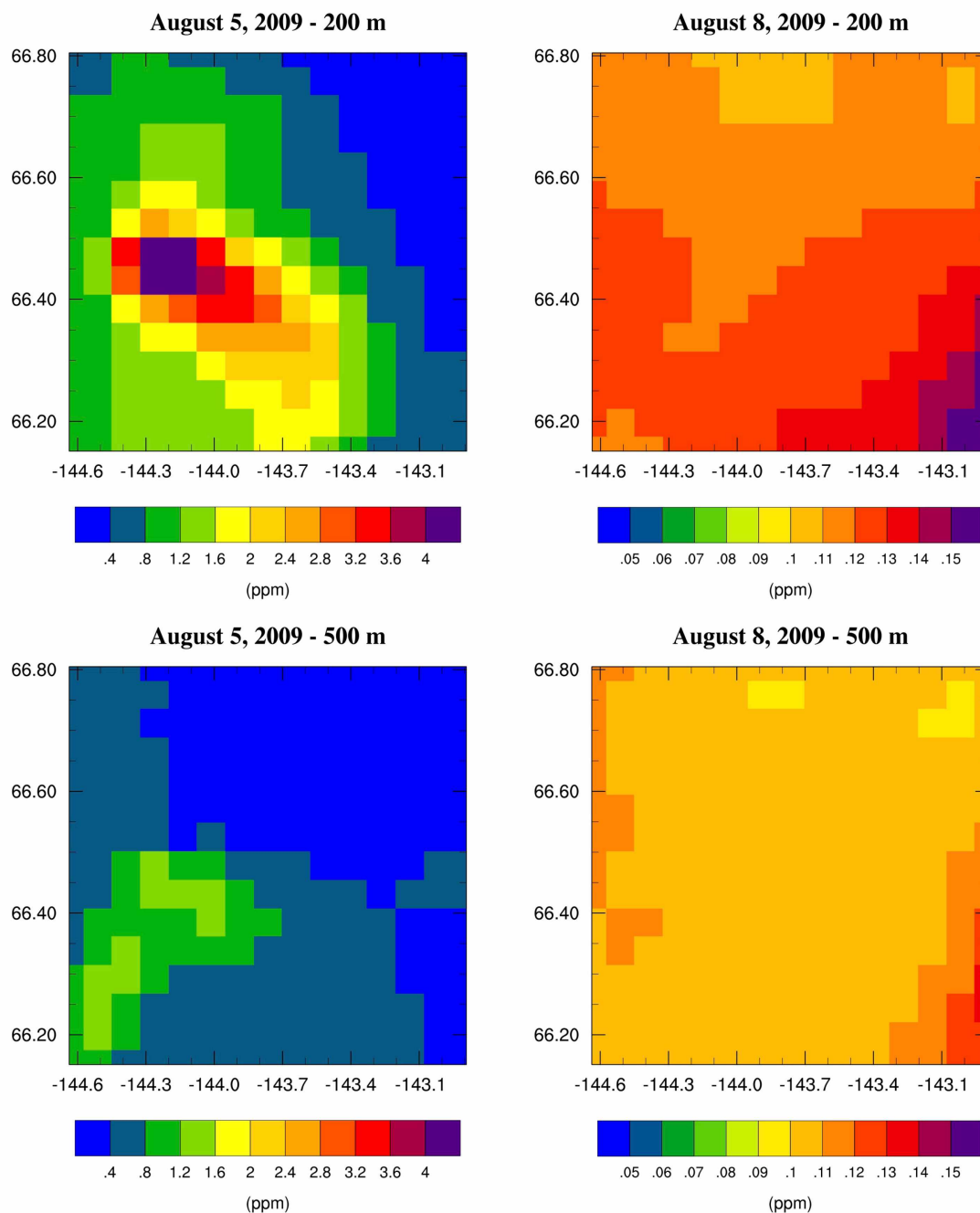
Figure A-5 The 20 hour 'grand truth' average CO concentrations on 5 and 8 August at the 200 and 500 m heights. Note the different scales for each day. Valid for the respective heights, all sampling directions, and all sampling speeds.

153
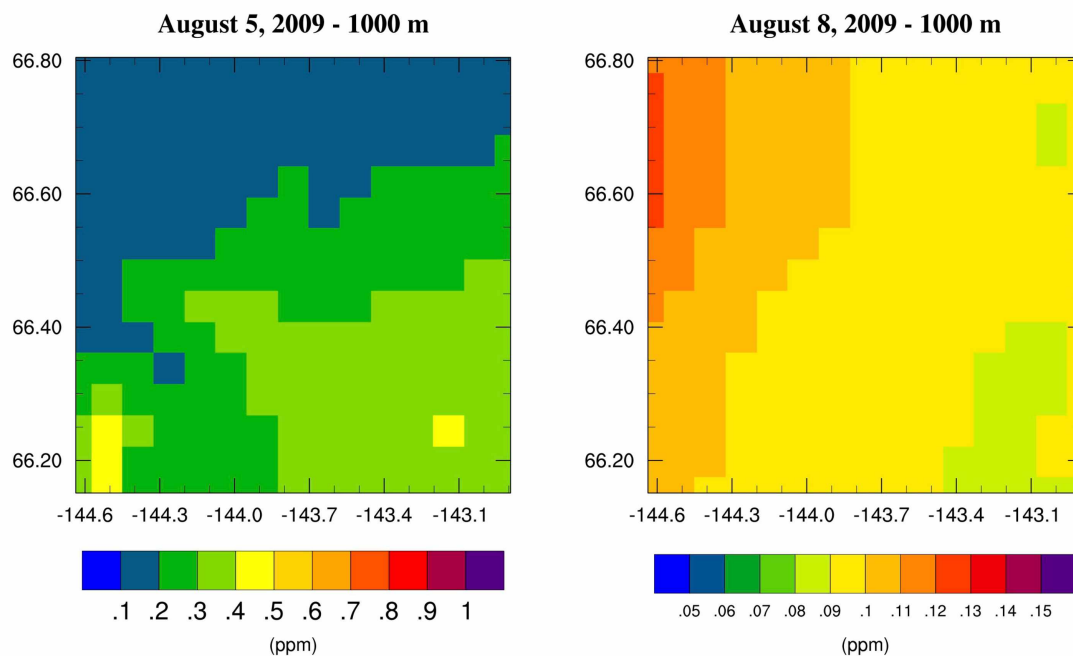
**Figure A-6** The 20 hour 'grand truth' average CO concentrations on 5 and 8 August at the 1000 m height. Note the different scales for each day. Valid for the 1000 m height, all sampling directions and sampling speeds.
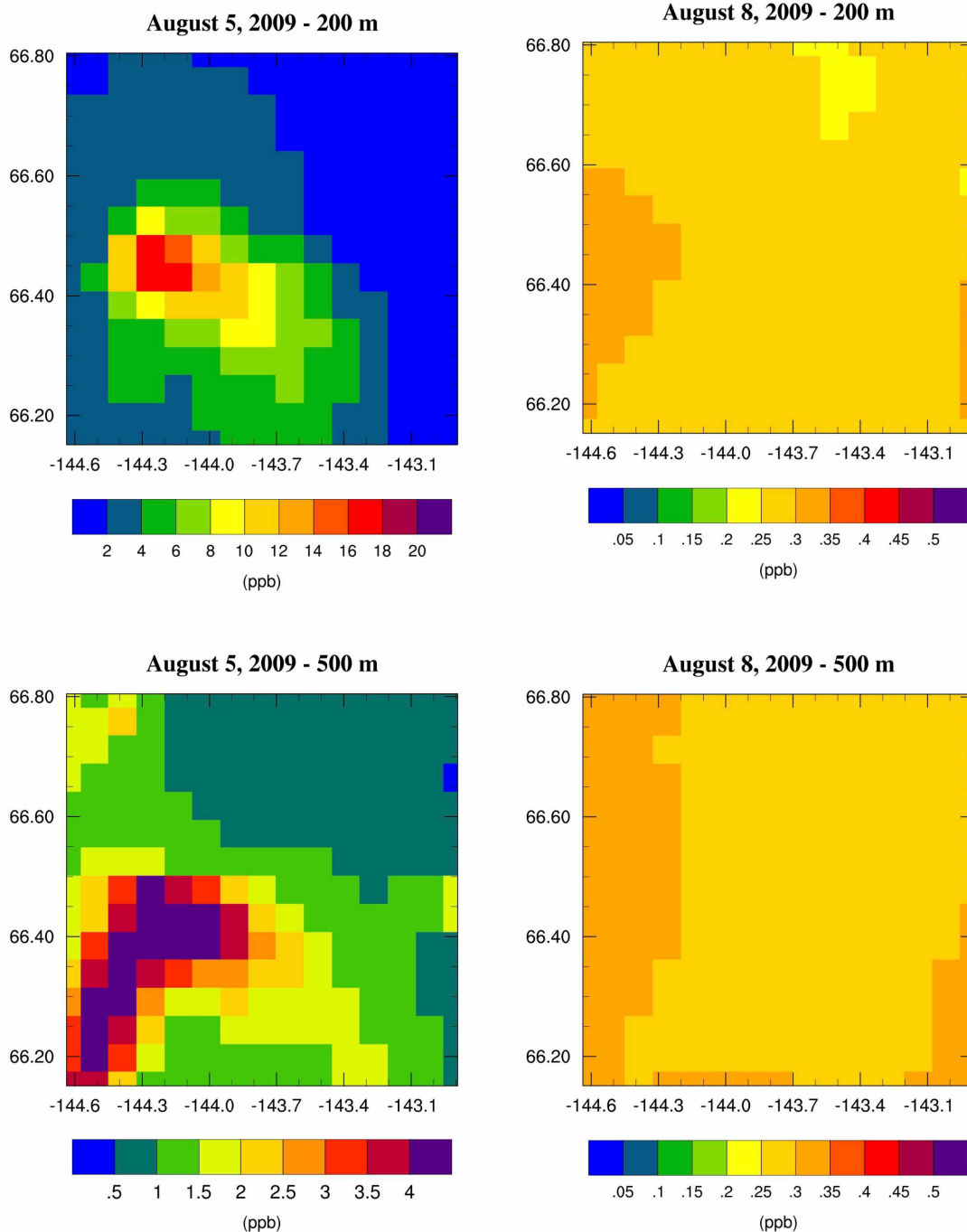
Figure A-7 The 20 hour 'grand truth' average SO$_2$ concentrations on 5 and 8 August at the 200 and 500 m heights. Note the different scales for 5 August. Valid for the respective heights, all sampling patterns, and all sampling speeds.

155
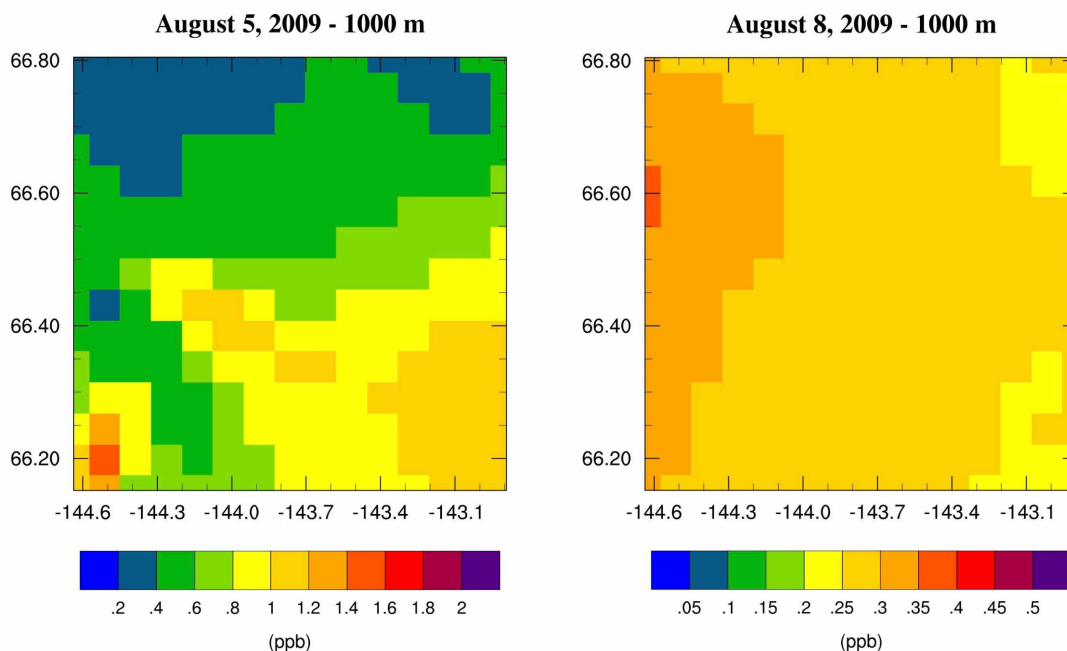
Figure A-8 The 20 hour 'grand truth' average SO₂ concentrations on 5 and 8 August at the 1000 m height. Note the different scales.
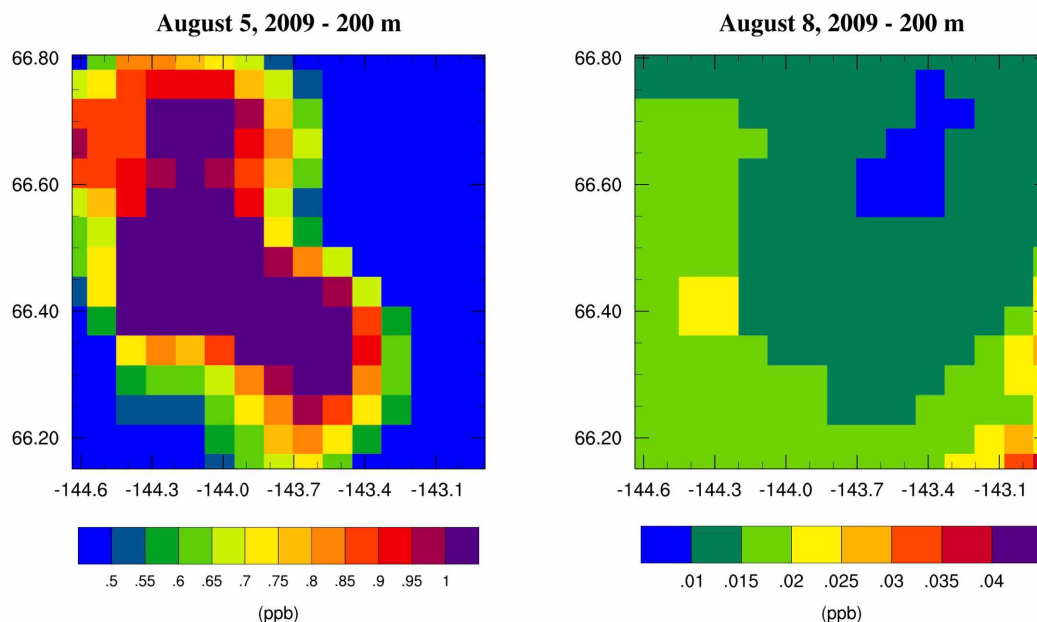
Figure A-9 The 20 hour 'grand truth' average NO concentrations on 5 and 8 August at the 200 m height. Note the different scales. Valid for the respective heights, all sampling directions, and all sampling speeds.
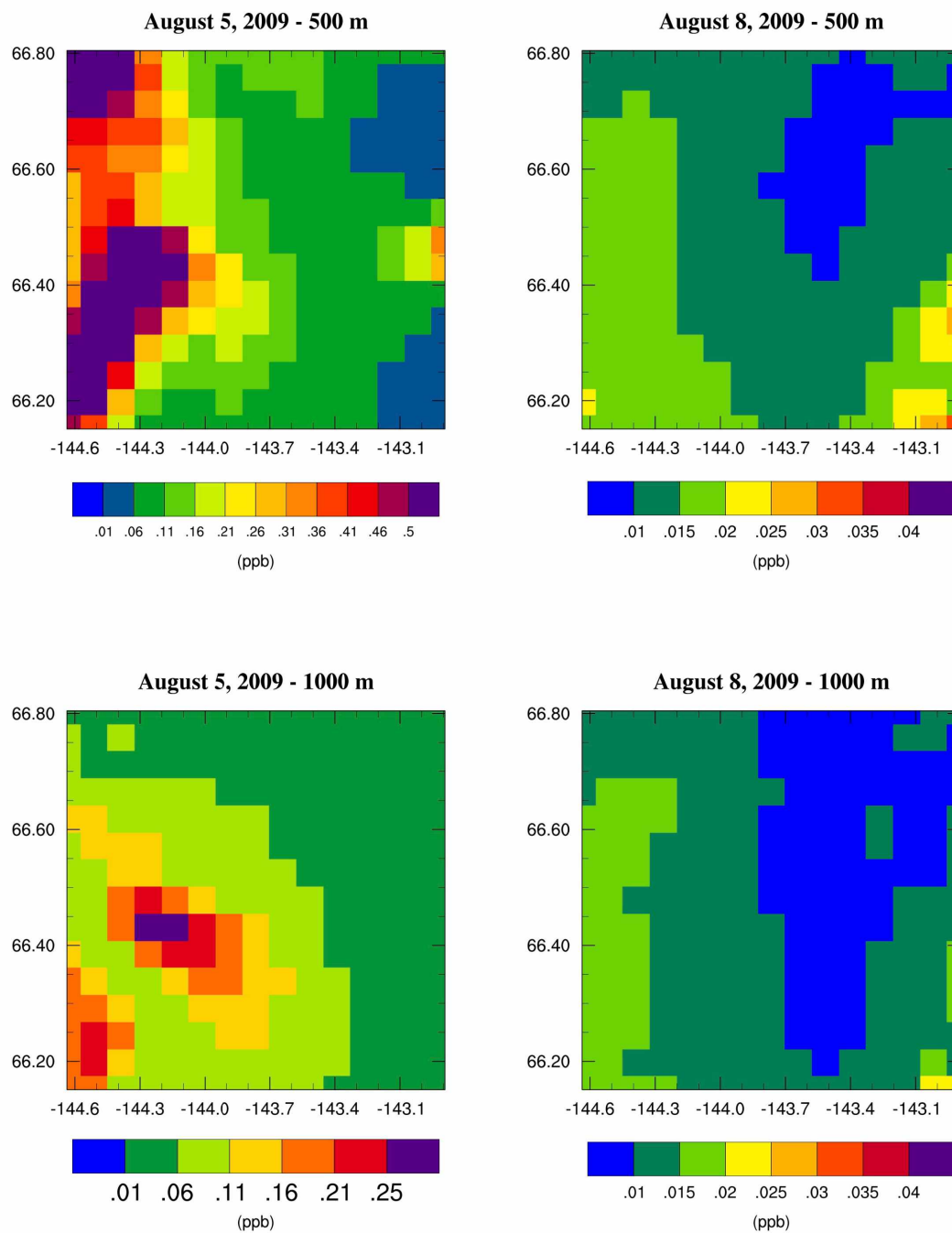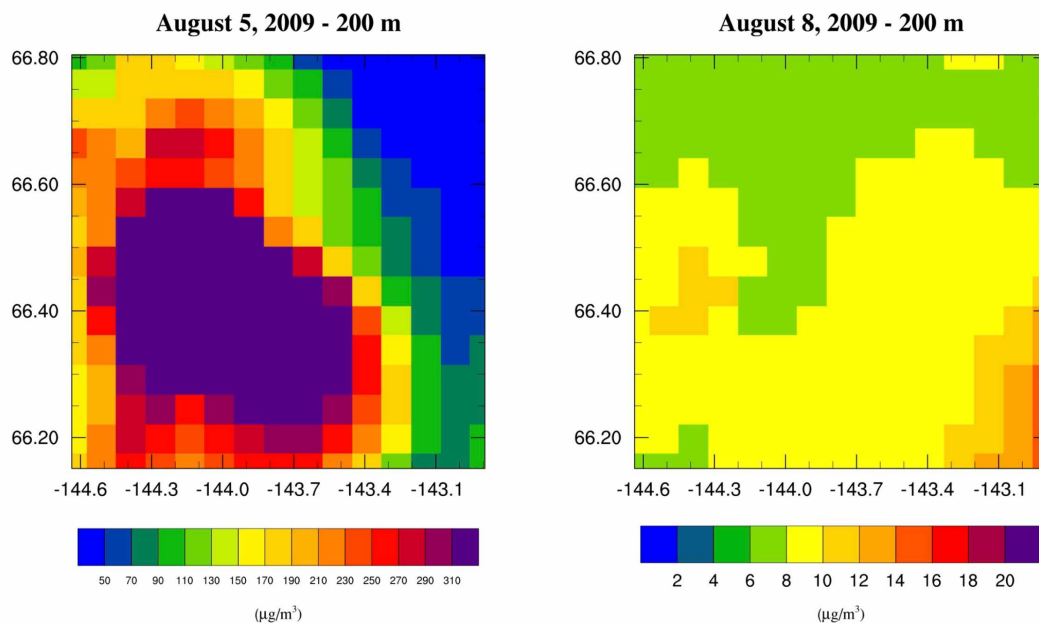
Figure A-10 20 hour average NO concentrations for 5 and 8 August at the 500 and 1000 m heights. Note the differing scales. Valid for the respective heights, all sampling directions, and all sampling speeds.
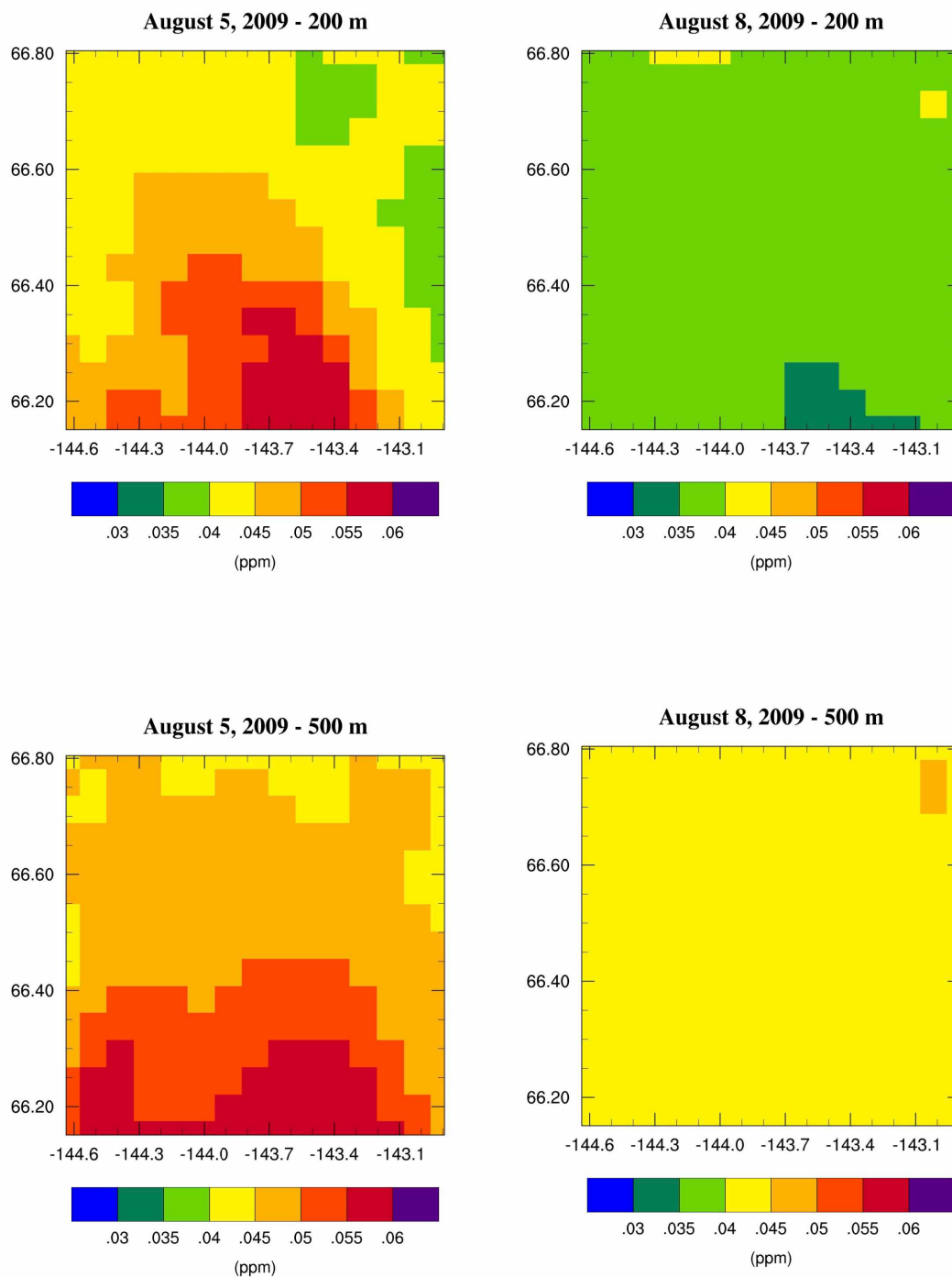
Figure A-11 20 hour average O₃ concentrations for 5 and 8 August at the 200 and 500 m heights. Valid for the respective sampling heights, all sampling directions, and all sampling speeds.
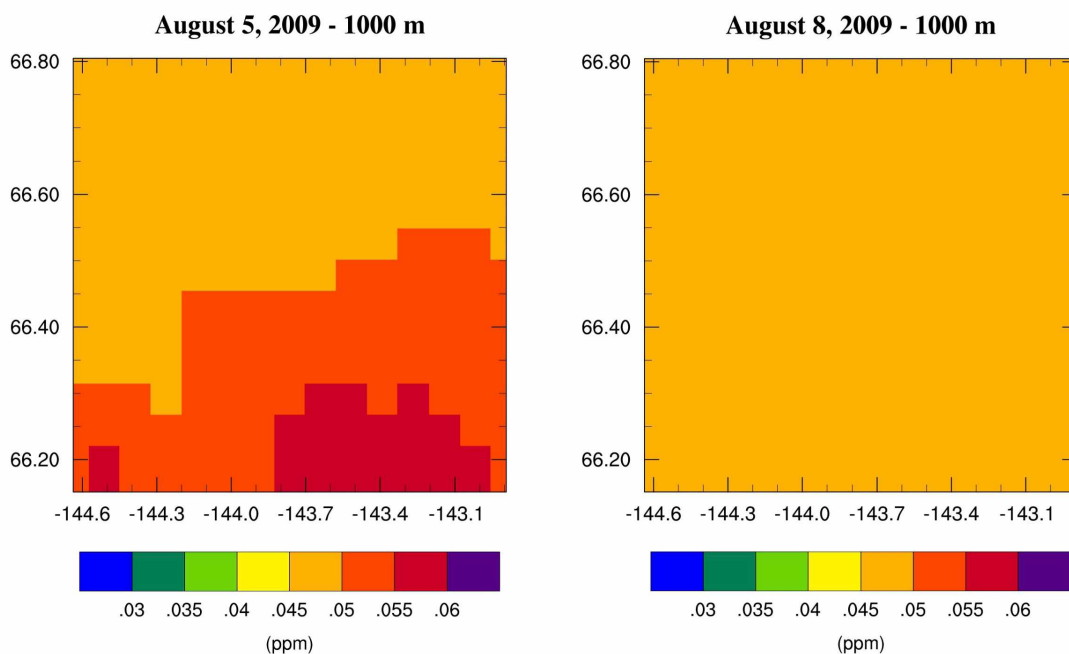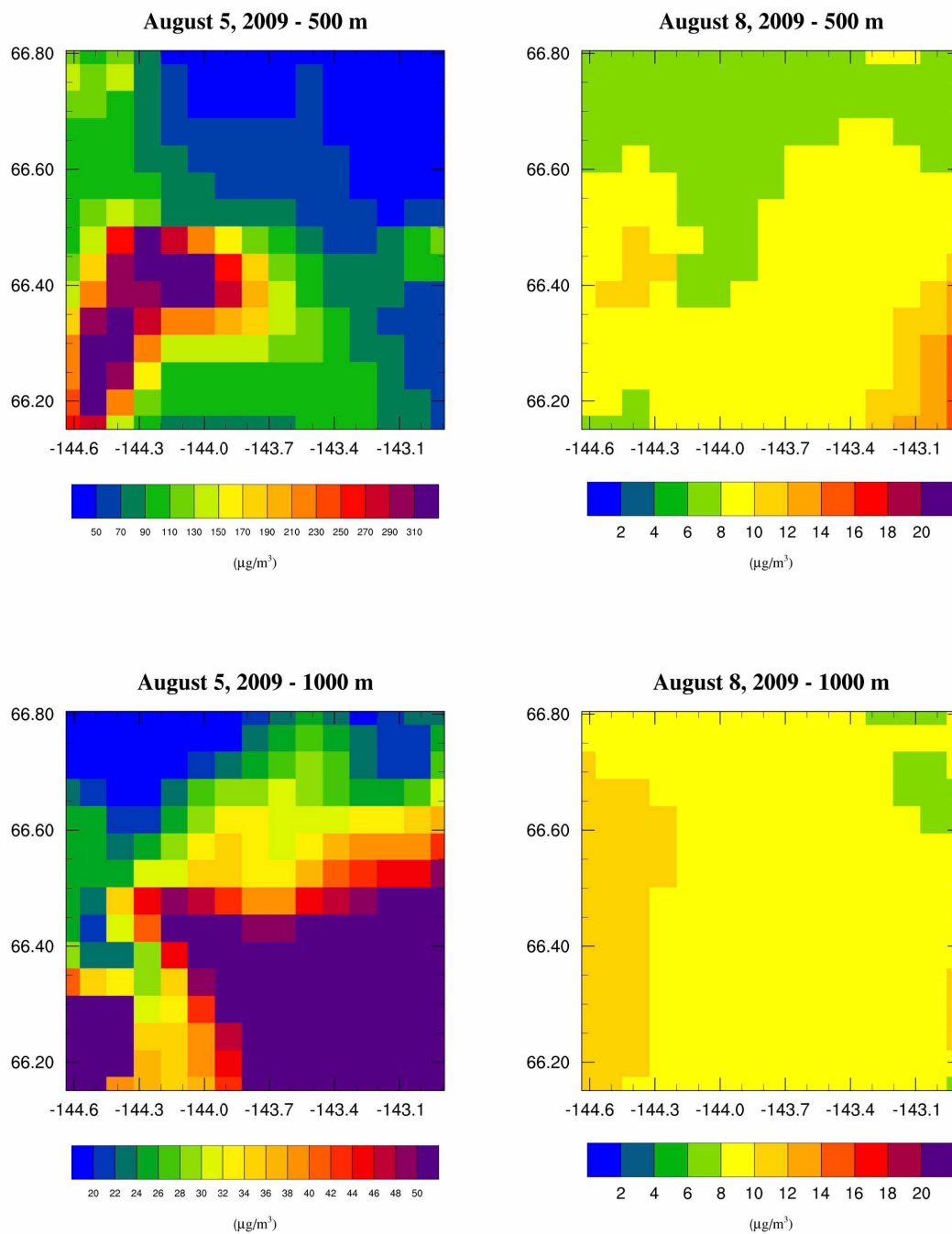
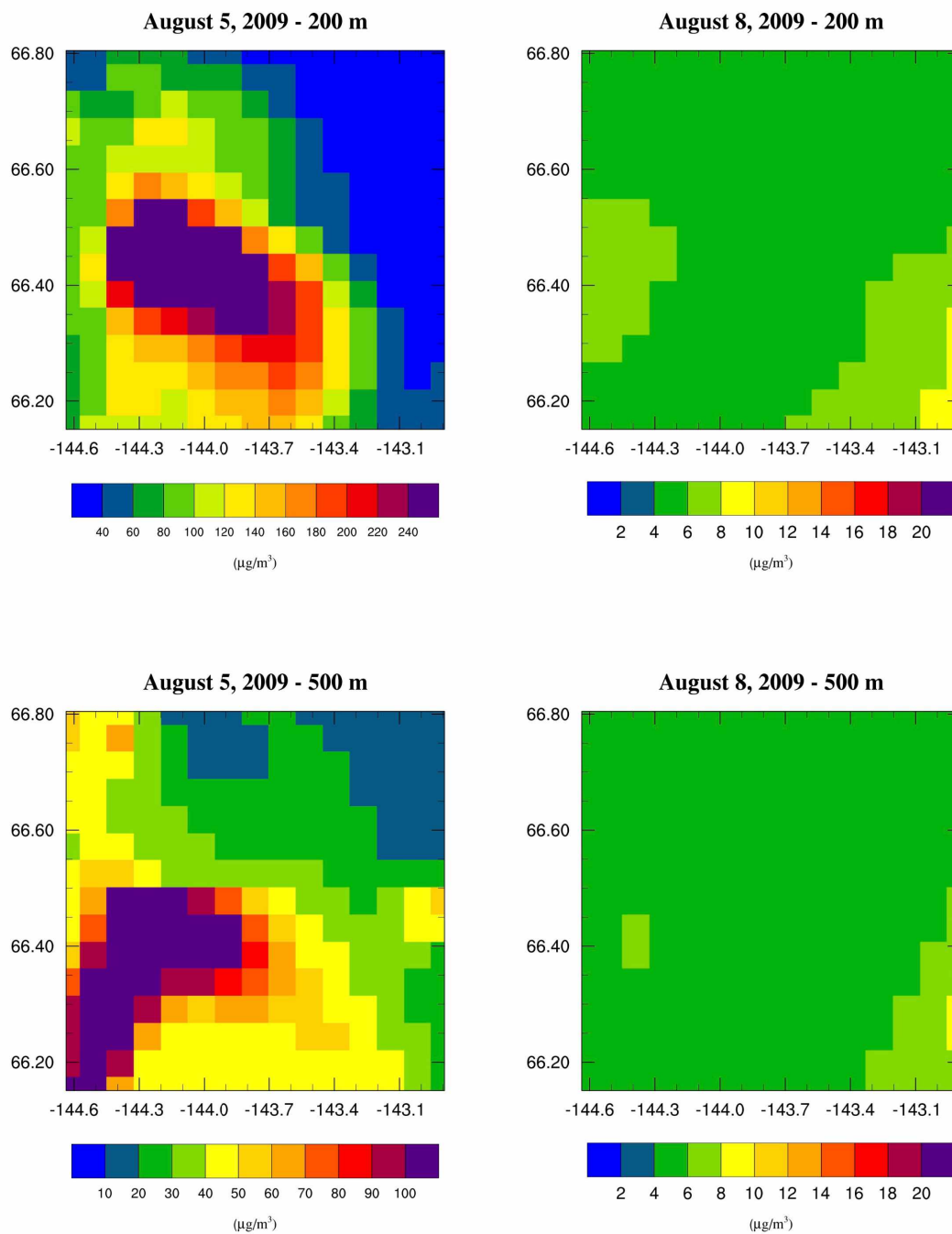**Figure A-12** 20 hour average O_3 concentrations for 5 and 8 August at the 1000 height.

Figure A-13 20 hour average PM_{10} concentrations for 5 and 8 August at the 200 height. Note the different scales. Valid for the respective heights, all sampling directions, and all sampling speeds.
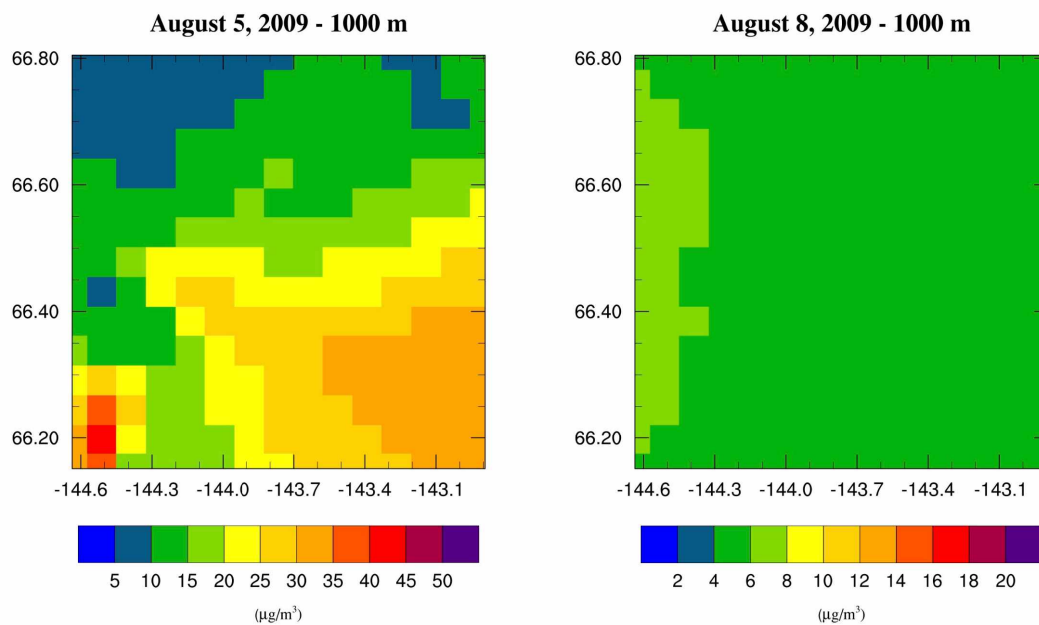
159

Figure A-14 20 hour average PM_{10} concentrations for 5 and 8 August at the 500 and 1000 m heights. Note the different scales. Valid for the respective sampling heights, all sampling directions, and all sampling speeds.

160

Figure A-15 20 hour average PM$_{2.5}$ concentrations for 5 and 8 August at the 200 and 500 m heights. Note the different scales. Valid for the respective heights, all sampling directions, and all sampling speeds.

Figure A-16 20 hour average PM$_{2.5}$ concentrations for 5 and 8 August at the 1000 height. Note the different scales. Valid for the 1000 m height, all sampling directions, and all sampling speeds.